



PONTIFICIA UNIVERSIDAD CATOLICA DE CHILE
SCHOOL OF ENGINEERING

PLASTIC ANISOTROPY AND FORMABILITY ESTIMATION IN ZINC SHEETS

FRANCISCO JAVIER ALISTER HERDENER

Thesis submitted to the Office of Graduate Studies in partial fulfillment of the requirements for the Degree of Doctor in Engineering Sciences

Advisors:

DIEGO CELENTANO

JAVIER SIGNORELLI

Santiago de Chile, October 2021

© 2021, Francisco Javier Alister Herdener



PONTIFICIA UNIVERSIDAD CATOLICA DE CHILE
SCHOOL OF ENGINEERING

PLASTIC ANISOTROPY AND FORMABILITY ESTIMATION IN ZINC SHEETS

FRANCISCO JAVIER ALISTER HERDENER

Members of the Committee:

DIEGO CELENTANO

DocuSigned by:

Diego Celentano

91CFB35EC4C442F...

JAVIER SIGNORELLI

DocuSigned by:

Javier Signorelli

8752CBA52FA9432...

MAGDALENA WALCZAK

DocuSigned by:

M Walczak

4404B94C10BD452...

DANIEL HURTADO

DocuSigned by:

Daniel Hurtado S.

4AD1C27AD1BB4B6...

JUAN VIVANCO

DocuSigned by:

Juan Vivanco

6C1D753FE0E94C6...

PIERRE-OLIVIER BOUCHARD

DocuSigned by:

Pierre-Olivier Bouchard

7EF73671A2BC4C9...

YADRAN ETEROVIC

DocuSigned by:

Yadran Eterovic S.

A20C7AE74678493...

This thesis submitted to the Office of Graduate Studies in partial fulfillment of the requirements for the Degree Doctor in Engineering Sciences

Santiago de Chile, October 2021

© 2021, Francisco Javier Alister Herdener

A quienes siempre han confiado en mí.

A quienes siempre me han apoyado.

A quienes siempre me ha amado.

A quienes hicieron todo para que llegara aquí.

A ti Pablo, a ti Lilliam, a ustedes, mis padres.

AGRADECIMIENTOS

A mis padres, Pablo y Lilliam, una vida no es suficiente para agradecerles lo que me han dado. A mis hermanos Claudio y Juan Pablo, por apoyarme siempre e incondicionalmente en la ruta de mi vida. A sus esposas Carolina y Francisca por hacerme parte de sus familias. A mis sobrinos Valentina, Raimundo, Trinidad, Lucas, Matías y Benjamín, sus risas cambian mi mundo. A Ángel, Rosi y Matías, la extensión de mi familia. A Javiera, mi compañera, gracias por tu guía y motivación permanente, por tu paciencia y sobre todo tu amor.

A Diego y Javier, mis profesores, gracias por su guía, compañía y amistad. Gracias por darme la confianza y espacio para discutir, crecer y aprender.

A mis amigos Marcelo Gutiérrez, Jorge Reyes y Carlos Álvarez, por su apoyo incondicional y fraternal amistad. A Víctor, María y sus padres, en especial Ezequiel y Sonia por su amistad y cariño desde el primer día. A Daniel Pino, Antonio Sánchez y Diego Uribe por su amistad, apoyo y guía. A personas entrañables como Cristián Vergara, Felipe Calderara, Cristián Henríquez, Ignacio Jeria, Matías Caces, el equipo RAL y el equipo COMPAS LAB. Muy especialmente a Ignacia Montes, José Eyzaguirre y Carlos Figueroa. Gracias a ellos por su amistad y confianza. A todas las personas del Departamento de Ingeniería Mecánica y Metalurgia: María Paz, Alejandra, Catalina, Anita, Leonardo, Manuel, Miguel Ángel, Ignacio, José y Patricio. Muchas gracias a cada uno de ustedes por su generosidad, confianza, ayuda y apoyo. Al equipo de IFIR, Martin Leonard y en especial a Emanuel Nicoletti. A Christophe Pradille por su apoyo. A Gilbert y Marc de CEMEF, por su amistad y ayuda. A Pierre-Olivier, por su generosidad y compromiso.

Finalmente, agradezco a la Comisión Nacional de Investigación Científica y Tecnológica, CONICYT, por su apoyo a través de la Beca Capital Humano Avanzado 2015, CONICYT-PCHA/2015-21150598 y los proyectos FONDECYT 1180591, FONDECYT 1130404 y ECOS-SUD CHILE C16E02.

ACKNOWLEDGEMENTS

To my parents, Pablo and Lilliam, one life is not enough to thank them for what they have given me. To my brothers Claudio and Juan Pablo, for always and unconditionally supporting me on the path of my life. To their wives Carolina and Francisca for making me part of their families. To my nephews Valentina, Raimundo, Trinidad, Lucas, Matías and Benjamín, their laughter changes my world. To Ángel, Rosi and Matías, the extension of my family. To Javiera, my partner, thank you for your guidance and permanent motivation, for your patience and above all your love.

To Diego and Javier, my teachers, thank you for your guidance, company and friendship. Thank you for giving me the confidence and space to discuss, grow and learn.

To my friends Marcelo Gutiérrez, Jorge Reyes and Carlos Álvarez, for their unconditional support and fraternal friendship. To Víctor, María and their parents, especially Ezequiel and Sonia for their friendship and affection from day one. To Daniel Pino, Antonio Sánchez and Diego Uribe for their friendship, support and guidance. To dear people such as Cristián Vergara, Felipe Calderara, Cristián Henríquez, Ignacio Jeria, Matías Caces, the RAL team and the COMPAS LAB team. Especially to Ignacia Montes, José Eyzaguirre and Carlos Figueroa. Thanks to them for their friendship and trust. To all the people of the Department of Mechanical Engineering and Metallurgy: María Paz, Alejandra, Catalina, Anita, Leonardo, Manuel, Miguel Ángel, Ignacio, José and Patricio. Many thanks to each of you for your generosity, trust, help and support. To the IFIR team, Martin Leonard and especially Emanuel Nicoletti. To Christophe Pradille for his support. To Gilbert and Marc from CEMEF, for their friendship and help. To Pierre-Olivier, for his generosity and commitment.

Finally, I thank the National Commission for Scientific and Technological Research, CONICYT, for their support through the 2015 Advanced Human Capital Grant, CONICYT-PCHA / 2015-21150598 and the projects FONDECYT 1180591, FONDECYT 1130404 and ECOS-SUD CHILE C16E02.

LIST OF PAPERS

This Thesis became from the research papers detailed below:

Paper 1, published: “Characterization of the elastoplastic response of low Zn-Cu-Ti alloy sheets using the CPB-06 criterion.” **Francisco Alister**, Diego Celentano, Javier Signorelli, Pierre-Olivier Bouchard, Daniel Pino and Marcela Cruchaga. Published in *Materials*, 2019, Volume 12, Issue 19, 3072-3086, DOI: <https://doi.org/10.3390/ma12193072>.

Paper 2, published: “Elastoplastic Characterization of Zn-Cu-Ti Alloy Sheets: Experiments, Modeling, and Simulation.” **Francisco Alister**, Diego Celentano, Emanuel Nicoletti, Javier Signorelli, Pierre-Olivier Bouchard, Daniel Pino, Christophe Pradille and Marcela Cruchaga. Published in *Journal of Material Engineering and Performance*, 2021, DOI: <https://doi.org/10.1007/s11665-021-06226-w>.

Paper 3, published: “Viscoplastic and Temperature Behavior of Zn-Cu-Ti Alloy Sheets: Experiments, Characterization, and Modeling.” **Francisco Alister**, Diego Celentano, Javier Signorelli, Pierre-Olivier Bouchard, Daniel Pino, and Marcela Cruchaga. Published in *Journal of Material Research and Technology*, 2021, Volume 15, 3759-3772, DOI: <https://doi.org/10.1016/j.jmrt.2021.09.132>

PROCEEDINGS

The findings of this research were presented at the following conference:

CONAMET-SAM 2019: “Estudio de la Formabilidad en Láminas de Zn20 en Caminos de Deformación Proporcionales con Aplicación de CPB-06”. XIX Congreso Internacional de Metalurgia y Materiales. Valdivia, Chile. Oral Presentation. **Francisco Alister**, Diego Celentano, Javier Signorelli, Pierre-Olivier Bouchard, Daniel Pino, and Marcela Cruchaga.

COCIM 2017: “Calibración del modelo de plasticidad CPB-06 aplicado a láminas de Zinc”. XVII Congreso Chileno de Ingeniería Mecánica. Santiago, Chile. Oral Presentation. **Francisco Alister**, Diego Celentano, Javier Signorelli, Pierre-Olivier Bouchard, Daniel Pino, and Marcela Cruchaga.

ENIEF 2017: “Aplicación del Criterio CPB-06 en la Modelación del Comportamiento Elastoplástico de Láminas de Zinc en el Ensayo de Tracción”. XXII Congreso de Métodos Numéricos y sus Aplicaciones. La Plata, Argentina. Oral Presentation. **Francisco Alister**, Diego Celentano, Javier Signorelli, Pierre-Olivier Bouchard, Daniel Pino, and Marcela Cruchaga.

JMC 2017: “Estimación del comportamiento mecánico de acero para embutición a través de modelos anisotrópicos asociados y no asociados”. XVI Jornadas de Mecánica Computacional. La Serena, Chile. Oral Presentation. **Francisco Alister**, Diego Celentano, Javier Signorelli, Marcela Cruchaga, Claudio García-Herrera and Julio Méndez.

INTERNATIONAL COOPERATION

This work was supported by the international cooperation with the following Institutions:

CEMEF: Centre de Mise en Forme des Matériaux, CEMEF, Sophia Antipolis, France. Internship of **Francisco Alister** in 2017, 2018 and 2019. Experimental procedures of the research under the direction of Pierre-Olivier Bouchard.

MIT: Massachusetts Institute of Technology, Crashworthiness Laboratory, Cambridge, USA. Internship of **Francisco Alister** in 2016. Implementation of the Modified Mohr-Coulomb damage model under the direction of Tomasz Wierzbicki.

IFIR: Instituto de Física Rosario, Rosario, Argentina. Experimental procedures performed by Emanuel Nicoletti under the direction of Javeri Signorelli from 2017 to 2020.

FUNDING

The development of this Thesis was possible by the funding provided by the following projects:

ECOS-SUD CHILE C16E02: “Non-Proportional Loading Conditions in Sheet Metal Forming: Modeling, Simulation and Experimental Validation.” International project between CEMEF UMR CNRS 7635, France and Pontificia Universidad Católica de Chile, Chile. **Francisco Alister** as a researcher.

FONDECYT 1180591: “Multiscale Analysis of Materials in Metal Forming Processes: Modeling, Simulation, and Experimental Validation.” Research project at and Pontificia Universidad Católica de Chile, Chile. **Francisco Alister** as a thesis student.

FONDECYT 1130404: “Modeling of Casting and Forming Processes: Simulation and Experimental Validation.” Research project at and Pontificia Universidad Católica de Chile, Chile. **Francisco Alister** as a thesis student.

CONICYT-PCHA/2015-21150598 SCOLARSHIP: “Programa Capital Humano Avanzado”. Scholarship for national doctoral programs. **Francisco Alister** as beneficiary.

MISTI-UC 2015: “Experimental and Numerical Analysis on Sheet Formability in Deep Drawing Processes.” International project between Crashworthiness Laboratory, MIT, USA, and Pontificia Universidad Católica de Chile, Chile. **Francisco Alister** as a researcher.

GENERAL INDEX

	Page
DEDICATORY	II
AGRADECIMIENTOS	III
ACKNOWLEDGEMENTS	IV
LIST OF PAPERS.....	V
PROCEEDINGS	VI
INTERNATIONAL COOPERATION	VII
FUNDING.....	VIII
TABLE INDEX.....	XII
FIGURE INDEX.....	XIII
1 INTRODUCTION	20
1.1 Motivation	20
1.2 Zn-Cu-Ti alloys	22
1.3 Sheet Metal Anisotropy.....	24
1.4 Plasticity Criterion.....	27
1.4.1 Brief Description of Yield Functions.....	29
1.4.2 Brief Description of Hardening Functions.....	34
1.5 Hypothesis and Objectives	35
1.5.1 Hypothesis	35
1.5.2 Objectives	35
1.6 Organization of the Thesis' Chapters.....	36
2 CHARACTERIZATION OF THE ELASTOPLASTIC RESPONSE OF LOW ZN- CU-TI ALLOY SHEETS USING THE CPB-06 CRITERION	39
2.1 Introduction	39
2.2 Materials and Methods	42
2.2.1 Material	42

2.2.2	CPB-06/Swift Elastoplastic Model	44
2.2.3	Fitting Procedure via the Tensile Test	46
2.2.4	Numerical Simulations of the Bulge Test	51
2.3	Results	52
2.3.1	Fitting Procedure	52
2.3.2	Bulge Test	55
2.4	Discussion	56
2.5	Conclusions	60
3	ELASTOPLASTIC CHARACTERIZATION OF ZN-CU-TI ALLOY SHEETS: EXPERIMENTS, MODELING, AND SIMULATION	62
3.1	Introduction	62
3.2	Materials and Methods	67
3.2.1	Material	67
3.2.2	Experimental Procedure	67
3.2.3	Constitutive model	75
3.2.4	Model Calibration Procedure	79
3.2.5	Numerical Simulation of the Shear and Bulge Tests	80
3.3	Results	82
3.3.1	Homogeneous State Range in the Tensile Test	82
3.3.2	Fitted Material Model Parameters from the Tensile Test	84
3.3.3	Shear Test	91
3.3.4	Bulge Test	93
3.4	Discussion	99
3.5	Conclusions	102
4	VISCOPLASTIC AND TEMPERATURE BEHAVIOR OF ZN-CU-TI ALLOY SHEETS: EXPERIMENTS, CHARACTERIZATION, AND MODELING. 104	104
4.1	Introduction	104
4.2	Materials and Methods	107
4.2.1	Material	107
4.2.2	Experimental Procedure	107
4.2.3	Constitutive Model	111
4.2.4	Model Calibration	115
4.3	Results and Discussions	119
4.3.1	Experimental Results	119

4.3.2	Numerical Results.....	125
4.4	Conclusions	134
5	CONCLUSIONS, PRESENT AND FUTURE WORKS	136
5.1	Conclusions	136
5.2	Present Work.....	137
5.3	Future Work	139
	REFERENCES.....	141

TABLE INDEX

	Page
Table I-1: General chemical composition of Zn-Ti-Cu alloys in weight percentage (Cauvin et al., 2018).	23
Table II-1: Experimentally measured mechanical properties of the Zn20 alloy (Jansen et al., 2013).	44
Table II-2: Swift fitted coefficients from the RD tensile curve.	52
Table II-3: CPB-06 fitted coefficients.	52
Table II-4: Numerical Lankford coefficients (R) and their relative errors.	53
Table II-5: RMSE of the fitting procedure in the true stress-strain curves and Lankford coefficients.	54
Table III-1: Mechanical properties of the Zn20 alloy.	69
Table III-2: Swift fitted coefficients.	85
Table III-3: CPB-06 fitted coefficients.	85
Table III-4: Experimental and Analytical Yield Values for main directions.	85
Table III-5: Experimental and Analytical Lankford values for main directions.	85
Table III-6: RMSE of the fitting procedure in the true stress-strain curves and Lankford coefficients for three main directions.	86
Table IV-1: Experiments performed.	108
Table IV-2: Johnson-Cook fitted coefficients.	126
Table IV-3: CPB-06 fitted coefficients.	126

FIGURE INDEX

	Page
Figure 1-1: Use of zinc world production. From www.ilzsg.org (<i>International Lead and zinc study group</i>).	20
Figure 1-2: Examples of zinc uses in architectural projects. Application in skin-like facades. From www.vmzinc.com	21
Figure 1-3: Optical micrography of Zn-Ti-Cu showing the marked texture and the TiZn ₁₆ inclusions. (Schlosser et al., 2019).	24
Figure 1-4: Reference axis in a rolled metal: RD – Rolling Direction or 0°, TD – Transversal Direction or 90°, and ND – Normal or Thickness Direction. From (Banabic, 2000).	25
Figure 1-5: Schematic representation of a tensile test sample on an arbitrary direction θ (Banabic, 2000).	26
Figure 2-1: Experimental true stress-strain tensile curves for RD, DD, and TD according to the data published in Jansen 2013 (Jansen et al., 2013).	43
Figure 2-2: Flow diagram of the fitting procedure.	47
Figure 2-3: Geometrical models and finite element meshes of the bulge test for the different analyzed dies.	52
Figure 2-4: Experimental and adjusted true stress-strain tensile curves (for all cases, the fitted curves are plotted in the whole strain range until fracture).	53
Figure 2-5: Plane stress yield envelope in the $\sigma_{xx} \sigma_{yy}$ plane at the yield strength for the von Mises, Hill-48, and CPB-06 criteria (the red circles denote the yield strengths for each sample direction).	55
Figure 2-5: Experimental and numerical strain paths on the major and minor strains diagram from the tensile and bulge test results.	56
Figure 3-1: Tensile specimen. Right: Experimental setup.	68
Figure 3-2: Left: Compression specimen. Center: Experimental setup. Right: DIC over the test.	71
Figure 3-3: Left: Experimental Rig. Right: Shear specimen.	72

Figure 3-4: Left: Masks used in the bulge test, from top to bottom $\beta=1.00$, $\beta=0.66$, and $\beta=0.33$. Right: Experimental setup.....	74
Figure 3-5: Schematic representation with dimensions for tensile, compression, and shear specimens (all samples in the same scale, dimensions in millimeters).....	75
Figure 3-6: Meshes and boundary conditions used in the finite element models. For the bulge tests, the sheet sample is grey, and the mask is green.....	81
Figure 3-7: Strain distribution over the sample length for RD, DD, and TD. The DIC images correspond to a) yield point, b) UTS, and c) OS-Necking.....	83
Figure 3-8: Yield loci for the $\sigma_1 - \sigma_2$ plane for all five directions based on the CPB-06 yield function. Experimental values at yield point with 0.002 strain offset for all tensile tests.	87
The adjusted true stress-strain curves, based on the CPB-06/Swift model, are presented in Figure 3-9.	88
Figure 3-9: Experimental and analytical hardening curves for all five directions.....	88
Figure 3-10: Experimental and analytical Lankford curves for all five directions.....	89
Figure 3-11: Experimental True Stress-Strain compression curves for TD.....	90
Figure 3-12: Shear test results. Top: Force - Displacement curves (Black solid line for numerical results). Bottom: In-plane shear strain plots (FEM simulations and DIC results).	92
Figure 3-13: Numerical and experimental strain-strain plots for all conditions.....	94
Figure 3-14: DIC and FEM major strain field (ϵ_1) for all masks and directions.....	96
Figure 3-15: Dome thickness evolution during bulge test for all conditions.....	98

Figure 4-1: Top: Strain-rate setup. Middle: The heating chamber for variable temperature experiments. Bottom: ASTM E8 test samples with speckle pattern.	110
Figure 4-2: Experimental engineering stress-strain curves for all experiments and conditions.	121
Figure 4-3: Experimental Lankford coefficient vs. engineering strain curves for all experiments and conditions.	123
Figure 4-4: Dispersion around the mean R value for all experiments and conditions.	124
Figure 4-5: Experimental and numerical true stress-strain plots all directions and conditions. From top to bottom: RD, DD, and TD, respectively.	128
Figure 4-6: Yield loci for all conditions at 0.10 of plastic strain for $\sigma_{xy} = 0$. Circles indicate the experimental yield value for both RD and TD in the respective condition (black: control, blue: medium strain, red: high strain, green: medium-temperature, and magenta: high temperature).	129
Figure 4-7: Experimental and numerical Lankford coefficient vs. plastic strain curves for all directions and conditions. From top to bottom: RD, DD, and TD, respectively.	132
Figure 4-8: True stress RMSE for each direction, condition, and repetition based on the numerical model.	133
Figure 4-9: Lankford coefficient RMSE for each direction, condition, and repetition based on the numerical model.	134
Figure 5-1: Prismatic die drawing samples for earing defect analysis.	138
Figure 5-2: Semispherical die drawing samples for shape and thickness reduction analysis.	139

PONTIFICIA UNIVERSIDAD CATOLICA DE CHILE
ESCUELA DE INGENIERIA

ANISOTROPIA PLASTICA Y ESTIMACION DE LA FORMABILIDAD EN
LAMINAS DE ZINC

Tesis enviada a la Dirección de Postgrado en cumplimiento parcial de los requisitos para el grado de Doctor en Ciencias de la Ingeniería.

FRANCISCO JAVIER ALISTER HERDENER

RESUMEN

El comportamiento del zinc, a diferencia de otros metales HCP como el titanio y el magnesio ha sido escasamente cubierto en la literatura. Para la lámina de aleación de zinc Zn20 estudiada en este trabajo (hasta 0.08% de titanio, mínimo de 0.06% de cobre con balance de zinc; porcentaje en peso), la anisotropía se aprecia claramente en las curvas tensión-deformación y los coeficientes de Lankford. Además, se ha observado que esta aleación muestra una fuerte influencia de la tasa de deformación y la temperatura en su comportamiento plástico, observando cambios significativos en la respuesta con pequeñas variaciones de estos parámetros. Estas propiedades imponen una caracterización rigurosa y una adecuada selección del modelo constitutivo para representar el comportamiento del material en simulaciones de conformado.

Esta investigación aborda la caracterización del comportamiento elastoviscoplastico y dependiente de la temperatura de la aleación Zn20 a través de una metodología que abarca caracterización experimental y modelado computacional. La caracterización incluye ensayos de tracción, compresión, corte y acopado hidráulico. Además, se realizaron pruebas de tracción con tres condiciones de tasa de deformación (0.002 , 0.02 y 0.2 s^{-1}) y temperatura (20 , 60 y $80 \text{ }^\circ\text{C}$). Para determinar el campo de deformación se utilizó el sistema de Correlación Digital de Imágenes o DIC en todos los experimentos. Los parámetros del modelo constitutivo, se obtienen con un procedimiento de calibración que considera las curvas de tensión-deformación en tracción y los coeficientes de Lankford. Además, se desarrollaron ensayos de compresión para análisis de asimetría.

El modelado se basa en el criterio de fluencia de Cazacu-Plunket-Barlat 2006 (CPB-06), en su forma asociada, y la ley de endurecimiento de Swift o Johnson-Cook. Tanto la función de fluencia como de endurecimiento, son ajustadas exclusivamente a partir de datos experimentales de los ensayos de tracción y compresión. En base a esto, el comportamiento elastoplástico, cuasi estático, se llevó a cabo mediante la ley de Swift, mientras que la dependencia a la tasa de deformación y la temperatura fueron cubiertos con el modelo de endurecimiento de Johnson-Cook. Los resultados experimentales de todos los ensayos de tracción se compararon con los modelos analíticos obtenidos de la aplicación de CPB-06 con la ley de endurecimiento de Swift o Johnson-Cook. La simulación numérica, realizada con el método de elementos finitos (FEM), se utilizó para validar la calibración previa con los modelos de ensayos de corte y acopado hidráulico.

Los resultados numéricos obtenidos muestran una buena descripción del comportamiento del material en los ensayos de corte y acopado hidráulico. Además, la evolución del campo de deformación en la prueba de acopado está adecuadamente representada por el modelo, independiente de la orientación de la muestra y la configuración de la máscara. Además, el resultado analítico muestra que el modelo constitutivo seleccionado puede representar la respuesta de la aleación en los ensayos de tracción para el comportamiento elastoviscoplastico y de temperatura. Así, finalmente, se concluye que la metodología propuesta proporciona un modelo robusto para describir la respuesta elastoplástica y dependiente de la tasa y la temperatura de láminas de Zn20 sujetas a diferentes condiciones de carga proporcional.

Miembros de la Comisión de Tesis Doctoral

Diego Celentano
Javier Signorelli
Magdalena Walczak
Daniel Hurtado
Juan Vivanco
Pierre-Olivier Bouchard
Yadran Eterovic

Santiago, Junio 2021

PONTIFICIA UNIVERSIDAD CATOLICA DE CHILE
ESCUELA DE INGENIERIA

PLASTIC ANISOTROPY AND FORMABILITY ESTIMATION IN ZINC
SHEETS

Thesis submitted to the Office of Graduate Studies in partial fulfillment of the
requirements for the Degree of Doctor in Engineering Sciences by

FRANCISCO JAVIER ALISTER HERDENER

ABSTRACT

The behavior of zinc, unlike other HCP metals such as titanium and magnesium, has been merely modeled in the literature. For the Zn20 zinc alloy sheet studied in this work (up to 0.08% of titanium, minimum of 0.06% of copper with a balance of zinc; weight percentage), the anisotropy is clearly seen on the stress-strain curves and Lankford coefficients. Besides, it has been experimentally observed that this alloy shows a strong influence of the strain rate and temperature on its plastic behavior. Furthermore, a significant change in the material response is seen with relatively small variations of these parameters. These features impose a rigorous characterization and an adequate selection of the constitutive model to represent the material behavior in metal forming simulations accurately.

This research drives the characterization of the elastoviscoplastic and temperature-dependent behavior of Zn20 alloy via a methodology that encompasses experimental characterization and numerical simulations. The characterization includes tensile, compression, shear, and bulge tests. Furthermore, tensile tests at three strain rates (0.002, 0.02, and 0.2 s⁻¹) and temperatures (20, 60, and 80 °C) were performed. Digital Image Correlation system (DIC) was used to determine strain fields in all experiments. The constitutive model parameters are obtained with a calibration procedure that accounts for the tensile stress-strain curves and Lankford coefficients. Besides, compression tests were performed to analyze asymmetric behavior.

The modeling is based on the Cazacu-Plunket-Barlat 2006 (CPB-06) yield criterion, in its associated form, and the Swift or Johnson-Cook hardening law, both the yield and hardening function, adjusted only from experimental data from the tensile and compression tests. The elastoplastic, quasi-static behavior was conducted by Swift law while the strain rate and temperature dependency were faced with the Johnson-Cook hardening model. The experimental results for all tensile tests were compared against the analytical models obtained from the application of CPB-06 with Swift or Johnson-Cook hardening law. The numerical simulation with the finite element method (FEM) validated the previous characterization with the shear and bulge tests models.

The obtained numerical results show a good description of the material behavior in the shear and bulge tests. Furthermore, the evolution of the strain field in the bulge test is well represented by the model regardless of the sample orientation and mask configuration. Furthermore, the analytical result shows that the selected constitutive model can drive the alloy response in tensile tests for the elastoviscoplastic and temperature behavior. Thus, it is finally concluded that the proposed methodology provides a robust model to describe the elastoplastic response of Zn20 sheets subject to different proportional loading conditions.

Members of the Doctoral Thesis Committee:

Diego Celentano
Javier Signorelli
Magdalena Walczak
Daniel Hurtado
Juan Vivanco
Pierre-Olivier Bouchard
Yadran Eterovic

Santiago, June 2021

1 INTRODUCTION

1.1 Motivation

Zinc is a hexagonal closed-packed metal (HCP) known for its corrosion resistance, based on a highly stable oxide form (zinc carbonate). Its primary use is galvanization process with 50% of the world production, followed by alloy production of bronze and brass with 17%; and other 17% for other zinc alloys. Finally, 6% of the world's production is used in construction (Semi-Manufacturers), where the alloy studied in this Thesis belongs (www.ilzsg.org, *International Lead, and zinc study group*).

Figure 1-1 details the uses of world zinc production.

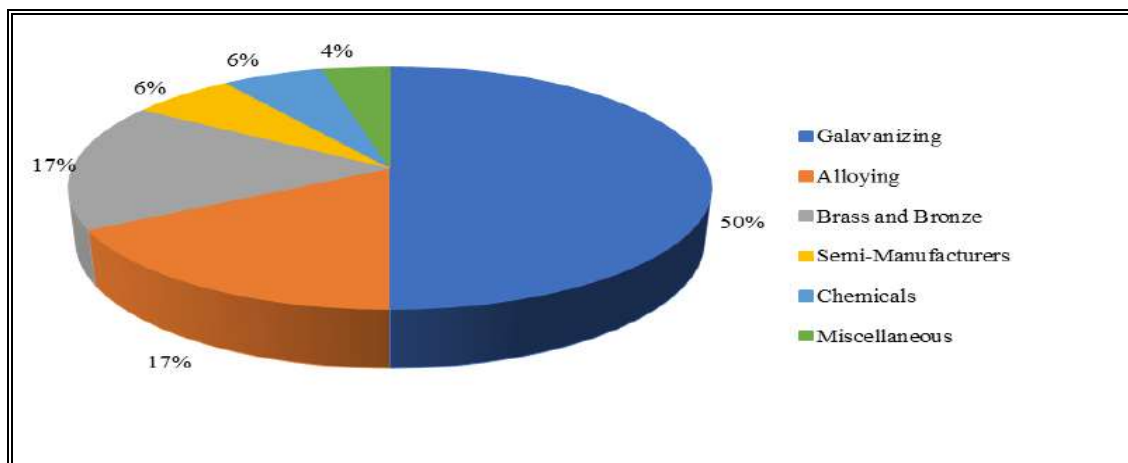


Figure 1-1: Use of zinc world production. From www.ilzsg.org (*International Lead and zinc study group*).

In the actual context, concerned with environmental protection policies and world pollution reduction, elements such as zinc are presented as alternative construction materials because they have a high recycling rate close to 90% (www.ilzsg.org). In addition, zinc alloys present high malleability, low fusion point (less expensive

production process), excellent and long-lasting aesthetic properties, and the possibility of creating avant-garde architecture projects with like-skin facades and complex shape covers. Figure 1-2 presents some examples of applications of zinc alloys in these types of projects.



Figure 1-2: Examples of zinc uses in architectural projects. Application in skin-like facades. From www.vnzinc.com.

The examples showed in Figure 1-2 made use of zinc alloys generally named Zn-Ti-Cu. In these alloys, the titanium is added in mass percentage from 0.005 to 0.2% to increase the mechanical resistance. The addition of copper improves the drawing aptitude of the alloy. However, the addition of titanium induces a strong texture in the alloy, expressed as a marked anisotropy.

Contrary to other HCP metals, the studies related to the zinc forming process have been poorly covered in the literature. Besides, there is a lack of information about the mechanical behavior of zinc and its alloys, and very few deal with numerical simulation in forming environments. However, the excellent properties of zinc alloys, its applicability to the building industry, the mechanical behavior in forming processes, and not yet broad-explored numerical characterizations allow studying and setting a phenomenological framework to drive numerical simulation that can estimate the material behavior in complex forming conditions, broadening the application field of these alloys.

In this Thesis, the complex mechanical behavior of a commercial zinc alloy, named Zn20 (up to 0.08% of titanium, minimum of 0.06% of copper with a balance of zinc; weight percentage), is studied under a phenomenological point of view using advanced yield criterion, quasi-static (Swift) and strain-rate and temperature-dependent (Johnson-Cook) hardening laws. This research presents an exhaustive material characterization based on tensile, shear, compression, and bulge test. Furthermore, the Digital Image Correlation system extends the comprehension of the alloy's behavior under the different tests. Finally, numerical simulations are carried out to verify the selection of the constitutive model and the projections of these tools to validate real forming conditions of the alloy in a simulated environment.

1.2 Zn-Cu-Ti alloys

As mentioned before, zinc is an HCP metal with an axis ratio c/a of 1.856, a density of 7.13 g/cm^3 , and a fusion temperature at normalized pressure of $419.35 \text{ }^\circ\text{C}$ (www.biom.org *Comité International des Poids et Mesures CIPM*). The primary

deformation mechanisms are dislocations and twinning. Twinning is an asymmetric mode of dislocation seen in specific thermomechanical conditions, as high temperature or high strain rates (Brunton & Wilson, 1969; Hosford & Allen, 1973).

Zinc is malleable up to 40% of the fusion temperature (in Kelvin degrees). Identical to other HCP metals, the base plane is usually placed in the sheet plane, and the c axis formed a 20° angle to the normal to this plane (Diot et al., 1998; Fundenberger et al., 1997; Philippe et al., 1991, 1994; Zhang et al., 2004). This alignment of the axis and the high c/a ratio, produced by the continuous rolling cold process, induces a high anisotropy in the sheet (Jansen et al., 2013; Pantazopoulos et al., 2013, 2017; Zhang et al., 2004).

The inclusion of titanium in Zn-Cu-Ti alloys creates TiZn_{16} precipitated elements, increasing the anisotropic features of these alloys (Faur & Cosmeleață, 2006; Vassilev et al., 2004). The incorporation of titanium raises the yield point of the alloy and the ultimate tensile strength; however, the corrosion resistance is compromised. Table I-1 shows the general chemical composition of commercial zinc alloys (Cauvin et al., 2018).

Table I-1: General chemical composition of Zn-Ti-Cu alloys in weight percentage (Cauvin et al., 2018).

Element	Zn	Ti	Cu
Composition (%)	Balance	≤ 0.08	≤ 0.06

Figure 1-3 shows a Zn-Ti-Cu alloy optical microscopy where the titanium precipitate can be observed (Schlosser et al., 2019).

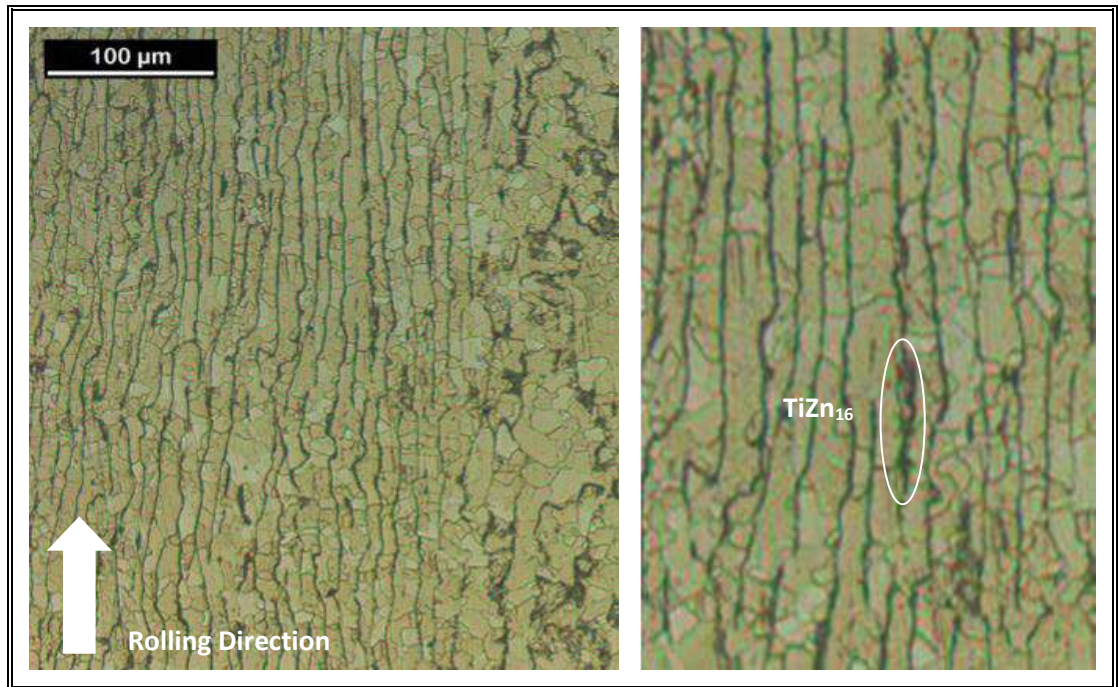


Figure 1-3: Optical micrography of Zn-Ti-Cu showing the marked texture and the TiZn_{16} inclusions. (Schlosser et al., 2019).

1.3 Sheet Metal Anisotropy

The thickness reduction induces transformation in the crystallographic texture of materials. As a result, the materials become anisotropic, which means that the mechanical properties depend on the material direction. The reference directions for metals in sheet formats are commonly defined, as shown in Figure 1-1. Here, the Rolling Direction or 0° is RD, the Transversal Direction or 90° is TD, and finally, the Normal Direction or Thickness Direction (ND), another specific direction is 45° from RD and is called Diagonal Direction (DD).

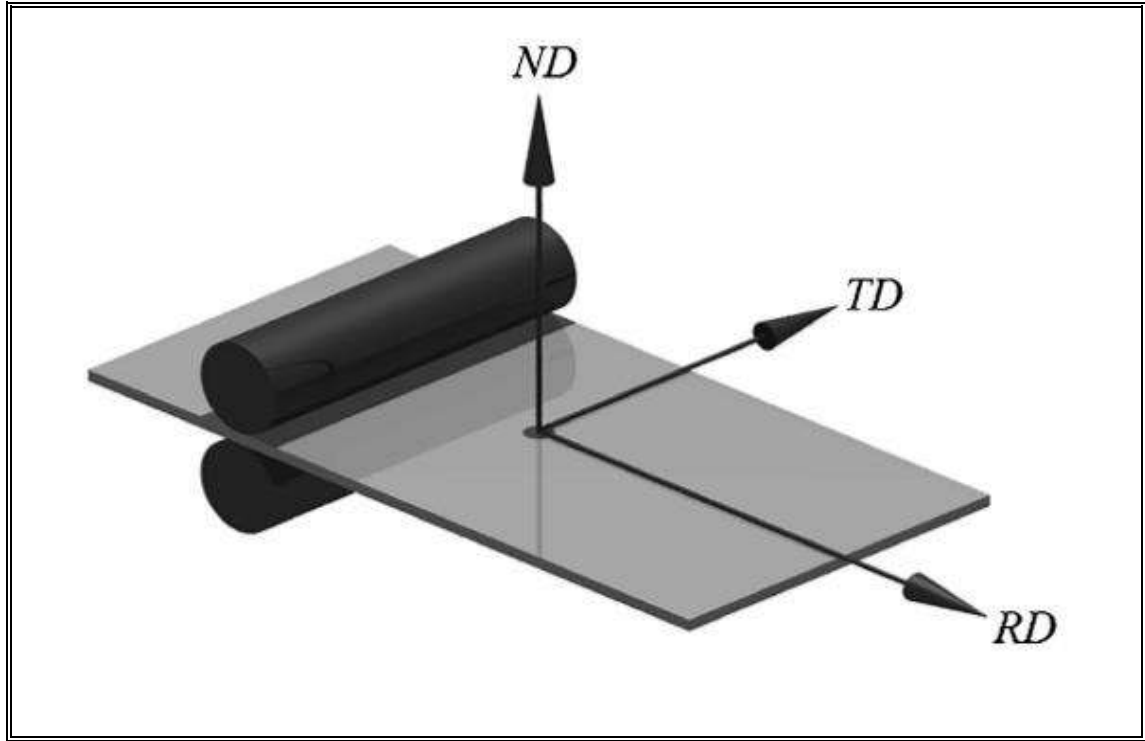


Figure 1-4: Reference axis in a rolled metal: RD – Rolling Direction or 0° , TD – Transversal Direction or 90° , and ND – Normal or Thickness Direction. From (Banabic, 2000).

A method to quantify the degree of anisotropy and the aptitude of a material to be formed was developed by Lankford (Lankford et al., 1950), who defines the R value as a measure of the thickness reduction rate against the width reduction rate in a uniaxial tensile test. The R values, considering plastic incompressibility or volume constancy (no change in volume due to plastic deformation process), can be defined as follows:

$$\varepsilon_{xx} + \varepsilon_{yy} + \varepsilon_{zz} = 0 \quad (1.1)$$

$$R = -\frac{\varepsilon_{yy}}{\varepsilon_{xx} + \varepsilon_{yy}} \quad (1.2)$$

where ε_{ii} are the normal strains, equation (1.1) is the application of plastic incompressibility, and (1.2) is the general definition of R values. In these expressions, the strain components are associated with the test sample axis, not with the material axis. A schematic representation of a test sample for a uniaxial tensile test is presented in Figure 1-5.

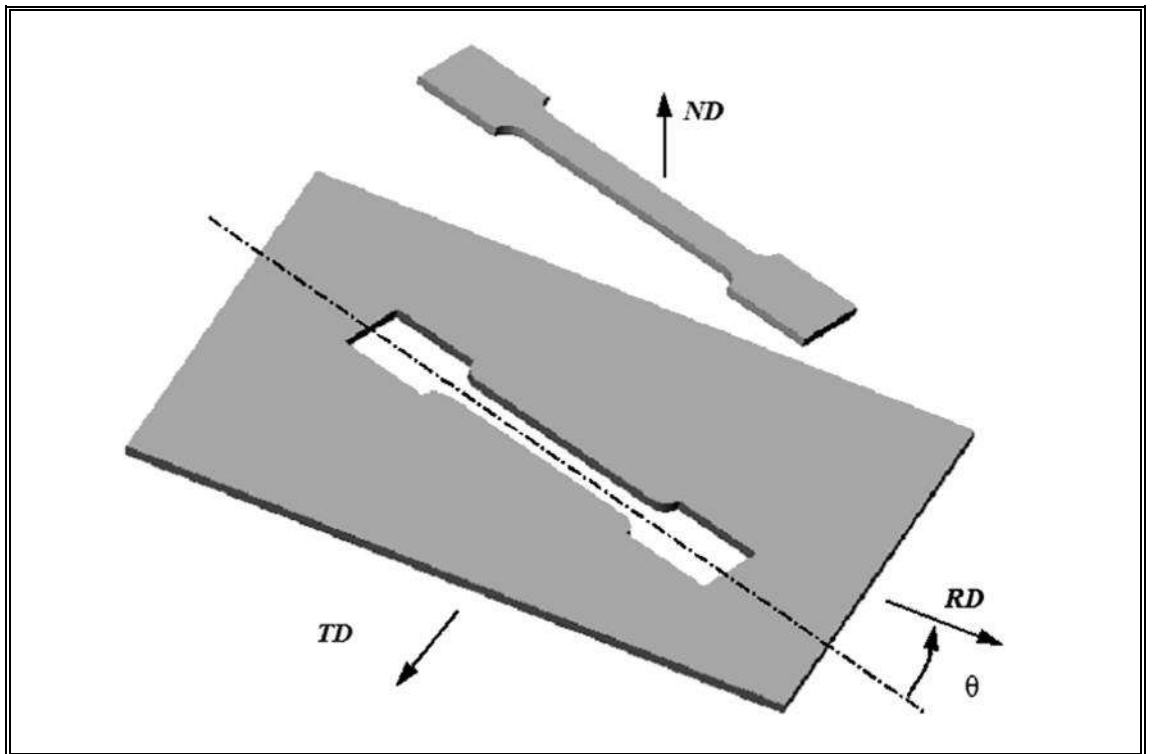


Figure 1-5: Schematic representation of a tensile test sample on an arbitrary direction θ (Banabic, 2000).

From Figure 1-5, the decomposition of the test sample principal strains over the samples axis system, drive to an equivalent expression for R value (1.2) that can be written as follows:

$$R_{\theta} = \frac{\varepsilon_{xx}\cos^2\theta + \varepsilon_{yy}\sin^2\theta + \varepsilon_{xy}\cos\theta\sin\theta}{\varepsilon_{xx} + \varepsilon_{yy}} \quad (1.3)$$

Taking into account an associated flow rule formulation, it is possible to define R values in terms of the stress components for a general case in the following form:

$$R_{\theta^\circ}^{num} = - \frac{\frac{\partial \bar{\sigma}}{\partial \sigma_{yy}[\gamma]}}{\frac{\partial \bar{\sigma}}{\partial \sigma_{xx}[\gamma]} + \frac{\partial \bar{\sigma}}{\partial \sigma_{yy}[\gamma]}} \quad (1.4)$$

In expression (1.4), the sample is loaded in the x -axis, $\bar{\sigma}$ is the equivalent stress and $\sigma_{ii}[\gamma]$ are the Cauchy Stress components in the material reference system.

The R values represent, at the same time, the plastic anisotropy of the sheet and its capability to deform without the presence of necking (fast reduction in thickness). Different R values for different directions mean plastic anisotropy, and their dispersion measures how anisotropic the material is. Besides, if R values are less than one (1) means a fast reduction in the thickness compared to the width under tensile loads, which means a poor aptitude to be formed. On the other hand, the higher the R value, the better the material for forming process. The determination of R values is, by convention, obtained at 20% of total strain, but with the use of the DIC system, it is possible to get the complete evolution of R values from the beginning of the test until fracture.

1.4 Plasticity Criterion

A plasticity criterion defines a condition (commonly based on stress) on which material goes from an elastic to a plastic state. The definition of three elements is needed to describe the plastic behavior of a material:

- The yield function that relates the stress components presented in the material at the time of yielding. This mathematical representation considers the complete

stress state to define the conditions at which the material starts to yield. In addition, the equivalent stress is obtained for each specific yield function. The equivalent stress is a scalar representation of a multidimensional stress state derived from the yield function. The yield criterion and equivalent stress can be expressed as:

$$F_{(\boldsymbol{\sigma}, \bar{\boldsymbol{\varepsilon}}_p)} = \bar{\boldsymbol{\sigma}}(\boldsymbol{\sigma}) - Y_{(\bar{\boldsymbol{\varepsilon}}_p)} = 0 \quad (1.5)$$

$$\bar{\boldsymbol{\sigma}}(\boldsymbol{\sigma}) = \left(\frac{f_{(\boldsymbol{\Sigma})}}{f_{(\gamma)}} \right)^{\frac{1}{a}} \quad (1.6)$$

In (1.1) $\bar{\boldsymbol{\sigma}}(\boldsymbol{\sigma})$ is the equivalent stress and $Y_{(\bar{\boldsymbol{\varepsilon}}_p)}$ is the hardening function. Here, if F is equal to 0, the material is in a plastic state. If F is lower than 0 is in an elastic state. Any value of F , bigger than 0, has no physical meaning. By its side, in (1.6) $f_{(\boldsymbol{\Sigma})}$ is the yield function, and $f_{(\gamma)}$ is the yield function for a uniaxial stress state in the reference direction, and a is the degree of homogeneity. The equivalent stress and equivalent strain need to fulfill the definition of plastic works according to the following expression:

$$\bar{\boldsymbol{\sigma}} \cdot \dot{\bar{\boldsymbol{\varepsilon}}}_p = \boldsymbol{\sigma}_m : \dot{\boldsymbol{\varepsilon}}_p \quad (1.7)$$

where $\bar{\boldsymbol{\sigma}}$ is the equivalent stress, $\dot{\bar{\boldsymbol{\varepsilon}}}_p$ is the equivalent plastic strain rate, $\boldsymbol{\sigma}_m$ is the Cauchy stress tensor, and $\dot{\boldsymbol{\varepsilon}}_p$ is the Cauchy strain rate tensor.

- A flow rule, which relates the stress components with the strain components of the material. The flow rule defines a bidirectional relation between the stress state and the strains. A flow rule can be either associated or non-associated. In

the case of this Thesis, an associated flow rule is considered. This means that the yield function, specifically the equivalent stress, is used to compute the strain components for a specific stress state. The strain components, as a result of the associated form, is expressed as:

$$\dot{\boldsymbol{\varepsilon}}_p = \dot{\lambda} \frac{\partial \bar{\sigma}}{\partial \boldsymbol{\sigma}_m} \quad (1.8)$$

where $\dot{\boldsymbol{\varepsilon}}_p$ is the strain rate tensor, $\dot{\lambda}$ is the plastic consistency parameter, $\bar{\sigma}$ is the equivalent stress, and $\boldsymbol{\sigma}_m$ is the Cauchy stress tensor.

- A hardening function to represent the evolution of the yield strength value as the plastic deformation process occurs. Hardening functions are mathematic expressions that associate the equivalent plastic strain with the increment of the strength in the material. A more complex function considers strain rate and temperature change to complement the plastic strain to define the new yield value. The hardening function is denoted as Y in Equation (1.5).

1.4.1 Brief Description of Yield Functions

This section made a brief description of some plasticity models. In-depth information can be obtained from the referred publications or in “*Formability of Metallic Materials*” (Banabic, 2000).

a) Von Mises

The Von Mises yield function is an isotropic model based on the observation that hydrostatic pressure cannot produce plastic deformation of the material (Von Misses,

1913). Von mises criterion is written for a general case in terms of the principal components of the Cauchy Stress Tensor is:

$$2\sigma_0^2 = (\sigma_1 - \sigma_2)^2 + (\sigma_2 - \sigma_3)^2 + (\sigma_3 - \sigma_1)^2 \quad (1.9)$$

For a plane stress condition, where $\sigma_{zz} = \sigma_{xz} = \sigma_{yz} = 0$ Von Mises takes the following form for a principal stress notation:

$$2\sigma_0^2 = (\sigma_1 - \sigma_2)^2 + \sigma_1^2 + \sigma_2^2 \quad (1.10)$$

For both equations (1.9) and (1.10), σ_0 the material's yield stress in the uniaxial tensile test.

b) Hill 1948

Proposed in 1948 by Rodney Hill (Hill, 1948). It is a quadratic anisotropic yield function derived from the isotropic criterion of Von Mises (Von Misses, 1913). The main advantage of this function is that all the anisotropic coefficients can be determined by the tensile test and the respective Lankford values. The general expression of Hill 1948 is:

$$F(\sigma_{yy} - \sigma_{zz})^2 + G(\sigma_{zz} - \sigma_{xx})^2 + H(\sigma_{xx} - \sigma_{yy})^2 + 2L\sigma_{yz}^2 + 2M\sigma_{xz}^2 + 2N\sigma_{xy}^2 = 1 \quad (1.11)$$

For a plane stress condition, where $\sigma_{zz} = \sigma_{xz} = \sigma_{yz} = 0$ the previous expression can be written in the following form:

$$F\sigma_{yy}^2 + G\sigma_{xx}^2 + H(\sigma_{xx} - \sigma_{yy})^2 + 2N\sigma_{xy}^2 = 1 \quad (1.12)$$

here, the anisotropic coefficients F, G, and H can be experimentally determined based on the following expressions of Lankford coefficients:

$$R_{0^\circ} = \frac{H}{G} \quad R_{45^\circ} = \frac{N}{F+G} - 0.5 \quad R_{90^\circ} = \frac{H}{F} \quad (1.13)$$

Finally, the anisotropic coefficient N is defined as:

$$N = (F + G)(R_{45^\circ} + 0.5) \quad (1.14)$$

c) Hill 1990

This criterion was developed by Hill in 1990 (Hill, 1990). It was written to face some issues of Hill 1948 and Hill 1979 (Hill, 1979) related to some aluminum alloys' behavior and the imposed coincidence of the principal stress with the material axis.

The expression of Hill 1990 for a plane stress case is:

$$\begin{aligned} & |\sigma_{xx} - \sigma_{yy}|^m + (\sigma_b^m / \tau^m) |(\sigma_{xx} - \sigma_{yy})^2 + 4\sigma_{xy}^2|^{\frac{m}{2}} + |\sigma_{xx}^2 + \sigma_{yy}^2 + \\ & 2\sigma_{xy}^2|^{\frac{m}{2}-1} [-2a(\sigma_{xx}^2 - \sigma_{yy}^2) + b(\sigma_{xx} - \sigma_{yy})^2] = (2\sigma_b)^m \end{aligned} \quad (1.15)$$

where σ_b is the equibiaxial stress, τ is the pure shear stress, and a , b and m are obtained from the following equations:

$$a = \frac{F-G}{F+G} \quad (1.16)$$

$$b = \frac{F+G+4H-2N}{F+G} \quad (1.17)$$

$$m = \frac{\ln [2(R_{45^\circ}+1)]}{\ln \left(\frac{2\sigma_b}{2\sigma_{45^\circ}} \right)} \quad (1.18)$$

where F, G, H, and N are the Hill 1948 coefficients defined in (1.13) and (1.14).

d) Barlat 1996

To face some problems with the plasticity of some aluminum alloys that couldn't be faced with Hill's functions, Barlat developed a new function (Barlat, Becker, et al., 1997; Barlat, Maeda, et al., 1997) based on the linear transformation proposed on his 1991 model (Barlat et al., 1991) to include anisotropy. This new function improves the accuracy of the yield surface in aluminum alloys. The Barlat 1996 criterion is written as:

$$\alpha_3(\Sigma_1 - \Sigma_2)^m + \alpha_1(\Sigma_2 - \Sigma_3)^m + \alpha_2(\Sigma_3 - \Sigma_1)^m = 2\sigma_e^m \quad (1.19)$$

where Σ_1 , Σ_2 , and Σ_3 are the principal components of the modified Cauchy Stress Tensor and α_k are equal to:

$$\alpha_1 = \alpha_x p_{11}^2 + \alpha_y p_{21}^2 + \alpha_z p_{31}^2 \quad (1.20)$$

$$\alpha_2 = \alpha_x p_{12}^2 + \alpha_y p_{22}^2 + \alpha_z p_{32}^2 \quad (1.21)$$

$$\alpha_3 = \alpha_x p_{13}^2 + \alpha_y p_{23}^2 + \alpha_z p_{33}^2 \quad (1.22)$$

by its side, the coefficients α_x , α_y , α_z and θ are defined as follows:

$$\alpha_x = \alpha_{x0} \cos^2 2\theta + \alpha_{x1} \sin^2 2\theta \quad (1.23)$$

$$\alpha_y = \alpha_{y0} \cos^2 2\theta + \alpha_{y1} \sin^2 2\theta \quad (1.24)$$

$$\alpha_z = \alpha_{z0} \cos^2 2\theta + \alpha_{z1} \sin^2 2\theta \quad (1.25)$$

$$\theta = \tan^{-1} \left(\frac{S_{11} - S_{22}}{S_{12}} \right) \quad (1.26)$$

e) Cazacu-Barlat 2004

In 2004, Cazacu and Barlat (Cazacu & Barlat, 2004) proposed an isotropic model that considered asymmetry in tension and compression that can be seen in some HCP metals. The expression of Cazacu-Barlat 2004 in terms of the second and third invariant of the Deviatoric Stress Tensor is:

$$(J_2)^{3/2} - cJ_3 = \tau_y^3 \quad (1.27)$$

where τ_y is the stress in a pure shear test and c is a scalar that represents the tension-compression asymmetry as follows:

$$c = \frac{3\sqrt{3}(\sigma_t^3 - \sigma_c^3)}{2(\sigma_t^2 - \sigma_c^2)} \quad (1.28)$$

here, σ_t and σ_c represents the yield stress at tension and compression, respectively.

f) Cazacu-Plunket-Barlat 2006 or CPB-06

Based on the previous models of Cazacu-Barlat 2004 and Barlat 1996 (Barlat, Becker, et al., 1997; Barlat, Maeda, et al., 1997; Cazacu & Barlat, 2004), Plunkett et al. (Plunkett et al., 2006) published the Cazacu-Plunket-Barlat yield function. This model considers the linear anisotropic transformation applied in Barlat 1996 and the asymmetric behavior of Cazacu-Barlat 2004. The CPB-06 is flexible enough to represent a spectrum of material behavior, from isotropic (Von Mises) to anisotropic materials, including asymmetric behavior. A complete and detailed description of CPB-06 can be found in (Cazacu et al., 2006; Plunkett et al., 2006, 2007, 2008). To avoid redundancy in the model's description used in this Thesis, refer to section 4.2.3 letter "a" for further details.

1.4.2 Brief Description of Hardening Functions

As was commented in the previous point, hardening functions represent the variation of the yield value due to the accumulated plastic strain. Therefore, the hardening functions can be based exclusively on the plastic strain, quasi-static models, or incorporate strain rate and temperature dependencies, dynamic models. A detailed review of different hardening functions can be found on (Larour, 2010).

a) Quasi-static

Some functions of this group are Swift (Swift, 1952), Voce (Voce, 1948), and Hockett-Sherby (Hockett & Sherby, 1975), all expressed as follows in the same order:

$$Y_{(\bar{\epsilon}_p)} = C_1(C_2 + \bar{\epsilon}_p)^{C_3} \quad (1.29)$$

$$Y_{(\bar{\epsilon}_p)} = C_1 + (C_2 - C_1)e^{(-C_3\bar{\epsilon}_p)} \quad (1.30)$$

$$Y_{(\bar{\epsilon}_p)} = C_2 - (C_2 - C_1)e^{(-C_3\bar{\epsilon}_p^{C_4})} \quad (1.31)$$

In equations (1.29) to (1.31), $\bar{\epsilon}_p$ is the equivalent plastic strain, and C_i are the coefficients of the hardening functions to be fitted.

b) Strain rate and Temperature-Dependent

As representative functions of strain rate and temperature-dependent hardening laws are Johnson-Cook (Johnson & Cook, 1983) and Johnson-Cook Modified (Kang et al., 1999), considering plastic strain, strain rate, and temperature.

$$Y_{(\bar{\varepsilon}_p, \dot{\varepsilon}_p, T^o)} = C_1 (C_2 + \bar{\varepsilon}_p)^{C_3} \left[1 + C_4 \ln \left(\frac{\dot{\varepsilon}_p}{\dot{\varepsilon}_{ref}} \right) \right] \left[1 - \left(\frac{T - T_{ref}}{T_{fusion} - T_{ref}} \right)^{C_5} \right] \quad (1.32)$$

$$Y_{(\bar{\varepsilon}_p, \dot{\varepsilon}_p, T^o)} = C_1 (C_2 + \bar{\varepsilon}_p)^{C_3} \left[1 + C_4 \ln \left(\frac{\dot{\varepsilon}_p}{\dot{\varepsilon}_{ref}} \right) + C_5 \left(\ln \left(\frac{\dot{\varepsilon}_p}{\dot{\varepsilon}_{ref}} \right) \right)^2 \right] \left[1 - \left(\frac{T - T_{ref}}{T_{fusion} - T_{ref}} \right)^{C_6} \right] \quad (1.33)$$

For the dynamic modes, $\bar{\varepsilon}_p$ is the equivalent plastic strain, $\dot{\varepsilon}_{ref}$ is the reference strain rate, T_{ref} is the reference temperature, T_{fusion} is the material melting point, and T is the actual temperature. Finally, C_i are the coefficients of the hardening functions to be fitted. It must be noted that $\bar{\varepsilon}_p$ and T needs to be higher than the reference values.

1.5 Hypothesis and Objectives

1.5.1 Hypothesis

This research is based on the hypothesis that the utilization of the CPB-06 yield criterion, in its associated form, will allow to numerically simulate the elastoplastic, elastoviscoplastic, and temperature-dependent behavior of Zn20 in different proportional loading paths under a phenomenological framework.

1.5.2 Objectives

The general objective of this research is:

- i) Represent, numerically, the elastoplastic, elastoviscoplastic, and temperature-dependent behavior of Zn20 alloy, using the associated form of CPB-06, under different proportional loading paths.

With this aim, the specific objectives of the Thesis are:

- i) Implement and fit CPB-06 yield criteria and Swift hardening law for a zinc alloy with previously reported results.
- ii) Perform a pool of experiments to generate a comparison basis for numerical simulations based on tensile, compression, shear, and bulge test to describe the Zn20 alloy applying the methodology defined in objective i).
- iii) Implement and fit the Johnson-Cook hardening law to describe the plastic behavior dependency of Zn20 alloy related to the strain rate and temperature based on the CPB-06 yield function.

1.6 Organization of the Thesis' Chapters

The present research focuses on the experimental and numerical description of the plastic behavior of Zn20 alloy. The work performed to accomplish this objective is described in three chapters detailed as follows:

- **Chapter 2:** Based on the paper “*Characterization of the Elastoplastic Response of Low Zn-Cu-Ti Alloy Sheets using the CPB-06 Criterion.*” This chapter focuses on the material characterization by presenting and applying the advanced Cazacu-Plunket-Barlat 2006 yield function combined with Swift hardening law. Firstly, the model parameters involved in the associate CPB-06/Swift constitutive model are fitted from published experimental data obtained from tensile tests. Secondly, these material parameters are assessed and validated in the simulation of the bulge test using different dies. The results

obtained with the CPB-06/Swift model show a good agreement with the experimental data reported in the literature.

- **Chapter 3:** Based on the paper “*Elastoplastic Characterization of Zi-Cu-Ti Alloy Sheets: Experiments, Modeling, and Simulation.*” This chapter is an extension of the work presented in Chapter I. Here the experimental data is generated through tensile, compression, shear, and bulge tests. The modeling is based on the Cazacu-Plunket-Barlat 2006 yield criterion and the Swift hardening law, presented in Chapter I with the same fitting procedure. Besides, compression tests were performed to search for evidence of asymmetric behavior. The numerical simulation, carried out with the finite element method (FEM), is used to validate the previous characterization with the shear and bulge tests models. In general, the obtained numerical results show a good description of the material behavior in the shear and bulge tests. The evolution of the strain field in the bulge test is well represented by the model regardless of the sample orientation and mask configuration.
- **Chapter 4:** Based on the paper “*Viscoplastic and Temperature Behavior of Zn20 Alloy Sheets: Experiments, Characterization, and Modeling.*” In this chapter, the influence of strain rate and temperature influence on the plastic behavior of Zn20 is studied to broaden the description done in previous chapters. The effects of strain rate and temperature are addressed through the Cazacu-Plunket-Barlat 2006 yield criterion and the Johnson-Cook hardening law. The tensile experiments were carried out for three strain rate conditions (0.002, 0.02,

and 0.2 s^{-1}) and three temperatures (20, 60, and $80 \text{ }^{\circ}\text{C}$). The proposed model calibration procedure describes the material responses adequately under the studied conditions, extending the characterization of the alloy in a non-previously covered environment.

2 CHARACTERIZATION OF THE ELASTOPLASTIC RESPONSE OF LOW ZN-CU-TI ALLOY SHEETS USING THE CPB-06 CRITERION

Published in *Materials*, 2019.

2.1 Introduction

Zinc is commonly used as a corrosion-resistant coating. However, it is also produced as thin sheets mainly used in architecture and construction as a roofing material, rain gutters, and decorative products. In addition to its corrosion resistance property, zinc shows high malleability, ductility, and high quality and durable surface finish. Despite these broad uses, there is a lack of studies and information concerning zinc sheet formability, in which the high c/a ratio may lead to a markable and evolving anisotropy in the plane of the blank as a consequence of the texture modification (Jansen et al., 2013; Pantazopoulos et al., 2013, 2017; Zhang et al., 2004).

Zinc has a Hexagonal Close Packed structure (HCP) for which the rolling process leads to a strong texture and slight local changes in the material induced by the manufacturing process (non-homogeneous cooling rates, local microsegregation of alloys, among others) often generate significant modifications of the microstructure. This material complexity leads to high strain and stress responses variability even on different samples over the same direction, as shown in (Milesi et al., 2017) and (Schlosser et al., 2017). For HCP metals, the rolling process produces an alignment of the c -axis normal to the rolling plane with a deviation of approximately 25° , inducing a high anisotropy in the sheet (Milesi et al., 2014). Specifically for the Zn-Cu-Ti alloy, the relation between the texture from the rolling process and the

bendability at different temperatures is discussed in (Philippe et al., 1991). Additionally, the texture evolution during a rolling process with an 80% reduction in thickness is reported in (Philippe et al., 1994) for the Zn-Cu-Ti alloy, comparing the texture components to those predicted by the Taylor evolution model.

Moreover, HCP materials show a Strength Differential (SD) effect due to the presence of the twinning deformation mechanism. This asymmetric process sets a different behavior in tension and compression (Hosford & Allen, 1973), so the yielding cannot be predicted with symmetric functions for all the expected forming conditions. Further studies were carried out on zinc alloys to define their formability via polycrystal models and necking criteria like the Marciniack-Kuczynski approach (Delannay et al., 2004; Schlosser et al., 2017; Schwindt et al., 2015).

To accurately describe the material behavior under general forming conditions, diverse anisotropic yield functions, thoroughly described in (Banabic et al., 2010), were developed during the last decades. Up to now, the formability of zinc sheets was driven by the use of constitutive models based mainly on the Hill-48 yield criterion combined with the Swift or Swift hardening laws, where both the yield function and hardening law are loading angle-dependent (Jansen et al., 2011, 2012, 2013, 2016; Milesi et al., 2014, 2017). The works cited made use of a “Fiber Vector” defined according to the direction of the major strain (Milesi et al., 2010). This approach allows the calculation of the yield function and hardening law coefficients for any direction, in particular, for the rolling (RD), diagonal (DD), and transverse (TD) directions. Although this approach has demonstrated a good agreement between experimental and numerical results, it requires a specific expression for each tested

direction, and, besides, it is unable to characterize the SD effect, which can be seen on several HCP metals. On the other hand, new asymmetrical yield functions have been developed to completely define the HCP behavior using a phenomenological approach (Li et al., 2015). One of these functions is the Cazacu-Plunket-Barlat 2006, i.e., the CPB-06 criterion (Cazacu et al., 2006; Plunkett et al., 2006), which is based on both, the generalization of the Barlat-96 function (Barlat, Maeda, et al., 1997) and the linear transformation of the Cauchy stress tensor proposed in (Barlat et al., 2005). The CPB-06 criterion introduces an asymmetry coefficient to account for the SD effect. Although this yield function was specifically formulated for HCP metals, it is flexible enough to model FCC and BCC materials. The CPB-06 criterion was first published by Plunkett (Plunkett et al., 2006) and described in detail later by Cazacu (Cazacu et al., 2006). Many applications of this yield function can be found for titanium, magnesium, and zirconium alloys (Cazacu et al., 2006, 2010; Chandola et al., 2015; Muhammad et al., 2015; Revil-Baudard et al., 2014; Tuninetti et al., 2012, 2015; Yoon et al., 2013) but none for zinc alloys.

In this work, the associated form of the CPB-06 yield criterion and the Swift hardening law are implemented in a finite element code to estimate the elastoplastic response of the low Zn-Cu-Ti alloy. To this end, a two-stage methodology is proposed. Firstly, the material characterization is performed via tensile test measurements available in (Jansen et al., 2013). As already mentioned, the material response associated with RD and TD samples shows notorious differences in hardening, increasing its value from RD to TD with intermediate values for DD samples. Moreover, the fracture strain is drastically reduced from RD to TD where,

besides, the Lankford coefficients are all less than one and significantly different for the three directions. The hardening coefficients are calibrated for RD, while the CPB-06 coefficients were fitted with an error minimization function that considers the stress-strain curves along with DD and TD and Lankford coefficients in RD, DD, and TD. Secondly, these material parameters are assessed in the simulation of the bulge test using different dies to validate the numerical model.

2.2 Materials and Methods

2.2.1 Material

The material used in this work is the low Zn-Cu-Ti alloy commercially known as Zn20. The RD, DD, and TD tensile samples were gathered from cold-rolled sheets of 1.0 mm thickness tested at a strain rate of 0.007 s^{-1} . The experimental true stress-strain tensile curves obtained and reported in (Jansen et al., 2013) are presented in Figure 2-1.

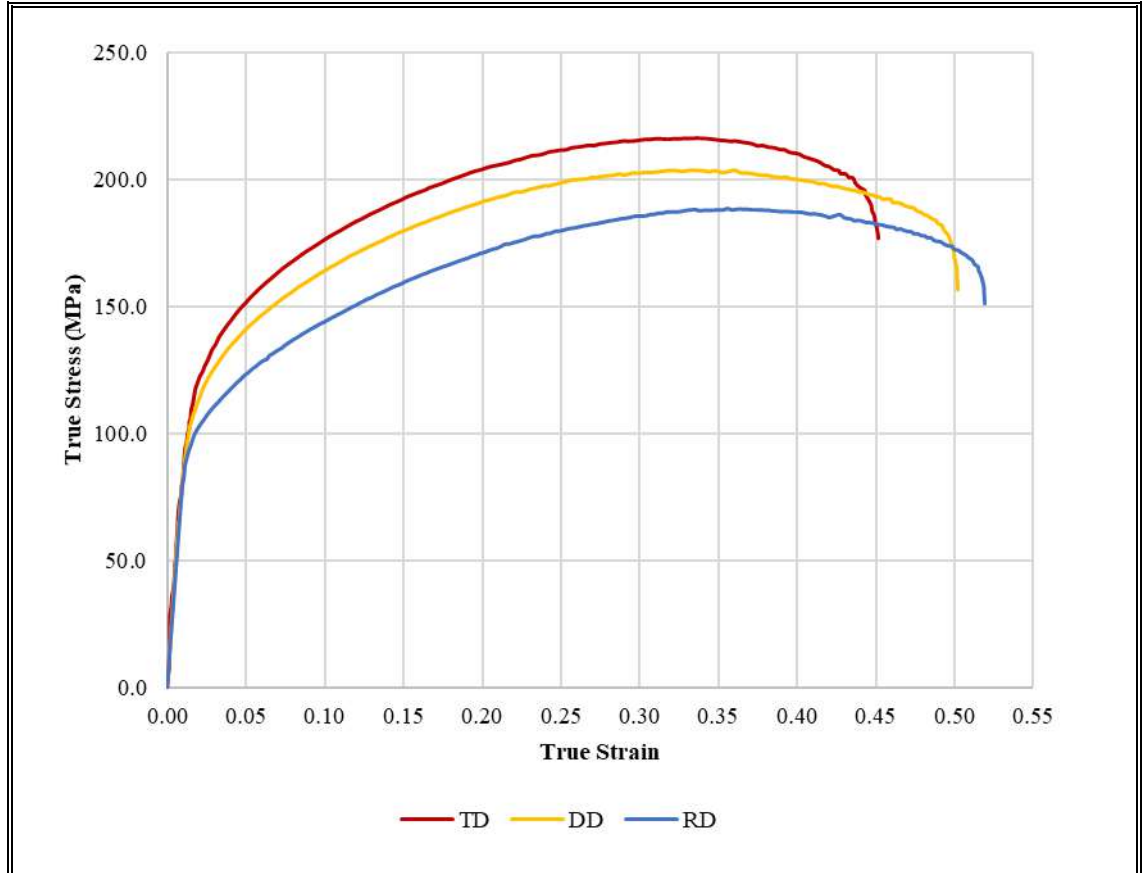


Figure 2-1: Experimental true stress-strain tensile curves for RD, DD, and TD according to the data published in Jansen 2013 (Jansen et al., 2013).

The mechanical properties, i.e., yield strengths and Lankford coefficients, of the Zn20 alloy sheet are presented in Table II-1. In addition, the Young modulus and Poisson ratio with respective values of 127.7 GPa and 0.23 were taken from (Tromans, 2011). These data are used in the fitting procedure to be presented in Section 2.2.3.

Table II-1: Experimentally measured mechanical properties of the Zn20 alloy
(Jansen et al., 2013).

Parameter	RD	DD	TD
σ_{yp} (MPa)	99.6	110.0	122.0
R	0.25	0.35	0.60

2.2.2 CPB-06/Swift Elastoplastic Model

The constitutive model used in this work is defined in the context of the associated flow rule and rate-independent plasticity with the standard elastoplastic strain decomposition (Celentano et al., 2012). RD and TD are assumed to be aligned with the x and y axes in the material reference system; thus, the z -axis defines the out-of-plane component. The CPB-06 yield criterion adopted to describe the material response is written as (Cazacu et al., 2006; Plunkett et al., 2006):

$$F_{(\boldsymbol{\sigma}, \bar{\boldsymbol{\varepsilon}}_p)} = \bar{\boldsymbol{\sigma}}(\boldsymbol{\sigma}) - Y(\bar{\boldsymbol{\varepsilon}}_p) = 0 \quad (2.1)$$

where $\bar{\boldsymbol{\sigma}}$ is the equivalent stress, $\boldsymbol{\sigma}$ is the Cauchy stress tensor, Y is the isotropic hardening stress, and $\bar{\boldsymbol{\varepsilon}}_p$ is the equivalent plastic strain. The equivalent stress is given by:

$$\bar{\boldsymbol{\sigma}}(\boldsymbol{\sigma}) = \left(\frac{f(\boldsymbol{\Sigma})}{f(\boldsymbol{\gamma})} \right)^{\frac{1}{\alpha}} \quad (2.2)$$

such that $f_{(\chi)}$, for $\chi = \boldsymbol{\Sigma}$ or $\chi = \boldsymbol{\gamma}$, is defined as:

$$f = (|\chi_1| - k\chi_1)^{\alpha} + (|\chi_2| - k\chi_2)^{\alpha} + (|\chi_3| - k\chi_3)^{\alpha} \quad (2.3)$$

where a is the degree of homogeneity, Σ_i are the principal components of the transformed stress tensor, γ_i are the modified anisotropic coefficients, and k is the asymmetry parameter (related, as already mentioned, to the SD effect). The reported expression for the transformed stress tensor Σ is given by:

$$\begin{pmatrix} \Sigma_{xx} \\ \Sigma_{yy} \\ \Sigma_{xy} \\ \Sigma_{zz} \\ \Sigma_{xz} \\ \Sigma_{yz} \end{pmatrix} = \begin{pmatrix} L_{11} & L_{12} & 0 & L_{14} & 0 & 0 \\ L_{12} & L_{22} & 0 & L_{24} & 0 & 0 \\ 0 & 0 & L_{33} & 0 & 0 & 0 \\ L_{14} & L_{24} & 0 & L_{44} & 0 & 0 \\ 0 & 0 & 0 & 0 & L_{55} & 0 \\ 0 & 0 & 0 & 0 & 0 & L_{66} \end{pmatrix} \begin{pmatrix} \sigma'_{xx} \\ \sigma'_{yy} \\ \sigma'_{xy} \\ \sigma'_{zz} \\ \sigma'_{xz} \\ \sigma'_{yz} \end{pmatrix}_{[m]} \quad (2.4)$$

where the components of \mathbf{L} tensor are the anisotropic coefficients and $\sigma'_{[m]}$ is the deviatoric part of the Cauchy stress tensor expressed in the material reference system $[m]$. The modified anisotropic coefficients γ_i are:

$$\gamma_1 = \left(\frac{2}{3}L_{11} - \frac{1}{3}L_{12} - \frac{1}{3}L_{14} \right) \quad (2.5)$$

$$\gamma_2 = \left(\frac{2}{3}L_{12} - \frac{1}{3}L_{22} - \frac{1}{3}L_{24} \right) \quad (2.6)$$

$$\gamma_3 = \left(\frac{2}{3}L_{14} - \frac{1}{3}L_{24} - \frac{1}{3}L_{44} \right) \quad (2.7)$$

Moreover, the hardening behavior is described through the Swift power-law written for RD as:

$$Y_{(\bar{\varepsilon}_p)} = K(\bar{\varepsilon}_0 + \bar{\varepsilon}_p)^n \quad (2.8)$$

where K is the strength coefficient, n is the hardening exponent (note that in this context, unlike other approaches (Jansen et al., 2011, 2012, 2013; Milesi et al., 2010,

2014), these two coefficients are only defined for RD) and $\bar{\varepsilon}_0 = \left(\frac{\sigma_{yp}^{RD}}{K} \right)^{\frac{1}{n}}$, σ_{yp}^{RD}

being the yield strength for RD (see Table 1). Also, the rate of the equivalent plastic strain is $\dot{\bar{\epsilon}}_p = \frac{\sigma_{[m]}\dot{\epsilon}_p}{\bar{\sigma}}$ such that $\boldsymbol{\epsilon}_p$ is the plastic strain tensor whose rate obeys the classical (objective, i.e., frame-indifferent) associated flow rule $\dot{\boldsymbol{\epsilon}}_p = \dot{\lambda} \frac{\partial \bar{\sigma}}{\partial \sigma_{[m]}}$, where $\dot{\lambda}$ is the plastic consistency parameter.

This model was implemented in an in-house finite element code with a radial-return scheme based on the Newton-Raphson iterative method (Celentano et al., 2012). The proposed model describes different strain path-dependent behaviors in a complete set of the bulge test. The computed numerical results show a good agreement with the experiments, as will be discussed in Section 4. Additionally, the present work improves previous studies on Zn-Cu-Ti sheet formability by fitting all directions using a unique set of parameters for the yield function and Lankford coefficients.

2.2.3 Fitting Procedure via the Tensile Test

The fitting procedure is based on the analytical expression for the stress and strain behavior on the unidirectional tensile test adopting the plane stress assumption. Thus, only σ_{xx} , σ_{xy} and σ_{yy} are different from zero. The steps involved in the methodology, summarized by the flow diagram in Figure 2-2, are described below.

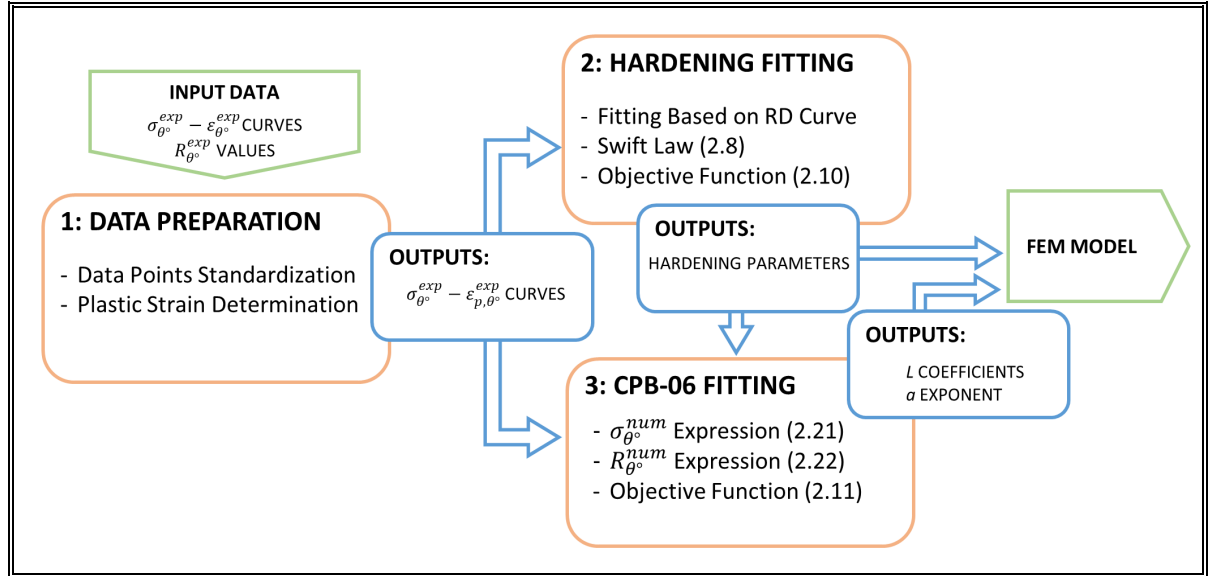


Figure 2-2: Flow diagram of the fitting procedure.

c) Data Preparation

The experimental data was considered until the Ultimate Tensile Stress (UTS) in the axial true stress-true strain ($\sigma_{\theta^\circ}^{exp} - \varepsilon_{\theta^\circ}^{exp}$) curves of the θ samples (i.e., $\theta=0^\circ$, 45° and 90° for RD, DD, and TD, respectively) for which a homogeneous state is assumed (Leonard et al., 2017). For simplicity, the same number of experimental ($\sigma_{\theta^\circ}^{exp} - \varepsilon_{\theta^\circ}^{exp}$) values m were considered for the curves of the three samples. In order to obtain the plastic component of the axial strain $\varepsilon_{p,\theta^\circ}^{exp}$ for stress beyond the yield strength, a simple decomposition was used:

$$\varepsilon_{p,\theta^\circ}^{exp} = \varepsilon_{\theta^\circ}^{exp} - \frac{\sigma_{\theta^\circ}^{exp}}{E} \quad (2.9)$$

where E is the Young modulus.

d) Hardening Fitting

The hardening parameters (K and n) are obtained through the minimization of the following objective function:

$$Error_Y = \sum_{i=1}^m \left(\frac{\sigma_{0^\circ}^{num}}{\sigma_{0^\circ}^{exp}} - 1 \right)_i^2 \quad (2.10)$$

where $\sigma_{0^\circ}^{num}$ is the numerical axial stress for the RD sample computed with the expression of $\sigma_{\theta^\circ}^{num}$ given in equation (2.21).

e) CPB-06 Fitting

The objective function proposed in (Barros et al., 2016) is also used here to obtain, through its minimization, the parameters involved in the CPB-06 model. A symmetric material response, i.e., $k=0$, is assumed since there is no experimental evidence of twinning for this alloy for low strain rates. Moreover, L_{11} equal to 1 was chosen (Cazacu et al., 2006, 2010; Chandola et al., 2015; Muhammad et al., 2015; Revil-Baudard et al., 2014; Tuninetti et al., 2012, 2015; Yoon et al., 2013) while L_{55} and L_{66} were also set to 1 due to the unavailability in this study of experimental results associated with the out-of-plane stress components. In summary, the CPB-06 parameters to be obtained are six L coefficients and exponent a . The objective function is written as:

$$Error_L = W_{45^\circ}^T \sum_{i=1}^m \left(\frac{\sigma_{45^\circ}^{num}}{\sigma_{45^\circ}^{exp}} - 1 \right)_i^2 + W_{90^\circ}^T \sum_{i=1}^m \left(\frac{\sigma_{90^\circ}^{num}}{\sigma_{90^\circ}^{exp}} - 1 \right)_i^2 + \\ W_{0^\circ}^R \sum_{i=1}^m \left(\frac{R_{0^\circ}^{num}}{R_{0^\circ}^{exp}} - 1 \right)_i^2 + W_{45^\circ}^R \sum_{i=1}^m \left(\frac{R_{45^\circ}^{num}}{R_{45^\circ}^{exp}} - 1 \right)_i^2 + W_{90^\circ}^R \sum_{i=1}^m \left(\frac{R_{90^\circ}^{num}}{R_{90^\circ}^{exp}} - 1 \right)_i^2 \quad (2.11)$$

where $R_{\theta^\circ}^{exp}$ and $R_{\theta^\circ}^{num}$ are the experimental and numerical Lankford coefficients of a θ sample, respectively, and W is a weighting factor. For simplicity, the weights W were set to 1 for the five terms of equation (2.11).

The minimization of expressions (2.10) and (2.11) is based on the non-linear Levenberg-Marquardt algorithm.

i) Numerical Stress $\sigma_{\theta^\circ}^{num}$

The numerical stress term is obtained from the general form of the equivalent stress given by equation (2.2), which can be written for a uniaxial tensile loading in the form of:

$$\bar{\sigma}(\sigma) = \left(\frac{f}{B_{\theta^\circ}} \right)^{\frac{1}{a}} \quad (2.12)$$

where the expressions for f and B_{θ° are:

$$f = \phi(\Sigma_1, \Sigma_2, \Sigma_3) = (|\Sigma_1| - k\Sigma_1)^a + (|\Sigma_2| - k\Sigma_2)^a + (|\Sigma_3| - k\Sigma_3)^a \quad (2.13)$$

$$B_{\theta^\circ} = \phi\left(\frac{1}{2}(\alpha + \beta), \frac{1}{2}(\alpha - \beta), \gamma\right) \quad (2.14)$$

where:

$$\alpha = (\varphi_1 + \varphi_2) \cos^2 \theta^\circ + (\psi_1 + \psi_2) \sin^2 \theta^\circ \quad (2.15)$$

$$\beta = \sqrt{((\varphi_1 - \varphi_2) \cos^2 \theta^\circ + (\psi_1 - \psi_2) \sin^2 \theta^\circ)^2 + 4(L_{33} \sin \theta^\circ \cos \theta^\circ)^2} \quad (2.16)$$

$$\gamma = \varphi_3 \cos^2 \theta^\circ + \psi_3 \sin^2 \theta^\circ \quad (2.17)$$

and:

$$\varphi_1 = \frac{1}{3}(2L_{11} - L_{12} - L_{14}) ; \quad \psi_1 = \frac{1}{3}(2L_{12} - L_{11} - L_{14}) \quad (2.18)$$

$$\varphi_2 = \frac{1}{3}(2L_{12} - L_{22} - L_{24}) ; \quad \psi_2 = \frac{1}{3}(2L_{22} - L_{12} - L_{24}) \quad (2.19)$$

$$\varphi_3 = \frac{1}{3}(2L_{14} - L_{24} - L_{44}) ; \quad \psi_3 = \frac{1}{3}(2L_{24} - L_{14} - L_{44}) \quad (2.20)$$

From (2.12), it can be seen that for $\theta^\circ = 0$ (RD), the condition $\bar{\sigma}_{(\sigma)} = \sigma_{0^\circ}$ is fulfilled. Besides, $\sigma_{\theta^\circ}^{num}$ can be written as:

$$\sigma_{\theta^\circ}^{num} = \left(\frac{B_{0^\circ}}{B_{\theta^\circ}} \right)^{\frac{1}{a}} Y(\bar{\epsilon}_p) \quad (2.21)$$

where $\left(\frac{B_{0^\circ}}{B_{\theta^\circ}} \right)$ includes the set of L coefficients to be fitted.

ii) Numerical Lankford Coefficients $R_{\theta^\circ}^{num}$

The numerical Lankford coefficients, considering the inherent plastic incompressibility of the model, are written as:

$$R_{\theta^\circ}^{num} = - \frac{\frac{\partial \bar{\sigma}}{\partial \sigma_{yy[r]}}}{\frac{\partial \bar{\sigma}}{\partial \sigma_{xx[r]}} + \frac{\partial \bar{\sigma}}{\partial \sigma_{yy[r]}}} \quad (2.22)$$

where the superscript r denotes the tensile test reference system such that the sample is loaded in the x -direction.

2.2.4 Numerical Simulations of the Bulge Test

Although the uniaxial test is crucial, assessing the proposed model under loading conditions representing real applications is also relevant. For this reason, the bulge test is used to study the material's mechanical response under biaxial loading.

According to the bulge tests carried out in (Jansen et al., 2013), three different dies with the following minor to major axis ratios β were used: 1.00 (equibiaxial), 0.50, and 0.33. In addition, for the $\beta=0.50$ and $\beta=0.33$ dies, samples with the major axis aligned with RD and TD were considered (the largest of the three dies was 120 mm). Therefore, five simulations were performed to replicate the experimental strain paths reported in (Jansen et al., 2013).

The complete domain was meshed with three sub-sets: the sheet sample, the die, and the sheet contact interface. The die was assumed to be rigid. For the sheet, 10,800 trilinear 8-noded hexahedral elements with B-bar integration to avoid numerical locking (Celentano et al., 2012) were used (considering 6 elements along with the thickness). Simultaneously, the die and contact interface were discretized with bilinear 4-noded quadrilateral elements, 2,160 for the die and 3,600 for the interface. The geometrical models and finite element mesh of the bulge test for the different analyzed dies are plotted in Figure 2-3.

As in the experiment, an internal pressure was prescribed on one side of the sheet. The sheet edges were restrained for all displacement. Coulomb friction is considered with a coefficient of 0.3 between the sheet and the die for all simulations.

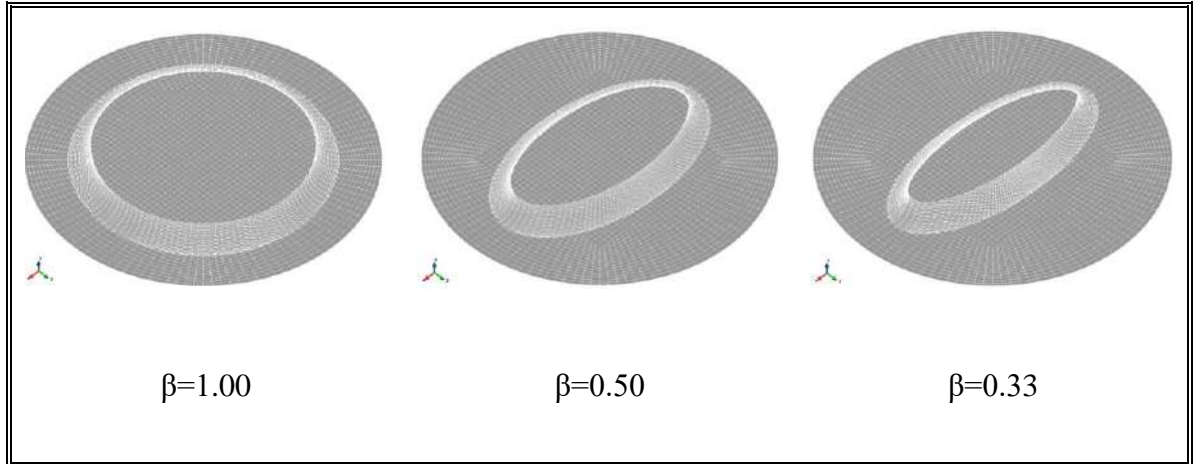


Figure 2-3: Geometrical models and finite element meshes of the bulge test for the different analyzed dies.

2.3 Results

2.3.1 Fitting Procedure

The obtained Swift and CPB-06 fitted coefficients are respectively presented in Tables II-2 and II-3.

Table II-2: Swift fitted coefficients from the RD tensile curve.

K (MPa)	ϵ_0	n
171.38	0.363	0.538

Table II-3: CPB-06 fitted coefficients.

L_{12}	L_{14}	L_{22}	L_{24}	L_{33}	L_{44}	a
0.1011	-0.2115	0.9141	-0.0156	0.8408	1.0346	6.0

The adjusted true stress-strain curves, based on the CPB-06/Swift model, are exposed in Figure 2-4.

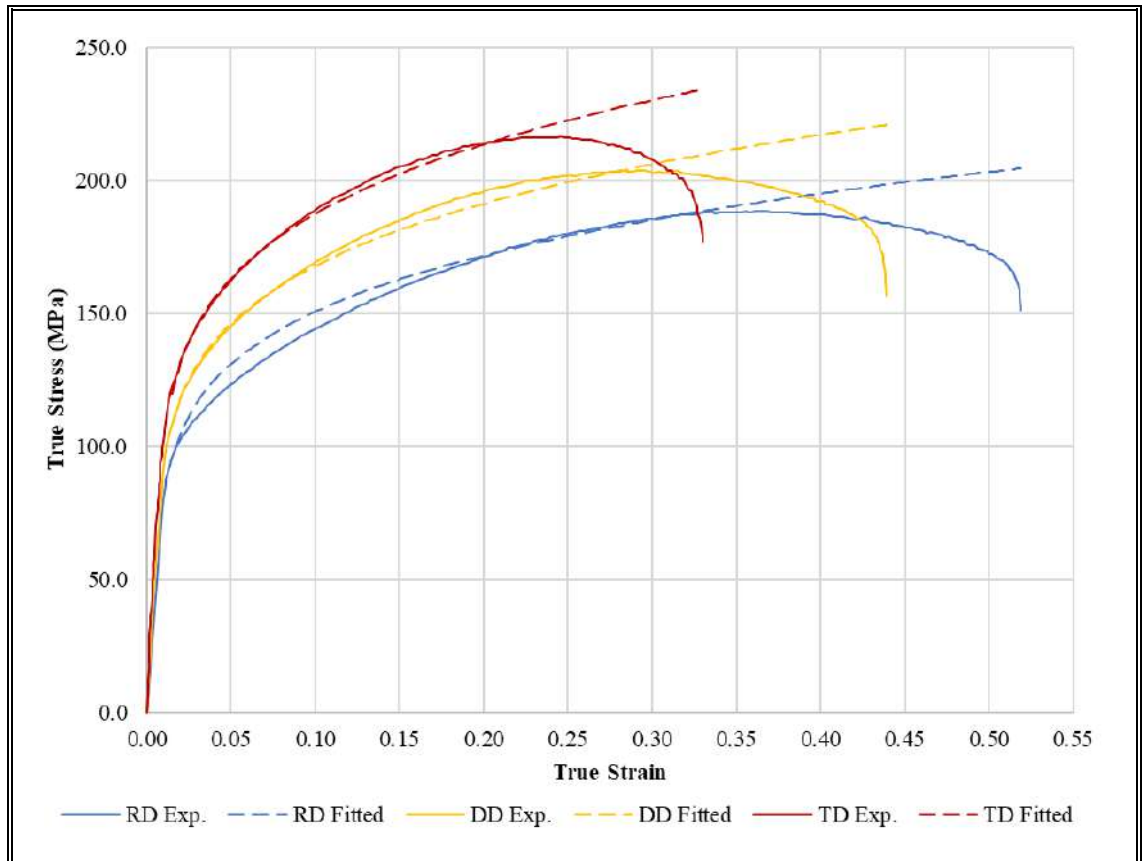


Figure 2-4: Experimental and adjusted true stress-strain tensile curves (for all cases, the fitted curves are plotted in the whole strain range until fracture).

The numerical Lankford coefficients obtained with the parameters reported in Tables II-2 and II-3 are summarized in Table II-4.

Table II-4: Numerical Lankford coefficients (R) and their relative errors.

Value	RD	DD	TD
R	0.25	0.35	0.60

Relative Error (%)	0.12	0.23	0.12
---------------------------	------	------	------

The error of the fitting procedure in the true stress-strain curves and Lankford coefficients for the three test directions can be assessed through the Root Mean Square Error (RMSE) given by the expressions:

$$E_{\sigma} = \sqrt{\frac{1}{m} \sum_{i=1}^m (\sigma_{\theta^{\circ}}^{num} - \sigma_{\theta^{\circ}}^{exp})^2} \quad (2.23)$$

$$E_R = \sqrt{\frac{1}{m} \sum_{i=1}^m (R_{\theta^{\circ}}^{num} - R_{\theta^{\circ}}^{exp})^2} \quad (2.24)$$

The obtained RMSEs for the true stress-strain curves and Lankford coefficients for the three test directions are shown in Table II-5.

Table II-5: RMSE of the fitting procedure in the true stress-strain curves and Lankford coefficients.

Value	RD	DD	TD
E_{σ} (MPa)	4.061	2.775	1.914
E_R	0.000	0.001	0.000

Figure 2-5 shows the plane stress yield envelope in the σ_{xx} and σ_{yy} plane (with $\sigma_{xy} = 0$) at the initiation of yielding for the von Mises, Hill-48, and CPB-06 criteria. The Hill-48 function is computed based on the R values shown in Table II-1.

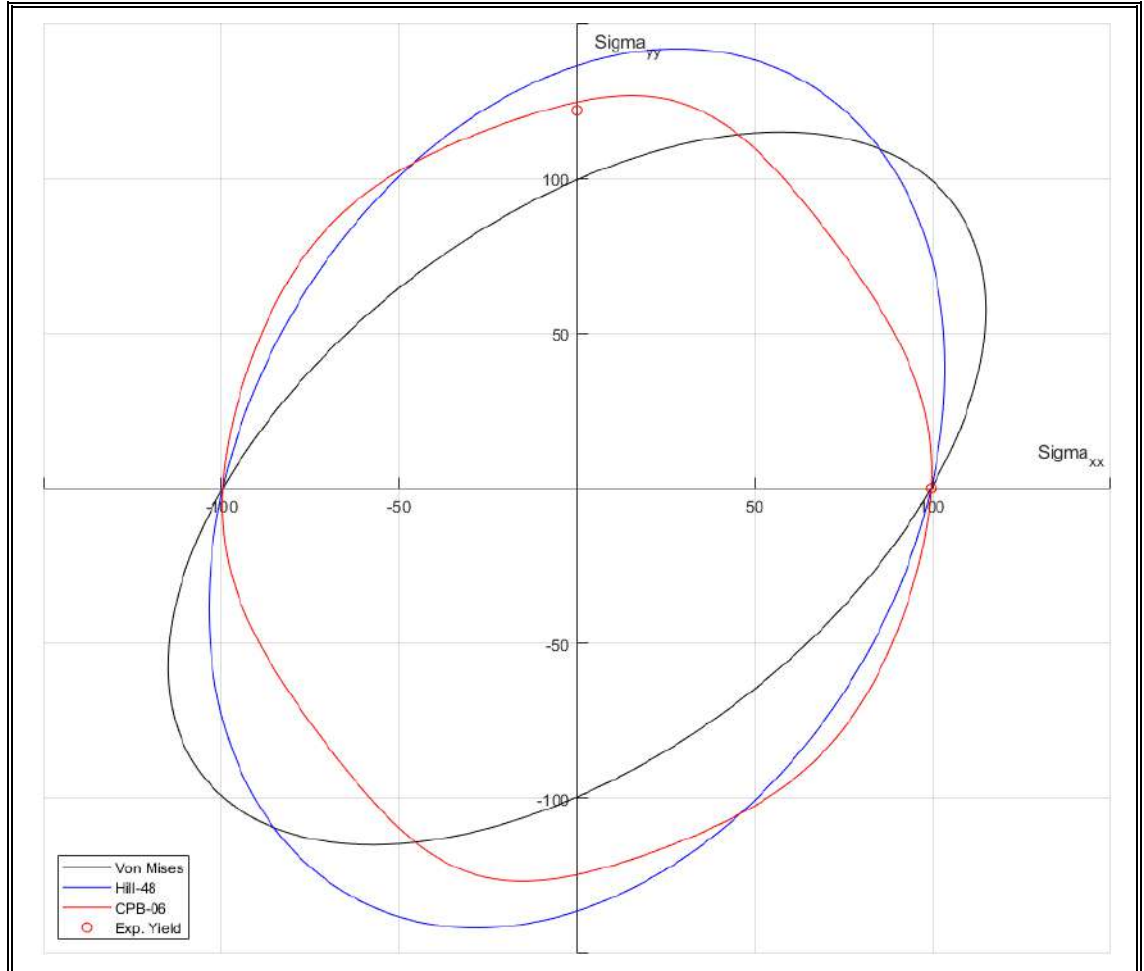


Figure 2-5: Plane stress yield envelope in the $\sigma_{xx} | \sigma_{yy}$ plane at the yield strength for the von Mises, Hill-48, and CPB-06 criteria (the red circles denote the yield strengths for each sample direction).

2.3.2 Bulge Test

The experimental and numerical strain paths on the major and minor strains diagram for the different dies and sample orientations are plotted in Figure 2-6 (the results from the tensile tests are also included for completeness). The experimental

measurements correspond to those reported in (Jansen et al., 2013). The numerical results were gathered from the central element of the outer side of the sheet.

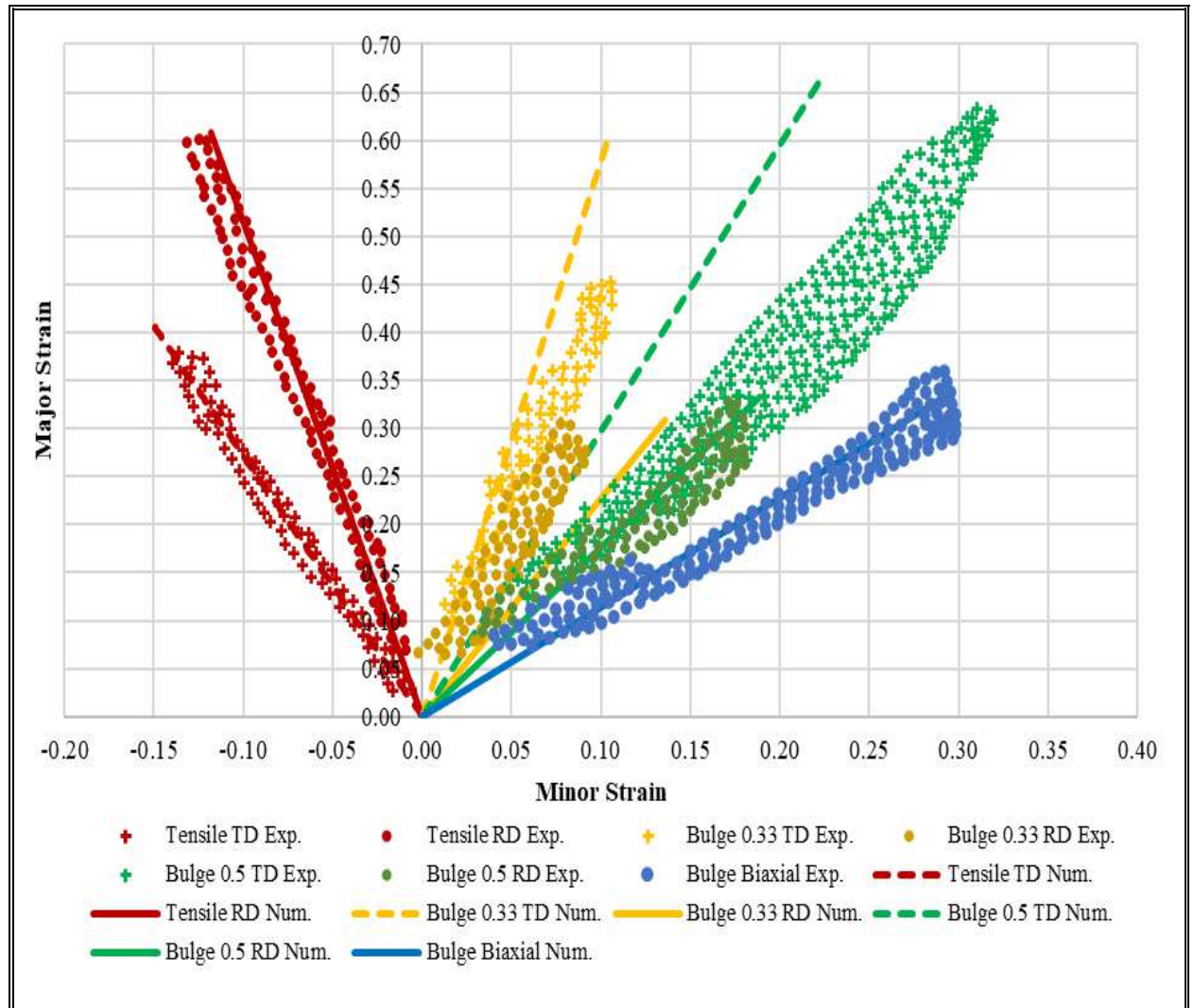


Figure 2-5: Experimental and numerical strain paths on the major and minor strains diagram from the tensile and bulge test results.

2.4 Discussion

The complexity of the anisotropy shown by zinc alloys requires the use of more elaborated elastoplastic constitutive laws. Thanks to the recent advances of the

material science community, we now dispose of a relatively large amount of different constitutive laws that can be used to study anisotropic materials like zinc alloys. These tools vary in complexity and, of course, in precision. As one might expect, more complex constitutive relationships often convey better precision. However, in a general way, it can be said that the more complex the material, the more considerable the number of material parameters that should be identified (Oya et al., 2014; Safaei et al., 2014; Stoughton & Yoon, 2009). Needless to say, that large amount of material parameters relies on complex and expensive experimental campaigns, which often do not meet the requirements of competitive industries. Additionally, the identification process of these material parameters is carried out through inverse analysis tools that typically lead to ill-posed problems. Thus, the challenge consists of obtaining a balance between complexity and precision.

As already mentioned, previous studies on zinc alloy formability face the material characterization using Hill-48 yield function and Swift or Swift hardening laws, separately fitted for each sample direction (Jansen et al., 2011, 2012, 2013, 2016; Milesi et al., 2014, 2017). Although the Hill-48 criterion is a simple anisotropic plastic model requiring a few material parameters, using independent models for the different loading directions increases the number of material parameters. Additionally, the implementation of such an approach in some numerical codes could be cumbersome.

The Swift hardening law simplifies implementing the constitutive model and the fitting process, showing a good agreement between the experimental and numerical stress-strain curves, with less than 4 MPa of RMSE for the RD (see Table II-5). It is

important to point out that the change in mechanical response in different directions other than RD is only driven by the yielding criterion CPB-06. The Swift hardening law identified from the RD data combined with the CPB-06 flow rule improves the fit of the hardening curve in the DD and TD. Thus, the RMSE in DD and TD is reduced by 50% compared to the RD (see Table II-5). This improvement can be seen qualitatively comparing the numerical predictions, and experimental data in the stress-strain curve plotted in Figure 4. The good agreement shown in Figure 2-4 up to the Ultimate Tensile Stress (UTS) is an encouraging result since it means that the damaging process of the material could eventually be captured by coupling the presented approach with some coupled non-local damage models (Bouchard et al., 2011; Cao et al., 2014; Peerlings et al., 1996).

An important feature of this approach is related to the change of the yielding locus induced by the CPB-06 yielding criterion. Figure 2-5 shows a comparison between the yielding surface in-plane biaxial stress (no shear) of different classic flow rules. The key features of the proposed approach are the anisotropic nature of the yielding criterion and the Strength Differential (SD) effect. In preliminary fitting runs, where the k parameter was set to 0 (neglecting SD effect), the error based on stress and Lankford was increased for all three directions. Specifically for TD, the fitted stress-strain curve over-estimated hardening while Lankford values decreased to 0.51. Assuming an asymmetric behavior (presence of SD effect) with a fitting of the k parameter, it is possible to match at the same time the stress-strain curves without compromising the estimation of the Lankford coefficients for all three directions (RD, DD, and TD).

It is also worth mentioning that the strain paths predicted by the model in the case of uniaxial loading present good agreement with the experimental data. Figure 2-6 shows the experimental and the numerical predictions of the strain path corresponding to the RD, the DD, and the TD uniaxial tests. A more quantitative way of looking at the quality of the prediction in terms of transversal strain is to look at the different Lankford coefficients (R). It can be seen in Table 4 that the predicted R values adequately agree with the corresponding experimental measurements given in Table II-1. The relative error in each Lankford coefficient is lower than 1%, which stems from how they have been defined. Thus, the RMSE is close to 0 for all three directions. The definition of Lankford coefficients as a function of L , k , and a leads to values that are almost the same as those experimentally determined. The previous results prove that the proposed approach can successfully predict the anisotropic mechanical response of the studied zinc alloy over different uniaxial loading directions.

Furthermore, these classic and simple experimental tests provide all the information required to calibrate the model. However, real-life applications involve mechanical loading that is much more complex. For instance, biaxial loading conditions are common in many material-forming industrial processes. The bulge test simulation (Section 2.3.2) is an interesting application involving the biaxial loading of the material sheet. The strain paths (experimental and numerical predictions) corresponding to the different elliptical dies used in the bulge test are plotted in Figure 2-6. On top of the aforementioned uniaxial strain paths, the numerical prediction of the equibiaxial loading condition also presents an excellent agreement

with experimental measurements (see blue data series in Figure 2-6). The bulge tests with elliptical dies can be divided into two sets of experiments using the material direction (RD or TD) oriented with the ellipse's long axis. For simplicity, these two sets of bulge tests are referred to as RD and TD, respectively.

The bulge RD tests present a slight deviation to the right of the experimental cloud point for the 0.5 dies but are highly displaced to the left for the 0.33. In the TD case, the numerically obtained curves slightly deviate to the left for the 0.33 die but, contrary to the RD situation, are highly displaced for the 0.5 die. The slope of the different strain paths denotes the behavior described above. In particular, a good experimental validation of the numerical model was obtained for the tensile test, bulge equibiaxial and bulge for paths $\beta=0.50$ -RD and $\beta=0.33$ -TD, where only the cases $\beta=0.50$ -TD and $\beta=0.33$ -RD exhibit minor differences.

2.5 Conclusions

The CPB-06/Swift associate constitutive model, in addition to the proposed fitting procedure, proves to be a valid and robust way to describe the elastoplastic anisotropic behavior of the Zn20 alloy. In this context, a unique set of anisotropic coefficients could reproduce the experimental tensile stress-strain curves and Lankford coefficients. The strain paths in the bulge test using different dies were properly validated for the equibiaxial, $\beta=0.50$ -RD, and $\beta=0.33$ -TD cases, while only approximate results have been obtained for the $\beta=0.50$ -TD and $\beta=0.33$ -RD cases. Together with the good approach of the stress-strain curves, these results reinforce using an associated flow rule to reproduce the anisotropy behavior of Zn20 sheets. The use of an associated flow rule simplifies the implementation of the constitutive

models, gives mathematical and physical consistency to the solution and reduces the complexity of the fitting process because of a reduction in the number of coefficients to be defined. Finally, the present work sets new steps to improve the predictability of more general forming conditions, including combined hardening laws and damage criteria.

3 ELASTOPLASTIC CHARACTERIZATION OF ZN-CU-TI ALLOY SHEETS: EXPERIMENTS, MODELING, AND SIMULATION

Published in *Journal of Materials Engineering and Performance*, 2021.

3.1 Introduction

Zinc alloys, especially the Zn-Cu-Ti alloy commercially known as Zn20, are Hexagonal Close Packed (HCP) materials that have become a cost-effective solution for constructors and architects, offering excellent corrosion resistance, malleability, and surface finish. Also, zinc alloys have a recycling rate of 95% for sheet format (www.zinc.org). Moreover, uses in biomedical applications were also reported (Niu et al., 2016). These features allow architects and engineers to develop complex and long-lasting designs with high aesthetic value and at a fraction of the cost of other scarcer metals. Despite these excellent properties and applicability, the zinc alloy's behavior is poorly covered in literature, and, as a consequence, few works address their elastoplastic behavior. Most of the works published for HCP materials focus on titanium, magnesium, or zirconium (Gilles, 2015; Paredes & Wierzbicki, 2020; Plunkett et al., 2006, 2007; Singh et al., 2018; Tuninetti et al., 2015; Tuninetti & Habraken, 2014).

The zinc alloy texture, resulting from the rolling process, leads to high variability of the strain and stress responses that increase the difficulty of correctly characterize this material. In particular, this alloy exhibits a high anisotropic response reflected in the Lankford coefficients with values below 1 and notoriously different between directions, limiting its use in forming process.

Many authors have worked on the description of this anisotropy, from the crystal scale to phenomenological studies. From the crystal scale, Cauvin et al. (Cauvin et al., 2018) used the viscoplastic self-consistent (VPSC) approach together with the EBSD technique to numerically replicate the evolution of texture and Lankford coefficients. Signorelli and coworkers (Schwindt et al., 2015; Signorelli et al., 2019) applied the VPSC model together with Marciniack-Kuczynski (M-K) criterion to define the forming limit curve (FLD) of the Zn20 alloy. Borodachenkova et al. (Borodachenkova et al., 2015) used the VPSC to represent the zinc alloy mechanical behavior in a forward-reverse shear experiment and the influence of shear deformation on the material hardening. Zhang et al. (Zhang et al., 2004) considered the Taylor model to determine the texture evolution due to the Zn-Cu-Ti alloy rolling process. Schlosser et al. (Schlosser et al., 2017) presented an exhaustive crystallographic analysis of the texture evolution and its influence on the anisotropy of Zn20 sheets. Wu et al. (Z. Wu et al., 2018) studied the Zn-Al alloy's creep resistance and mechanism in different temperature scenarios. Philippe et al. (Philippe et al., 1991) analyzed a Zn-Cu-Ti alloy under different temperatures and tensile loadings, showing the texture changes and deformation mechanisms involved in each case. Philippe et al. (Philippe et al., 1994) employed the Taylor model to predict the texture evolution in a Zn-Ti-Cu alloy under a cold rolling process with 80% thickness reduction. Diot et al. (Diot et al., 1998) worked over a Zn-Cu-Ti alloy, studying the evolution of texture in the thickness and explaining the mechanism involved. Delannay et al. (Delannay et al., 2004) studied, experimentally and numerically, the springback effect on textured zinc sheets using the LAMEL polycrystal plasticity

model. Florando et al. (Florando et al., 2006) analyzed the slip system activity in single-crystal zinc using a 3D DIC (Digital Image Correlation) system as a basis to analytically calculate the slip activity in the deformed crystals. More recently, Leonard et al. (Leonard et al., 2020) showed that the continuous dynamic recrystallization mechanism appears as a critical factor to explain the grain fragmentation process and the weakening of the texture observed during straining of Zn-Cu-Ti alloy sheets.

Additionally, copper is entirely soluble in zinc at low concentrations, and titanium forms the intermetallic phase TiZn_{16} (Vassilev et al., 2004). Faur and Cosmeleață (Faur & Cosmeleață, 2006) showed that increasing copper and titanium decreases the amount of twinning and enhances a grain refinement process by the presence of the secondary phase TiZn_{16} . This remark is entirely compatible with the VPSC simulations obtained by Roatta et al. (Roatta et al., 2020) for tensile and shear tests at different loading directions. This lack of twinning activity is consistent with the lack of asymmetry in this zinc alloy's tension/compression response. These works have provided valuable information explaining zinc alloys' behavior, the main deformation mechanisms involved, and the influence of different conditions (due to production or environmental factors) affecting these alloys' elastoplastic behavior. However, this type of approach in the forming process industry seems still far from phenomenological studies, which, are generally easier to implement and calibrate. To describe zinc alloys' elastoplastic behavior from a phenomenological standpoint, Vitu et al. (Vitu et al., 2018) compared the stress-strain curves obtained from bulge test experience on the traditional approach (dome curvature and thickness) and

measurements from 3D DIC. Jansen et al. (Jansen et al., 2011) proposed using the Hill-90 yield function and the Modified Maximum Force Criterion to numerically obtain the FLD of a zinc alloy. This work considered modifying the equivalent stress with in-plane angle-dependent coefficients that define the so-called - *fiber vector* - (Milesi et al., 2010). Later, Jansen et al. (Jansen et al., 2012) applied the previous procedure and methodology to simulate the stamping process of a cross sheet specimen of a zinc alloy, here using the Hill-48 constitutive model and a fracture model based on the Hill-90 criterion. Continuing with this work, Jansen et al. (Jansen et al., 2013) presented a stress-based FLD with a formulation exclusively written in terms of the Hill-48 criterion and Swift hardening law. The simulations were carried out on bulge tests. In this case, both the yield function and hardening law are angle-dependent. In further work, Milesi et al. (Milesi et al., 2014) applied the methodology as mentioned above to an industrial forming case, showing a good agreement between the predicted failure areas and the experimental evidence. The work of these researchers is complemented with the study of the influence of the adopted constitutive model on the prediction of earing in a cup drawing experience (Jansen et al., 2016). These studies have shown a good agreement between the numerical and experimental results despite the modeling requires a specific expression for each tested direction since it is based on the - *fiber vector* -. Extending the work of Jansen and Milesi, Alister et al. (Alister et al., 2019) recently applied the Cazacu-Plunket-Barlat 06 (Cazacu et al., 2006; Plunkett et al., 2006, 2008), CPB-06 for short, yield criterion to firstly characterize via tensile tests and then numerically describe the strain paths on the bulge test of Zn20 alloy sheets.

The CPB-06 criterion is a non-quadratic function that introduces an asymmetry coefficient to account for the Strength Differential effect (SD effect) observed under specific conditions in HCP structures (Cazacu et al., 2006; Plunkett et al., 2006, 2008). Although this function was specifically formulated for HCP metals, it is flexible enough to model FCC and BCC materials. The application of the CPB-06 yield function can be extensively found in titanium, magnesium, and zirconium alloys (Cazacu et al., 2006, 2010; Chandola et al., 2015; Muhammad et al., 2015; Revil-Baudard et al., 2014; Tuninetti et al., 2012, 2015; Yoon et al., 2013), and except for (Alister et al., 2019), none on zinc alloys. While the implementation and characterization of the Hill-48 yield function are relatively simple (Hill, 1948), it is not well suited to estimate the behavior of metals with Lankford coefficients below 1, a fact that leads to the use of other functions such as the CPB-06 criterion (Cheng et al., 2017; Nurcheshmeh & Green, 2016).

From a phenomenological point of view, this work aims to characterize the elastoplastic response of Zn20 alloy sheets with a proposed methodology that accounts for experiments and constitutive modeling that includes material parameters calibration and numerical simulations of them oriented to experimental validation of the computed predictions. To this end, tensile, compression, shear, and bulge tests are firstly carried out. Then, the associated form of the CPB-06 yield criterion and the Swift hardening law are fitted from the experimental tensile stress-strain curves and Lankford coefficients along with five directions with respect to the rolling direction of the sheet. Besides, a compression test is made to determine the presence or absence of asymmetric behavior.

The material, experimental procedure, constitutive model, and calibration procedure are described in Section 3.2. Afterward, this characterization is assessed and experimentally validated in the numerical simulation via the finite element method (FEM) of the shear and bulge tests. The experimental-numerical comparison is performed with the following results from the shear test: shear force-displacement curve and shear strain contours. The comparison from the bulge test is driven by plots of the strain path and major strain and thickness reduction in terms of the dome height. These results are presented and discussed in Sections 3.3 and 3.4, highlighting the numerical model's capabilities and limitations. Finally, Section 3.5 summarizes the main conclusions drawn from this work.

3.2 Materials and Methods

3.2.1 Material

The material used in this work is the low Zn-Cu-Ti alloy sheet named Zn20 (0.08% or less of titanium and 0.06% and upper of copper with a balance of zinc; percentage in weight) produced as sheets in a semi-continuous cast and rolling process with a nominal thickness of 0.65 mm.

3.2.2 Experimental Procedure

a) Tensile Test

The tensile test was performed in an Instron 5967 Universal Testing machine, equipped with a 30 kN load cell. The shape of the sample is chosen according to the ASTM E8-8M standard. Samples were stretched with a constant strain rate of 0.002 s⁻¹ at room temperature (20 °C).

A 3D Digital Image Correlation (3D DIC) system, VIC 3D 8 by Correlated Solutions, was used to capture the displacement fields. The measured area for which all the information was retrieved is placed on the gauge section, avoiding the sample's boundaries. The system is provided with two high-resolution cameras (Point Grey Grasshopper, 4.0 Megapixels at 10 fps) to measure both the in-plane and out-of-plane displacement and strain fields. As post-process parameters, the grid and step size were set on 19 and 3 pixels, respectively. The load data was recorded for each time step and frame using an analog-digital converter provided by National Instruments. Figure 3-1 shows the samples with the speckle pattern and experimental setup, respectively.

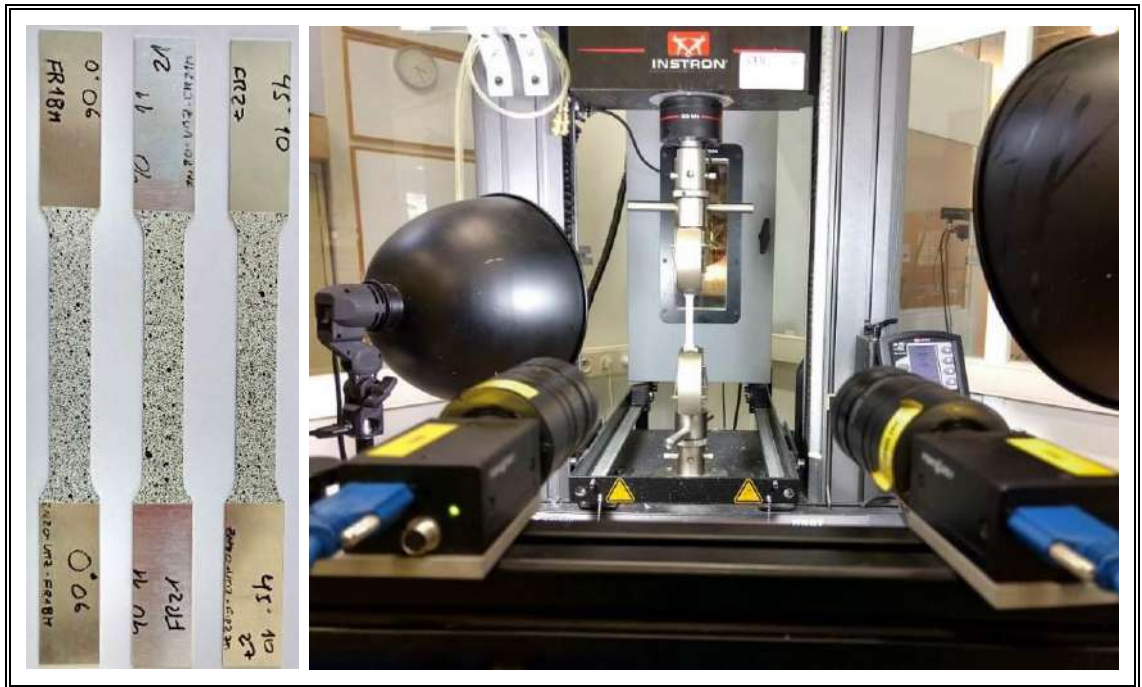


Figure 3-1: Tensile specimen. Right: Experimental setup.

The characteristic mechanical properties shown in Table 1 were determined from the uniaxial tensile tests. The samples were cut along different directions with respect to

the rolling one RD (0°) (i.e., 22.5°, 45° or diagonal direction DD, 67.5°, and 90° or transversal direction TD). The properties shown are Yield Strength (σ_{yp}), the Ultimate Tensile Strength (UTS) in the Engineering Stress-Strain Curve, the strain at the UTS, and the Mean Lankford (R) value. The reference system considers RD and TD aligned with the x and y axes in the material reference system. Thus, the z -axis defines the out-of-plane direction.

All reported values were obtained applying standard procedures, i.e., the yield stress σ_{yp} was obtained with the 0.002 strain offset while the mean Lankford coefficients were computed from the DIC images over the gauge area during the time interval for which a homogeneous strain pattern is observed (see 3.3.1). The studied alloy shows no major differences between the five sample directions and the experimentally determined elasticity modulus (E). A value of 99.0 GPa was considered for all directions based on Ledbetter (Ledbetter, 1977). The Poisson's ratio was assumed as 0.23 (Tromans, 2011). These tests are considered in this work as the basis to obtain the calibration data of the constitutive model presented in Section 2.3.

Table III-1: Mechanical properties of the Zn20 alloy.

Direction	Sample N°	σ_{yp} (MPa)	UTS (MPa)	Strain at UTS (%)	Mean <i>R</i> value
RD	1	107.5	138.5	15.8	0.25
	2	109.5	140.6	13.4	0.24
22.5°	1	108.7	142.7	11.9	0.24
	2	107.4	143.8	12.3	0.24
DD	1	122.9	160.9	11.5	0.32
	2	128.0	161.8	9.6	0.32

Direction	Sample N°	σ_{yp} (MPa)	UTS (MPa)	Strain at UTS (%)	Mean <i>R</i> value
67.5°	1	145.6	182.5	8.9	0.53
	2	144.6	198.1	7.7	0.52
TD	1	150.7	196.9	7.9	0.72
	2	162.4	196.6	7.7	0.72

b) Compression Test

The compression test was carried out with a device designed from the Kuwabara-type rig (Maeda et al., 2017) mounted on an Instron 3382A universal testing machine. The device has two pairs of comb-shaped dies with relative movement between them in the axial direction. The compression specimen, manufactured according to the ASTM E-8 standard with a width of 40 mm and a length of 50 mm, is mounted between polypropylene sheets to minimize friction effects within the device. However, according to Kuwabara et al. (Kuwabara et al., 2009), friction has no noticeable effect on the experimental results on this type of device.

To avoid buckling of the sample, the maximum strain was limited to 0.01 to avoid buckling of the sample. As in the tensile test, the yield point calculation was performed at 0.002 of true strain. The tests were conducted at room temperature and a strain rate of 0.00067 s⁻¹; only TD samples were used. Figure 3-2 shows the samples, experimental setup, and DIC capture for the vertical displacement field.

Strains field were evaluated using the DIC technique with a single camera Nikon D3300 with a Micro-Nikkor 85mm f / 3.5G lens, Ncorr v1.2 open-source software (Blaber et al., 2015) was used for data post-processing. The parameters of this analysis were the radius of the analysis circle (subset): 20 pixels; spacing between

subsets: 1 pixel; strain radius was adjusted to 20 pixels. The results are used to verify the presence of SD-Effect.

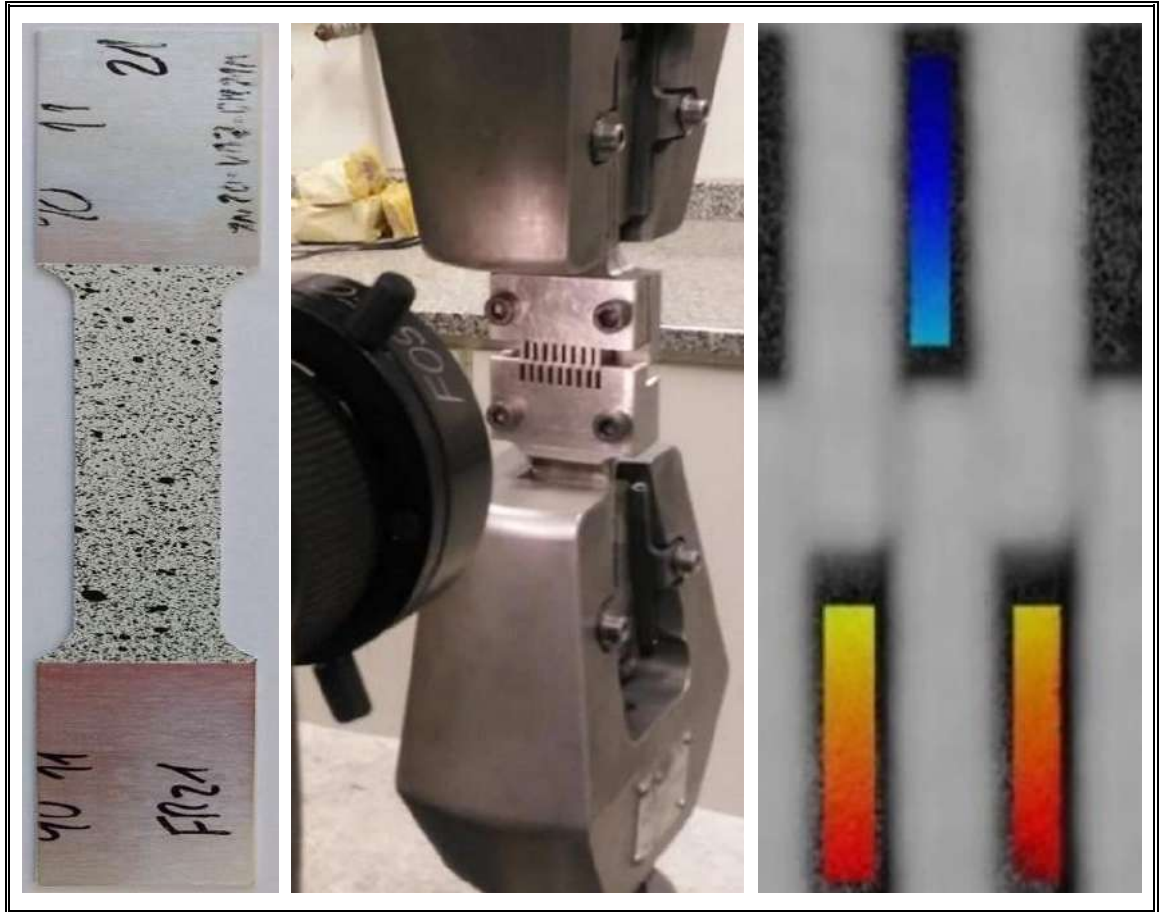


Figure 3-2: Left: Compression specimen. Center: Experimental setup. Right: DIC over the test.

c) Simple Shear Test

The simple shear test is used to validate, experimentally, the material mechanical response for strain paths that were not considered in the model calibration. The sample has two symmetrical rectangular shear areas concerning the load application axis of 3 mm width and 70 mm length, fixed in a device designed for this purpose based on the Miyauchi setup (An et al., 2009; Miyauchi, 1984; Yin et al., 2014;

Zillmann et al., 2012). A detailed view of the sample and the rig are shown in Figure 3-3.

The sample device set is mounted in an Instron 3382 universal testing machine. Tests were carried out at room temperature, applying a constant engineering strain rate of 0.0005 s^{-1} . The load data was taken directly from the machine load cell, while the displacement and strain were obtained using the same DIC setup used for the compression test (subset 13 pixels; spacing 3 pixels and strain radius 15 pixels).

Mechanical tests were conducted up to 0.2 of in-plane shear strain with one sample per direction RD, DD, and TD. The load-displacement curves are used as validation of the constitutive model presented in Section 3.2.3.

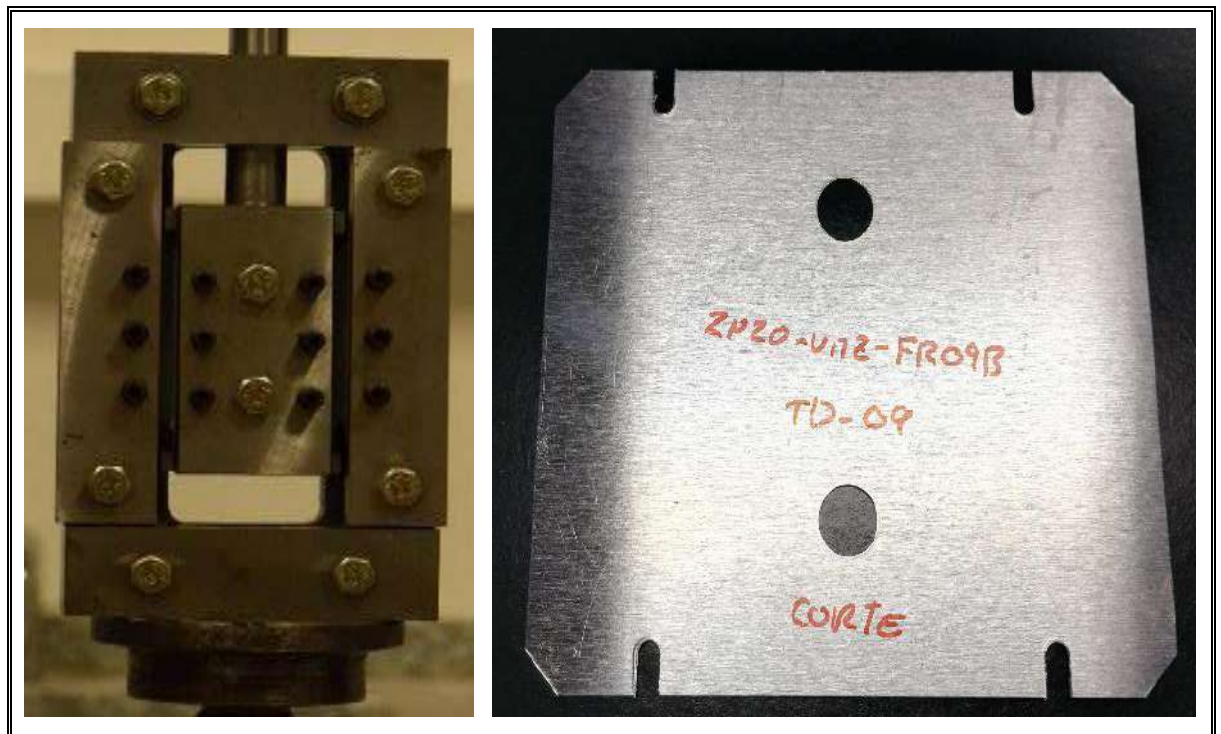


Figure 3-3: Left: Experimental Rig. Right: Shear specimen.

d) Bulge Test

The bulge test can extend the strain limits beyond the uniaxial tensile test. Moreover, the bulge test provides information for the right side of FLD diagrams without the inconvenience of the contact and friction between the punch and the sample as in other tests (e.g., Nakazima).

The bulge test is used in this work as a validation experiment. Three masks with different minor to major axis ratios (β) were used, with a major axis of 120 mm length. The chosen ratios were $\beta=1$ for equibiaxial conditions, $\beta=0.66$ and $\beta=0.33$.

The test specimen is a hexagonal cut of the sheet with a circumscribed diameter of 160 mm. For each direction RD, DD or TD, the material axis was aligned with the mask's major axis. The mean strain rate for all tests until fracture was 0.002 s⁻¹. Two repetitions per direction (RD, DD, and TD) and mask ($\beta=1$, 0.66, and 0.33) were performed until fracture.

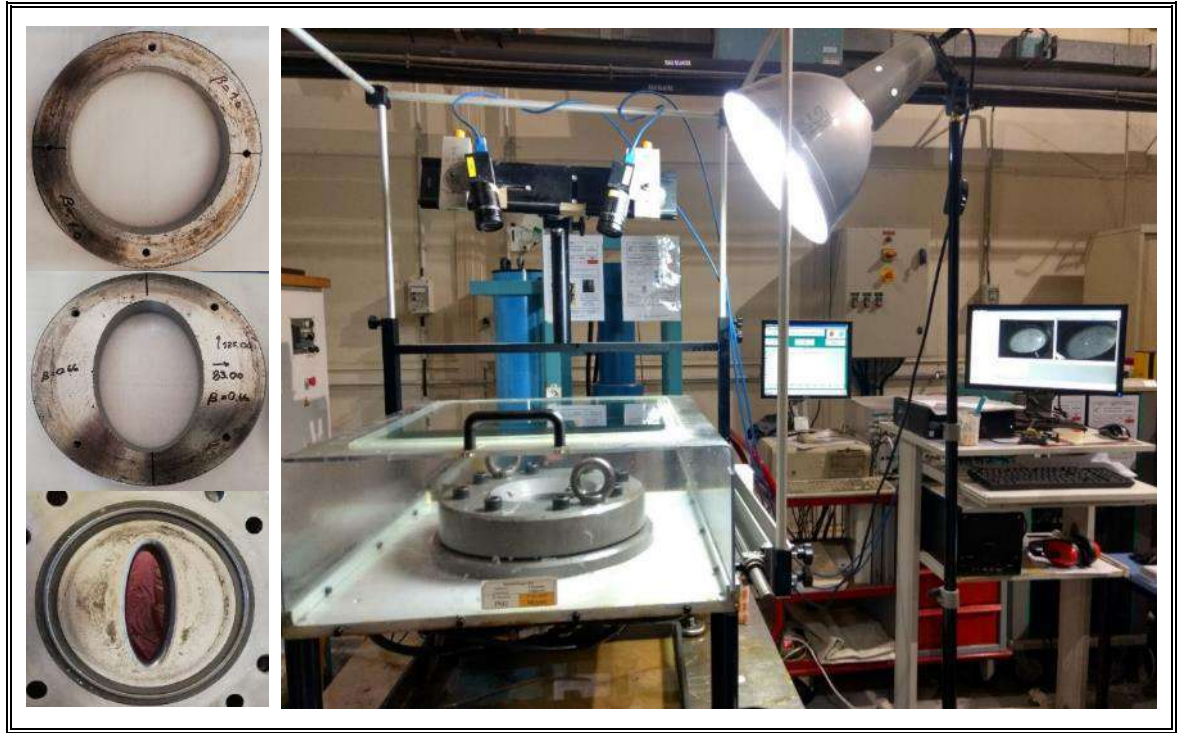


Figure 3-4: Left: Masks used in the bulge test, from top to bottom $\beta=1.00$, $\beta=0.66$, and $\beta=0.33$. Right: Experimental setup.

For each test, strain evolution was registered from a circle of 5 mm diameter placed on the top of the dome. The same DIC hardware and software previously used in the tensile tests were used for this test with a grid and step size of 19 and 4 pixels, respectively. Here, the pressure data was recorded every second and synchronized with the DIC information. The masks used, the experimental setup, and a DIC capture are presented in Figure 3-4.

e) Samples Geometries

The sample dimension for tensile, compression, and shear experiments are presented in Figure 3-5.

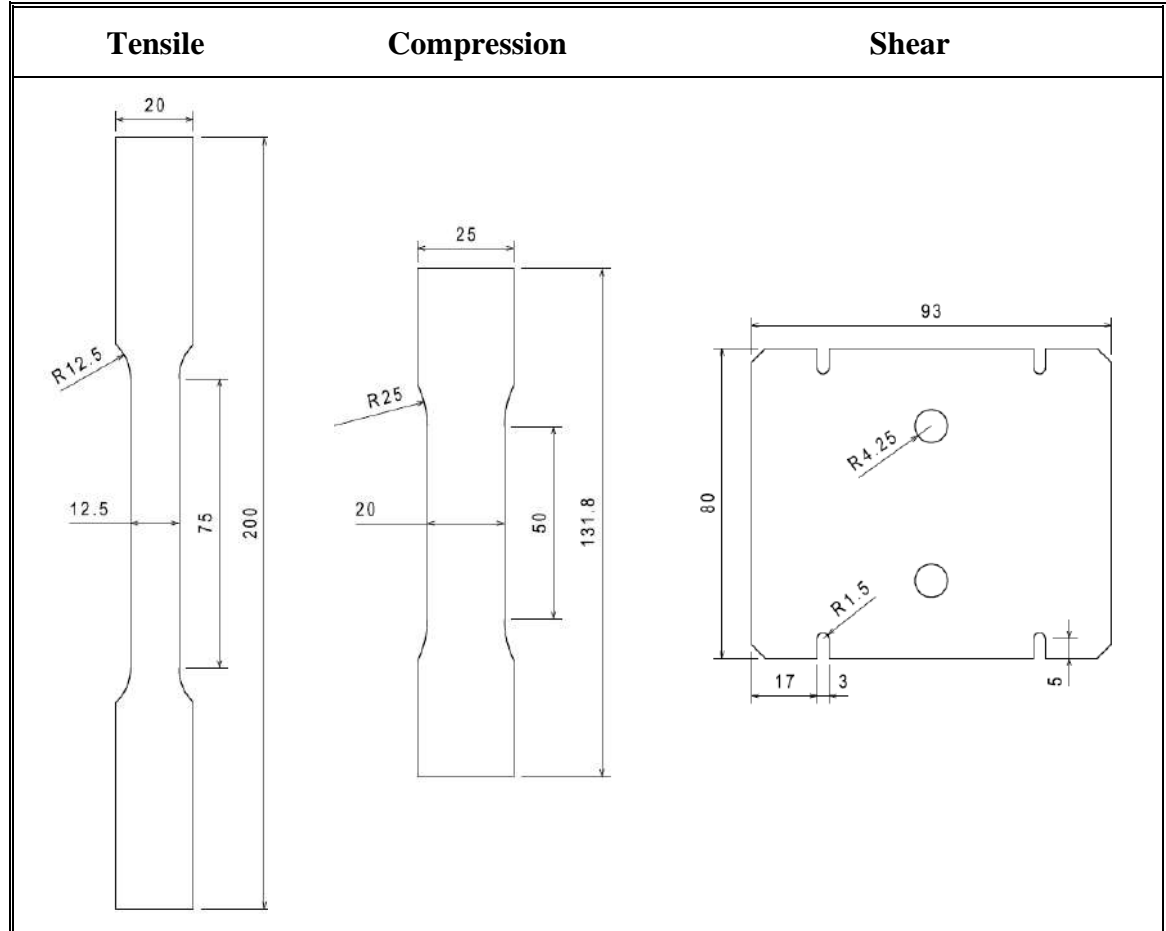


Figure 3-5: Schematic representation with dimensions for tensile, compression, and shear specimens (all samples in the same scale, dimensions in millimeters).

3.2.3 Constitutive model

The constitutive model adopted in this work was already reported in (Alister et al., 2019; Cazacu et al., 2006; Plunkett et al., 2006, 2008). Therefore, it is summarized in what follows only for completeness of the present study. The model considers an associated flow rule and rate-independent plasticity assuming the standard elastoplastic strain decomposition. The constitutive model has been implemented in

an in-house finite element code with a radial-return scheme based on the Newton-Raphson iterative method (Celentano et al., 2012).

a) Yield Function

The CPB-06 yield criterion chosen to describe the material behavior is written as (Cazacu et al., 2006; Plunkett et al., 2006, 2008):

$$F_{(\boldsymbol{\sigma}, \bar{\varepsilon}_p)} = \bar{\sigma}(\boldsymbol{\sigma}) - Y(\bar{\varepsilon}_p) = 0 \quad (3.1)$$

where $\bar{\sigma}$ is the equivalent stress, $\boldsymbol{\sigma}$ is the Cauchy stress tensor, Y is the isotropic hardening stress, and $\bar{\varepsilon}_p$ is the equivalent plastic strain. The equivalent stress is given by:

$$\bar{\sigma}(\boldsymbol{\sigma}) = \left(\frac{f(\boldsymbol{\Sigma})}{f(\boldsymbol{\gamma})} \right)^{\frac{1}{a}} \quad (3.2)$$

such that $f_{(\chi)}$, for $\chi = \boldsymbol{\Sigma}$ or $\chi = \boldsymbol{\gamma}$, is defined as:

$$f = (|\chi_1| - k\chi_1)^a + (|\chi_2| - k\chi_2)^a + (|\chi_3| - k\chi_3)^a \quad (3.3)$$

where a is the degree of homogeneity, Σ_i are the principal components of the transformed stress tensor, γ_i are the modified anisotropic coefficients, and k is the asymmetry parameter (related to the Strength Differential effect or SD-effect). The reported expression for the transformed stress tensor $\boldsymbol{\Sigma}$ is given by:

$$\begin{pmatrix} \Sigma_{xx} \\ \Sigma_{yy} \\ \Sigma_{xy} \\ \Sigma_{zz} \\ \Sigma_{xz} \\ \Sigma_{yz} \end{pmatrix} = \begin{pmatrix} L_{11} & L_{12} & 0 & L_{14} & 0 & 0 \\ L_{12} & L_{22} & 0 & L_{24} & 0 & 0 \\ 0 & 0 & L_{33} & 0 & 0 & 0 \\ L_{14} & L_{24} & 0 & L_{44} & 0 & 0 \\ 0 & 0 & 0 & 0 & L_{55} & 0 \\ 0 & 0 & 0 & 0 & 0 & L_{66} \end{pmatrix} \begin{pmatrix} \sigma'_{xx} \\ \sigma'_{yy} \\ \sigma'_{xy} \\ \sigma'_{zz} \\ \sigma'_{xz} \\ \sigma'_{yz} \end{pmatrix} \quad (3.4)$$

[m]

where the components of tensor \mathbf{L} are the anisotropic coefficients and $\boldsymbol{\sigma}'_{[m]}$ is the deviatoric part of the Cauchy stress tensor expressed in the material reference system $[m]$. For a plane stress case, the following transformation is applied:

$$\sigma_{xx[m]} = \sigma_{xx[r]} \cos^2 \theta + \sigma_{yy[r]} \sin^2 \theta + 2 \sin \theta \cos \theta \sigma_{xy[r]} \quad (3.5)$$

$$\sigma_{yy[m]} = \sigma_{xx[r]} \sin^2 \theta + \sigma_{yy[r]} \cos^2 \theta - 2 \sin \theta \cos \theta \sigma_{xy[r]} \quad (3.6)$$

$$\sigma_{xy[m]} = (\sigma_{yy[r]} - \sigma_{xx[r]}) \sin \theta \cos \theta + \sigma_{xy[r]} (\cos^2 \theta - \sin^2 \theta) \quad (3.7)$$

where the subscript r denotes the tensile test reference system such that the sample is loaded in the x -direction.

The modified anisotropic coefficients γ_i are:

$$\gamma_1 = \left(\frac{2}{3} L_{11} - \frac{1}{3} L_{12} - \frac{1}{3} L_{14} \right) \quad (3.8)$$

$$\gamma_2 = \left(\frac{2}{3} L_{12} - \frac{1}{3} L_{22} - \frac{1}{3} L_{24} \right) \quad (3.9)$$

$$\gamma_3 = \left(\frac{2}{3} L_{14} - \frac{1}{3} L_{24} - \frac{1}{3} L_{44} \right) \quad (3.10)$$

For an isotropic material, the asymmetry coefficient k is obtained as:

$$k = 1 - \frac{\left\{ \frac{2^a - 2 \left(\frac{\sigma_t}{\sigma_c} \right)^a}{\left(\left(\frac{\sigma_t}{\sigma_c} \right)^a - 2 \right)} \right\}^{\frac{1}{a}}}{1 + \left\{ \frac{2^a - 2 \left(\frac{\sigma_t}{\sigma_c} \right)^a}{\left(\left(\frac{\sigma_t}{\sigma_c} \right)^a - 2 \right)} \right\}^{\frac{1}{a}}} \quad (3.11)$$

where $\frac{\sigma_t}{\sigma_c}$ is the ratio between the yield values at tension and compression respectively obtained from the uniaxial tensile and compression tests over the same direction. It

should be noted that this expression is valid regardless of the sample direction (Cazacu et al., 2006; Plunkett et al., 2008, 2006). Finally, if the material shows no asymmetry or SD-effect, k is equal to 0. In this work, it is assumed that the yield function presents no coupling between anisotropy and asymmetry.

b) Hardening Function

The hardening behavior is represented by the Swift power law (Swift, 1952) written for RD as:

$$Y_{(\bar{\varepsilon}_p)} = K(\bar{\varepsilon}_0 + \bar{\varepsilon}_p)^n \quad (3.12)$$

where K is the strength coefficient, $\bar{\varepsilon}_0 = \left(\frac{\sigma_{yp}^{RD}}{K}\right)^{\frac{1}{n}}$ and n is the hardening exponent. σ_{yp}^{RD} is the yield strength for RD (see Table III-1). The rate of the equivalent plastic strain is $\dot{\bar{\varepsilon}}_p = \frac{\boldsymbol{\sigma}_m : \dot{\boldsymbol{\varepsilon}}_p}{\bar{\sigma}}$, such that $\boldsymbol{\varepsilon}_p$ is the plastic strain tensor with the associated flow rule $\dot{\boldsymbol{\varepsilon}}_p = \dot{\lambda} \frac{\partial \bar{\sigma}}{\partial \boldsymbol{\sigma}_m}$, where $\dot{\lambda}$ is the plastic consistency parameter. Finally, $\boldsymbol{\sigma}_m$ is the Cauchy stress tensor based on the material reference system (according to the transformation on (3.5) to (3.7)) and $\bar{\sigma}$ is the equivalent stress. The hardening function can be explicitly written as:

$$Y_{(\bar{\varepsilon}_p)} = K \left[\left(\frac{\sigma_{yp}^{RD}}{K} \right)^{\frac{1}{n}} + \bar{\varepsilon}_p \right]^n \quad (3.13)$$

3.2.4 Model Calibration Procedure

The material parameters of the constitutive model presented in Section 3.2.3 are obtained through a fitting procedure that only considers the tensile and compression test results. Both the hardening and CPB-06 coefficients (except the asymmetry parameter k) are obtained using the fitting methodology developed by Alister (Alister et al., 2019), which is based on the procedure described and used in other works (Barros et al., 2016; Dasappa et al., 2012; Gilles et al., 2012). This methodology minimizes the error between the experimental and corresponding analytical values of the tensile true stress-strain curves and means Lankford coefficients for the five sample directions reported in Section 3.2.1. The results of the compression test are exclusively used to determine the value of the asymmetry parameter k .

The minimization function used in (Alister et al., 2019) is described in (3.14). Also, the terms $\sigma_{\theta^\circ}^{num}$ and $R_{\theta^\circ}^{num}$ are presented for clearness in equations (3.15) and (3.16):

$$Error_L = \sum_{\theta^\circ=22.5^\circ}^{90^\circ} W_{\theta^\circ}^T \sum_{i=1}^m \left(\frac{\sigma_{\theta^\circ}^{num}}{\sigma_{\theta^\circ}^{exp}} - 1 \right)_i^2 + \sum_{\theta^\circ=0^\circ}^{90^\circ} W_{\theta^\circ}^R \sum_{i=1}^m \left(\frac{R_{\theta^\circ}^{num}}{R_{\theta^\circ}^{exp}} - 1 \right)_i^2 \quad (3.14)$$

$$\sigma_{\theta^\circ}^{num} = Y_{(\bar{\varepsilon}_p)} \left(\frac{f(Y)}{f(\varphi)} \right)^{\frac{1}{a}} \quad (3.15)$$

$$R_{\theta^\circ}^{num} = - \frac{\frac{\partial \bar{\sigma}}{\partial \sigma_{yy}[r]}}{\frac{\partial \bar{\sigma}}{\partial \sigma_{xx}[r]} + \frac{\partial \bar{\sigma}}{\partial \sigma_{yy}[r]}} \quad (3.16)$$

In the present study, L_{11} , L_{55} , L_{66} , and weights W_{θ° were set to 1 (Cazacu et al., 2006, 2010; Chandola et al., 2015; Muhammad et al., 2015; Revil-Baudard et al., 2014;

Tuninetti et al., 2012, 2015; Yoon et al., 2013). By its side, “ m ” represents the number of fitting points per each direction and repetition, from the yield point to the OS-Necking. A fitting point is considered as a pair of $\bar{\epsilon}_p - \sigma$ or $\bar{\epsilon}_p - R$. Because of this, each direction and term (stress or R value) has its specific number of fitting points.

Finally, the fitting procedure's performance is assessed through the Root Mean Square Error (RMSE) between the experimental and corresponding analytical values for both the tensile stress curves and mean Lankford coefficients considering once again the five sample directions described in Section 3.2.1 with the use of the following expressions:

$$E_{\sigma} = \sqrt{\frac{1}{m} \sum_{i=1}^m (\sigma_{\theta^{\circ}}^{num} - \sigma_{\theta^{\circ}}^{exp})^2} \quad (3.17)$$

$$E_R = \sqrt{\frac{1}{m} \sum_{i=1}^m (R_{\theta^{\circ}}^{num} - R_{\theta^{\circ}}^{exp})^2} \quad (3.18)$$

3.2.5 Numerical Simulation of the Shear and Bulge Tests

The simulations were carried out in an - in-house - Finite Element code where the CPB-06 yield function was implemented according to Section 3.2.3. The samples of these experiments were discretized with the finite element meshes shows in Figure 6. These meshes were structured with trilinear hexahedra with 8 integration points and a B-bar technique to avoid locking due to the plastic incompressibility constraint (Celentano et al., 2012). The total number of elements for the shear and bulge meshes were 7,440 and 15,600, respectively, with 4 elements in thickness for both

simulations. For the shear test, the geometry is symmetric with respect to the thickness plane, and only the gauge area was modeled.

On the other hand, the bulge test was modeled with no symmetries. Only the geometry of the masks was modified for the different configurations. Neither the sample nor the mask elements (number or type) change. The masks are assumed to be rigid. The contact between sample and mask is represented by the Coulomb model with a friction coefficient of 0.12 to improve interaction conditions in the contact zone.

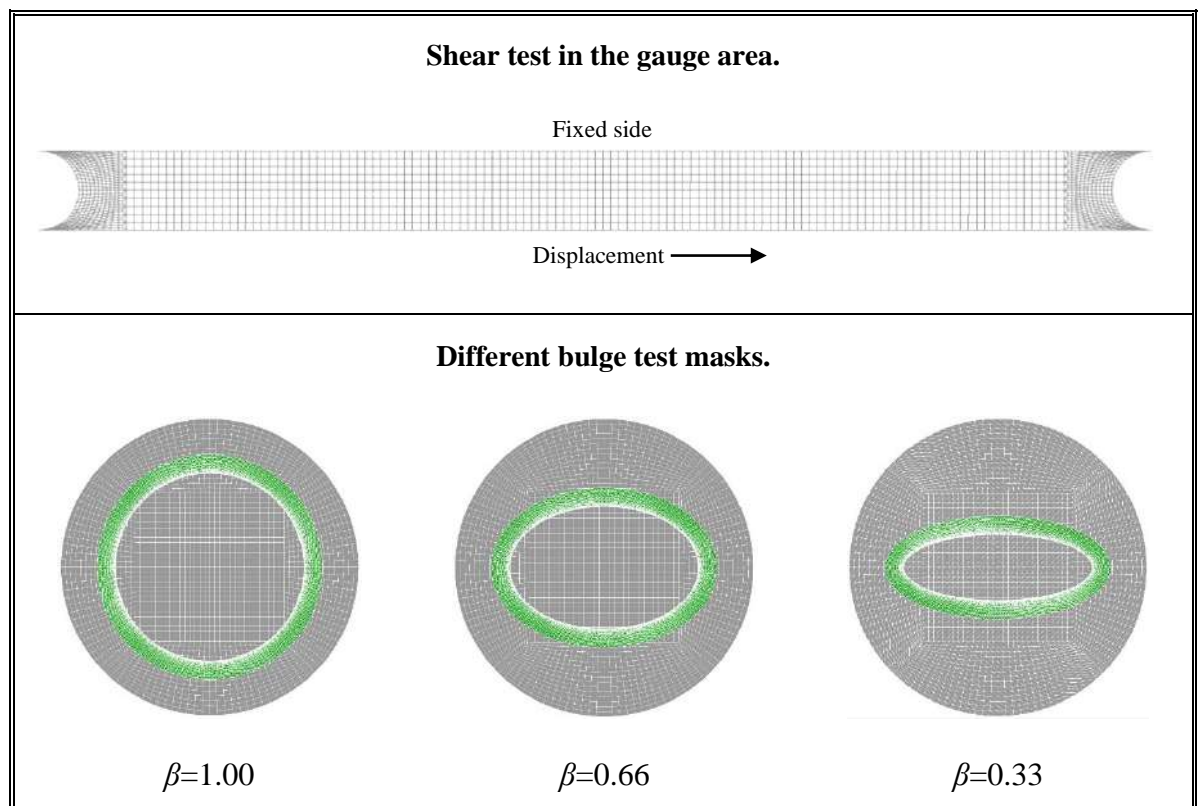


Figure 3-6: Meshes and boundary conditions used in the finite element models.

For the bulge tests, the sheet sample is grey, and the mask is green.

The shear test's boundary conditions are an imposed displacement on one side of the gauge area, and a total restraint on the opposite was used. The displacement is progressively applied linearly from 0 to the maximum experimental recorded displacement. For the bulge test, hydrostatic pressure from 0 to 5 MPa (step 0 to final step) is prescribed on the sample's inner side.

3.3 Results

3.3.1 Homogeneous State Range in the Tensile Test

Leonard et al. (Leonard et al., 2019) reported that zinc alloys exhibit a weak trend to necking formation during the tensile test. Localization bands are formed over all the samples during the test. The necking formation is not clear until a few steps before fracture. Therefore, nearly homogeneous stress and strain patterns are obtained well beyond the UTS. This homogenous state is confirmed in what follows for the material considered in the present work.

Figure 3-7 shows the true strain (Hencky) profile over the sample's main axis for three strain levels: yield point, UTS, and the onset of necking formation (OS-Necking) in the reference configuration (not deformed). The sample position is set so that the 0 position coincides with the center of the extensometric length. Thus, to the right of the "Sample position" axis, the analyzed point moves to the top and vice-versa.

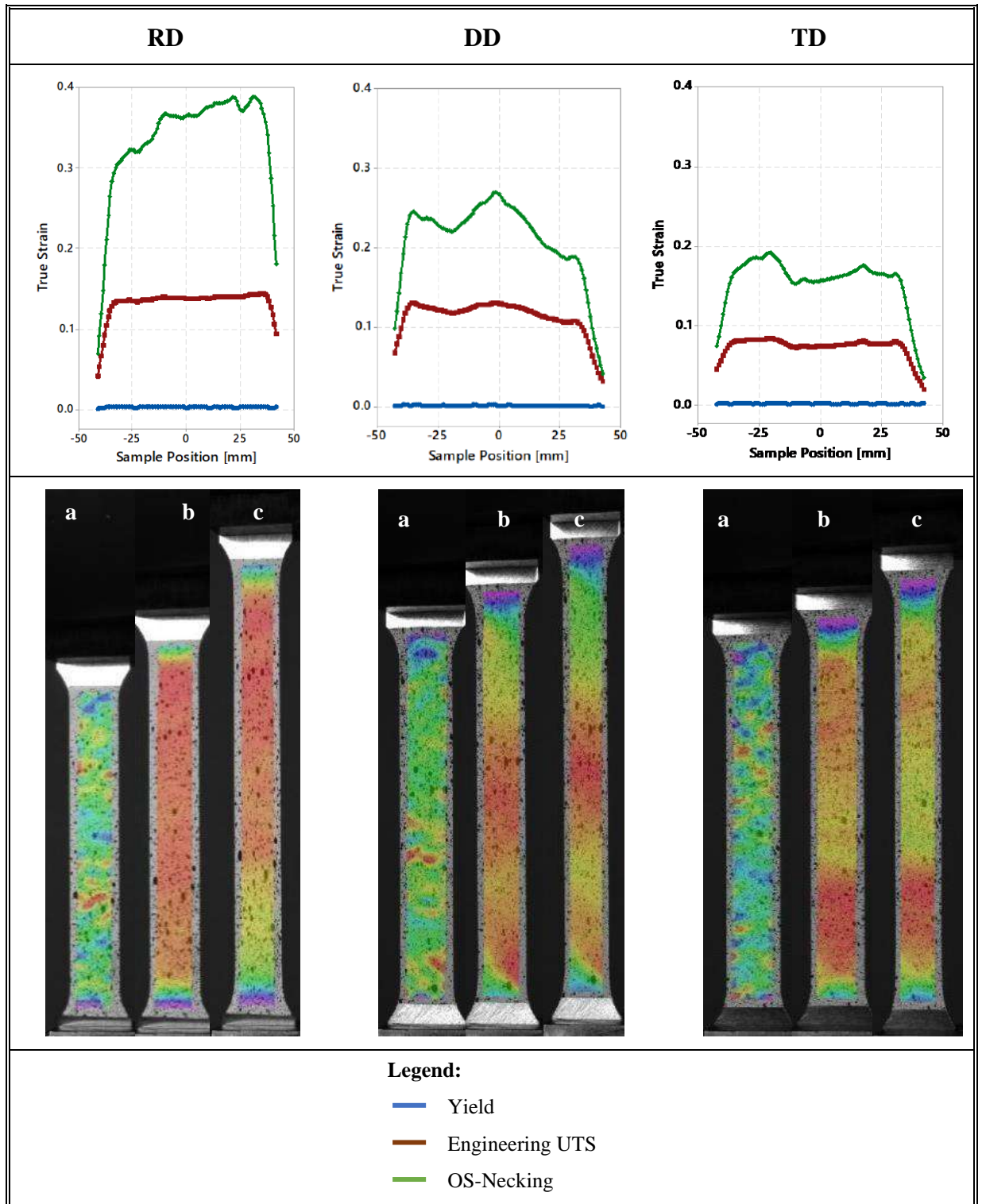


Figure 3-7: Strain distribution over the sample length for RD, DD, and TD. The DIC images correspond to a) yield point, b) UTS, and c) OS-Necking.

As can be seen for RD, DD, and TD, the homogeneous strain area covers a length of 60 mm for the UTS point. Although this strain level is relatively low (e.g., less than 0.15), it should be noted that no necking starts to develop at this stage. Instead, the OS-Necking occurs afterward, at a strain level where the strain distribution can still be considered approximately homogeneous, for which the variations in the strain value are less than 0.05 over a length of at least 20 mm for the three samples.

3.3.2 Fitted Material Model Parameters from the Tensile Test

The model parameters were fitted in the plastic strain interval ranging from the yield point (σ_{yp}) up to the OS-Necking. It is essential to highlight that the use of this range, instead of the shorter one delimited by σ_{yp} and UTS, allows improving the predictive capabilities of the constitutive model in the description of the material anisotropy and hardening behavior. The objective function value (equation (3.14)) was 2.27 for UTS and 1.68 for the OS-Necking.

The obtained Swift and CPB-06 fitted coefficients are respectively presented in Tables III-2 and III-3. In this work, the homogeneity degree a was defined as 4 after screen trials for this parameter (Alister et al., 2019). Besides, Liu et al. (Liu et al., 1997) show a better approximation with fourth-order yield models for some HCP materials. The CPB-06 coefficients were considered constant and valid for all the plastic strain range since, as shown below, there is no significant variation of the Lankford coefficient with the level of deformation.

Table III-2: Swift fitted coefficients.

<i>K</i> (MPa)	ϵ_0	<i>n</i>
196.8	0.0036	0.107

Table III-3: CPB-06 fitted coefficients.

<i>L</i>₁₂	<i>L</i>₁₄	<i>L</i>₂₂	<i>L</i>₂₄	<i>L</i>₃₃	<i>L</i>₄₄	<i>k</i>	<i>a</i>
0.0555	-0.1908	0.8529	0.0247	0.8555	1.0557	0.0	4.0

The analytical computed yield values and Lankford coefficients for three main directions are compared with the mean of the two repetitions per direction in Table III-4 and Table III-5. Additionally, the experimental mean values indicate the minimum and maximum deviation observed.

Table III-4: Experimental and Analytical Yield Values for main directions.

Parameter	RD	DD	TD
<i>σ</i> Exp.	108.5	+1.0	+2.6
		-1.0	-2.6
<i>σ</i> Ana.	107.5	125.6	150.8

Table III-5: Experimental and Analytical Lankford values for main directions.

Parameter	RD	DD	TD
<i>R</i> Exp.	0.251	+0.014	+0.0231
		-0.020	-0.0292
<i>R</i> Ana.	0.238	0.324	0.723

The obtained RMSEs for three main directions (and two repetitions per experiment), related to stress and Lankford values, are shown in Table III-6.

Table III-6: RMSE of the fitting procedure in the true stress-strain curves and Lankford coefficients for three main directions.

Parameter	RD		DD		TD	
	Exp. 1	Exp. 2	Exp. 1	Exp. 2	Exp. 1	Exp. 2
<i>Error_{σ}</i>	1.084	2.532	4.948	3.405	7.605	6.324
<i>Error_R</i>	0.013	0.007	0.011	0.013	0.010	0.008

The yield loci, based on CPB-06, for all five directions and von Mises in the $\sigma_1 - \sigma_2$ stress plane with the corresponding experimental yield values are shown in Figure 8. The yield loci were obtained with the transformation of equations (3-5) to (3-7) and the yield function definition in equations (3-2) and (3-3). The loci are rotated such σ_1 is coincident, for all directions, with the tensile test axis. The von Mises yield locus is plotted to contrast the high anisotropy of the studied alloy.

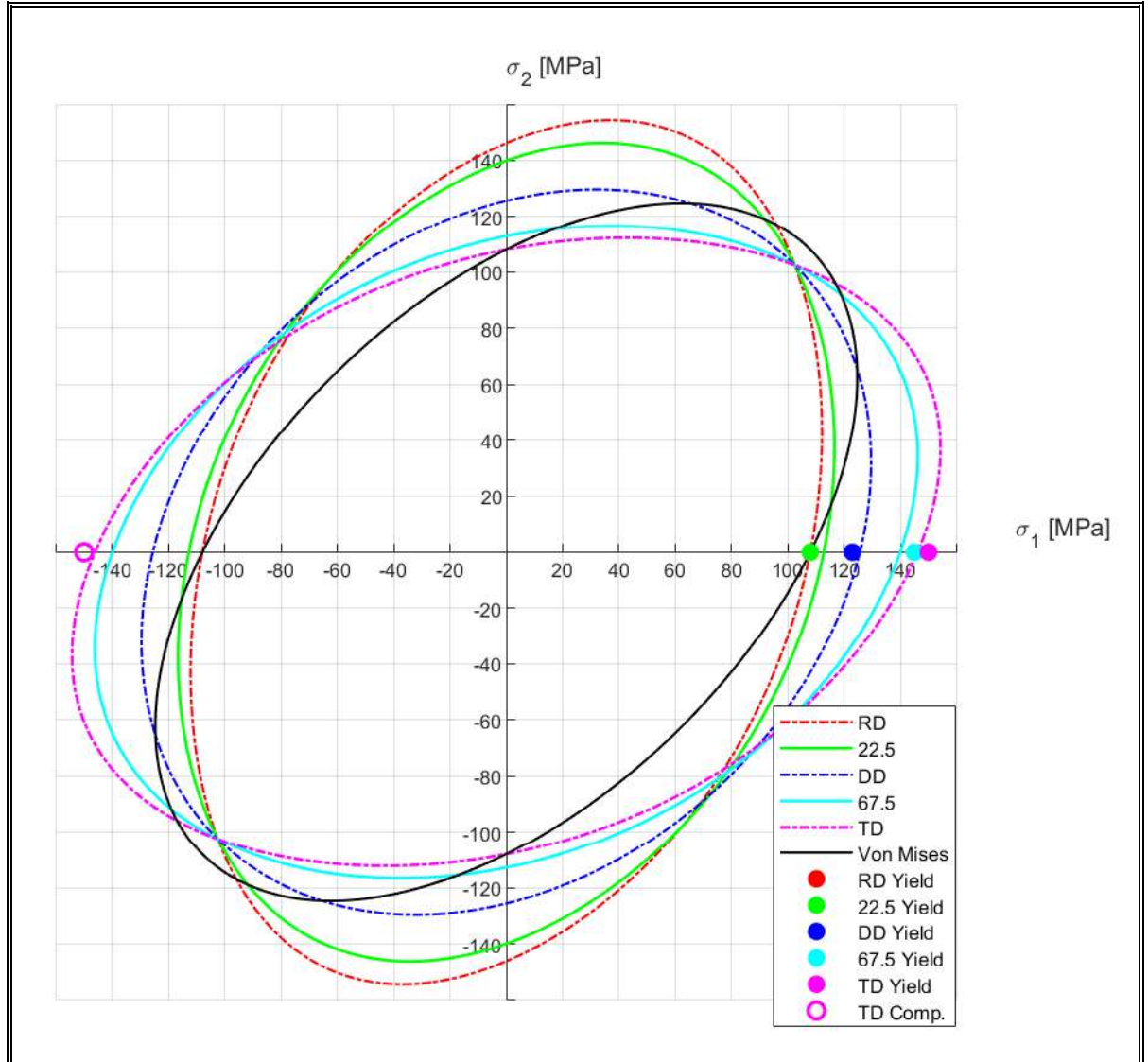


Figure 3-8: Yield loci for the $\sigma_1 - \sigma_2$ plane for all five directions based on the CPB-06 yield function. Experimental values at yield point with 0.002 strain offset for all tensile tests.

The adjusted true stress-strain curves, based on the CPB-06/Swift model, are presented in Figure 3-9.

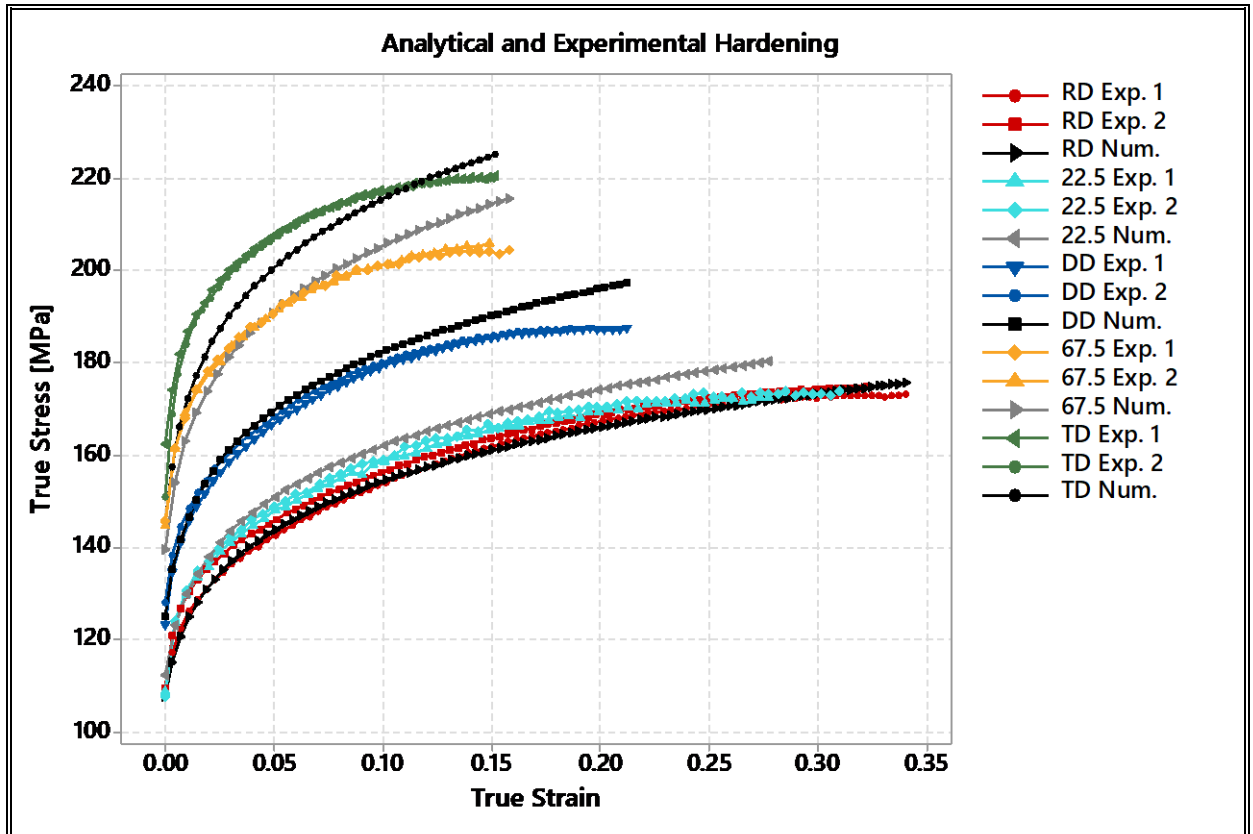


Figure 3-9: Experimental and analytical hardening curves for all five directions.

The analytical computed Lankford coefficients (see equation (16)) for all five directions are compared with the tow repetition's registered values in Figure 3-10.

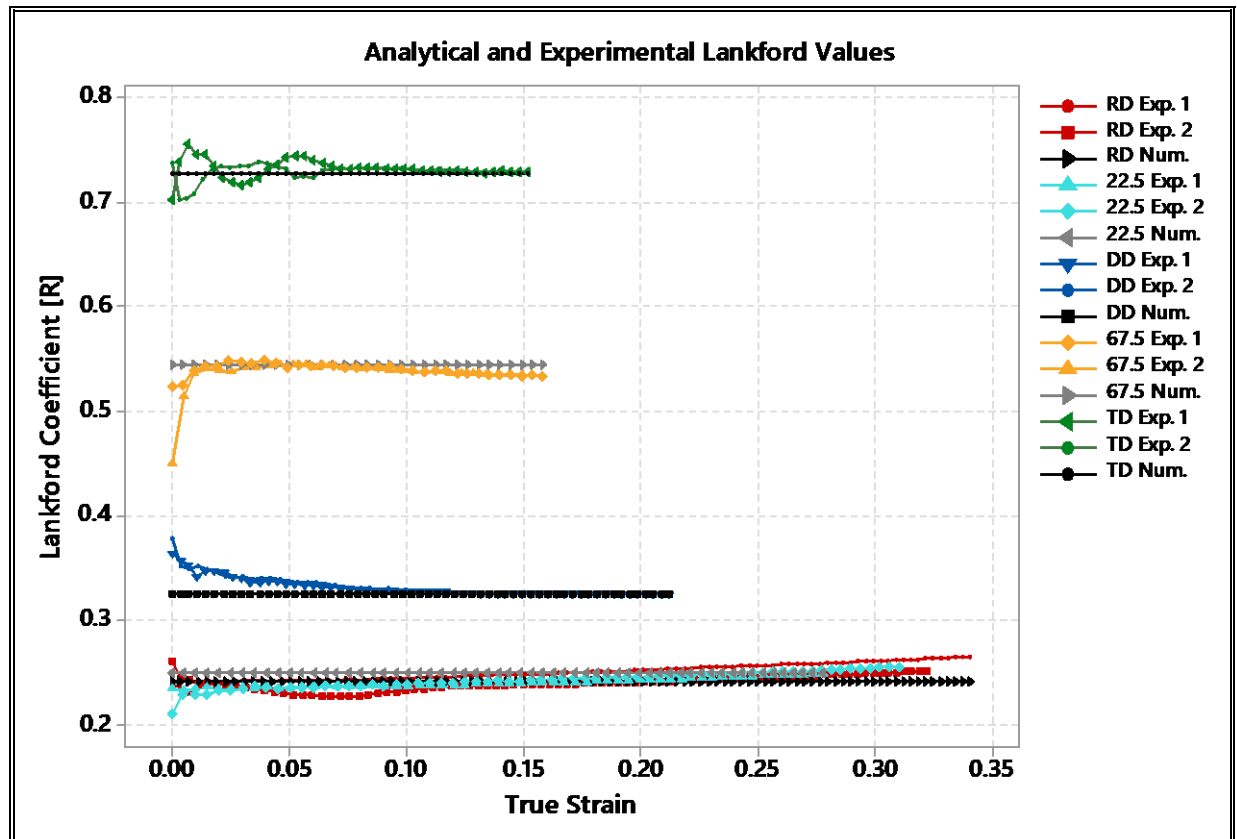


Figure 3-10: Experimental and analytical Lankford curves for all five directions.

The true stress-strain curve of the compression test shown in Figure 3-11 exhibits no significant differences from the tensile test at 0.002 of strain for TD. This behavior is assumed for RD and DD; however, further experiments need to be done in these directions. Therefore, no SD-effect is considered in this (TD) or the others directions, (i.e., RD, DD) assuming the isotropic definition for the k parameter. As a consequence, the value of k is set to 0.

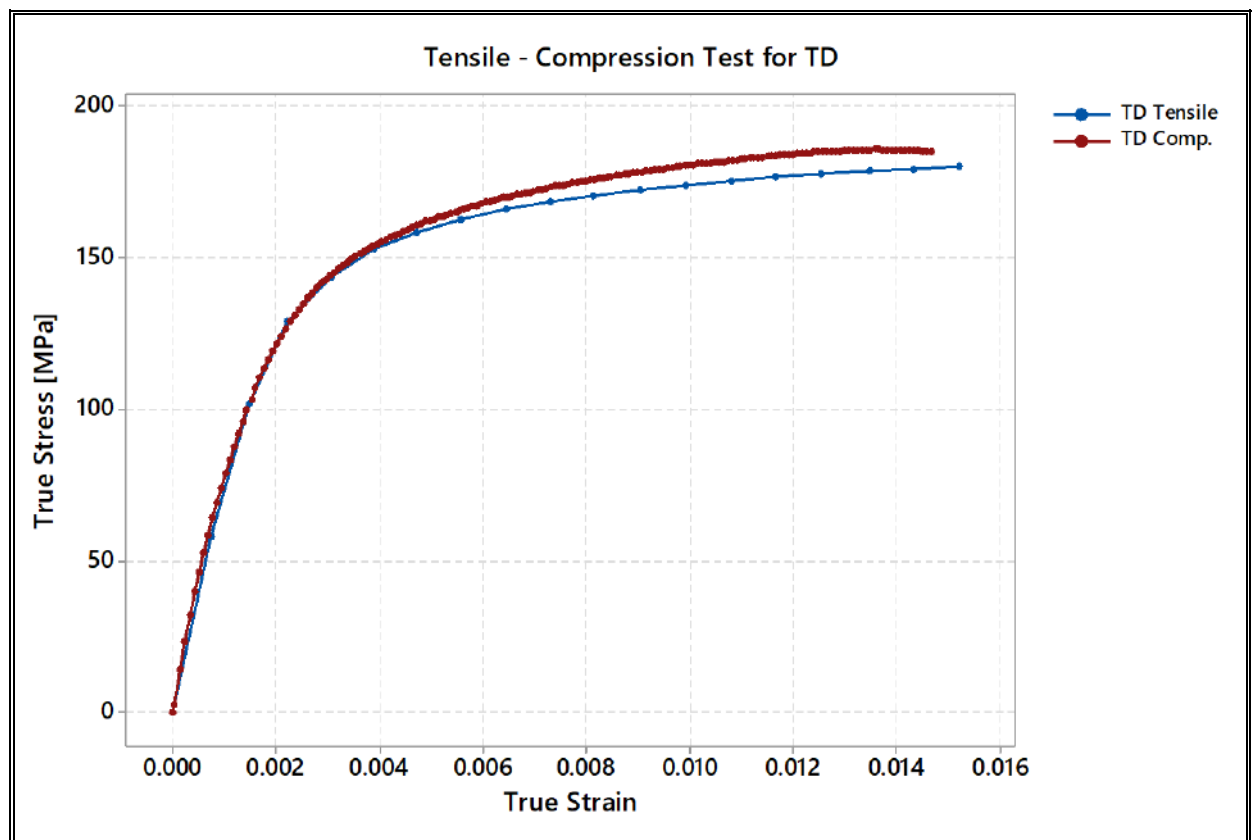


Figure 3-11: Experimental True Stress-Strain compression curves for TD.

3.3.3 Shear Test

The numerical Force–displacement curves are compared against the experimental curves for RD, DD, and TD in Figure 3-12. In addition, the DIC strain field together with the finite element computed strains are also shown.

The strain field plots are obtained for the same displacement at 1.0 mm. Inhomogeneous strain states can be seen in the gauge area's top and bottom border, on which the highest value was obtained. A homogeneous strain area with equivalent values of strain can be seen in both DIC and FEM simulations.

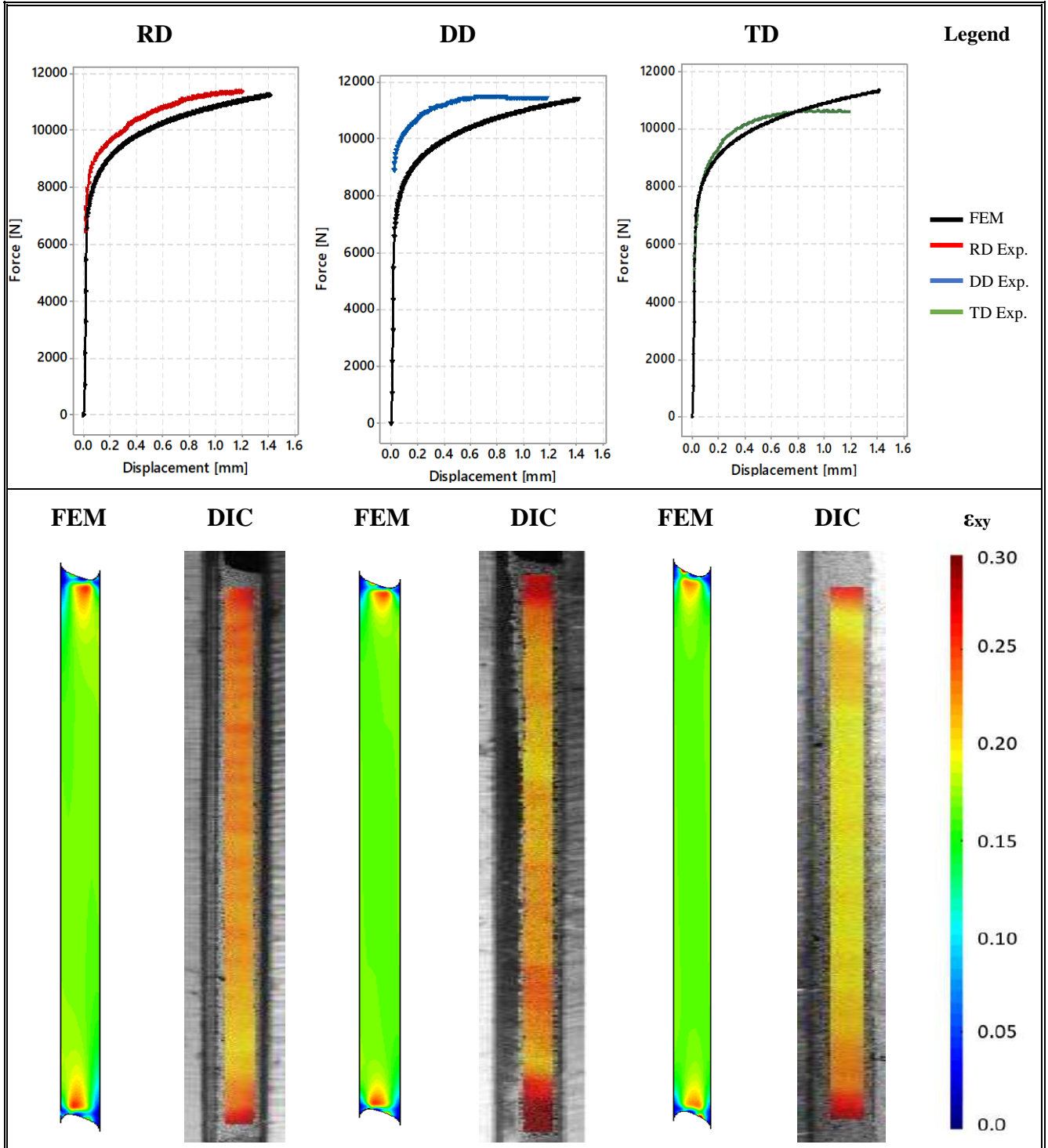


Figure 3-12: Shear test results. Top: Force - Displacement curves (Black solid line for numerical results). Bottom: In-plane shear strain plots (FEM simulations and DIC results).

3.3.4 Bulge Test

The naming of the bulge test experiments defines where the material axis is aligned with the elliptical mask's major axis. For example, $\beta=0.33$ | RD means a mask axis ratio of 0.33 with the RD aligned to the major axis.

The experimental and numerical strain paths on the major and minor strains diagram for the different dies and sample orientations are presented in Figure 3-13. Numerical and experimental values were gathered from the top dome element/area.

The plots include the two different experiments per mask and direction. The DIC image and FEM strain field presented in Figures 3-13 and 3-14 are obtained from the last step of the experiment and simulation.

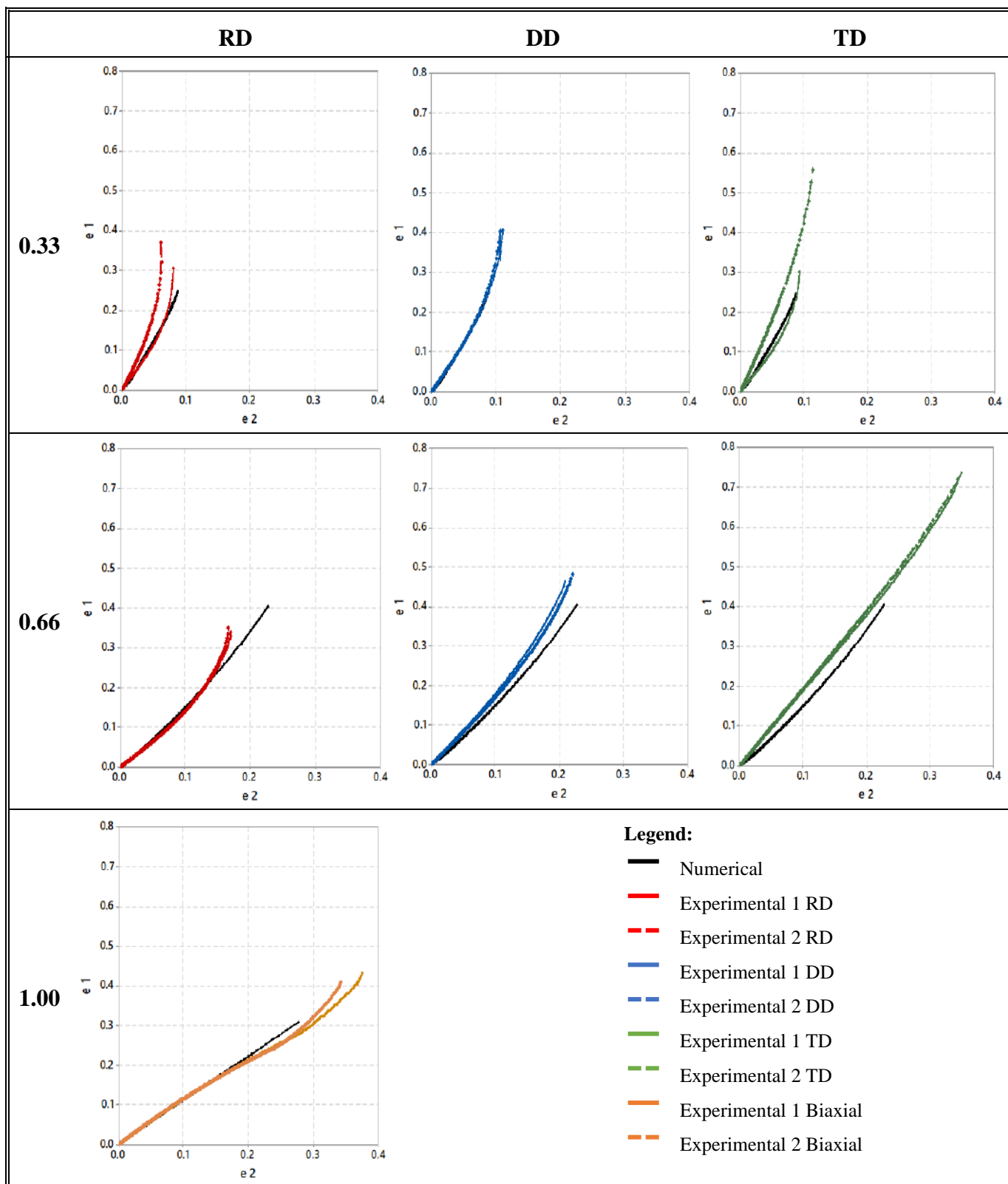
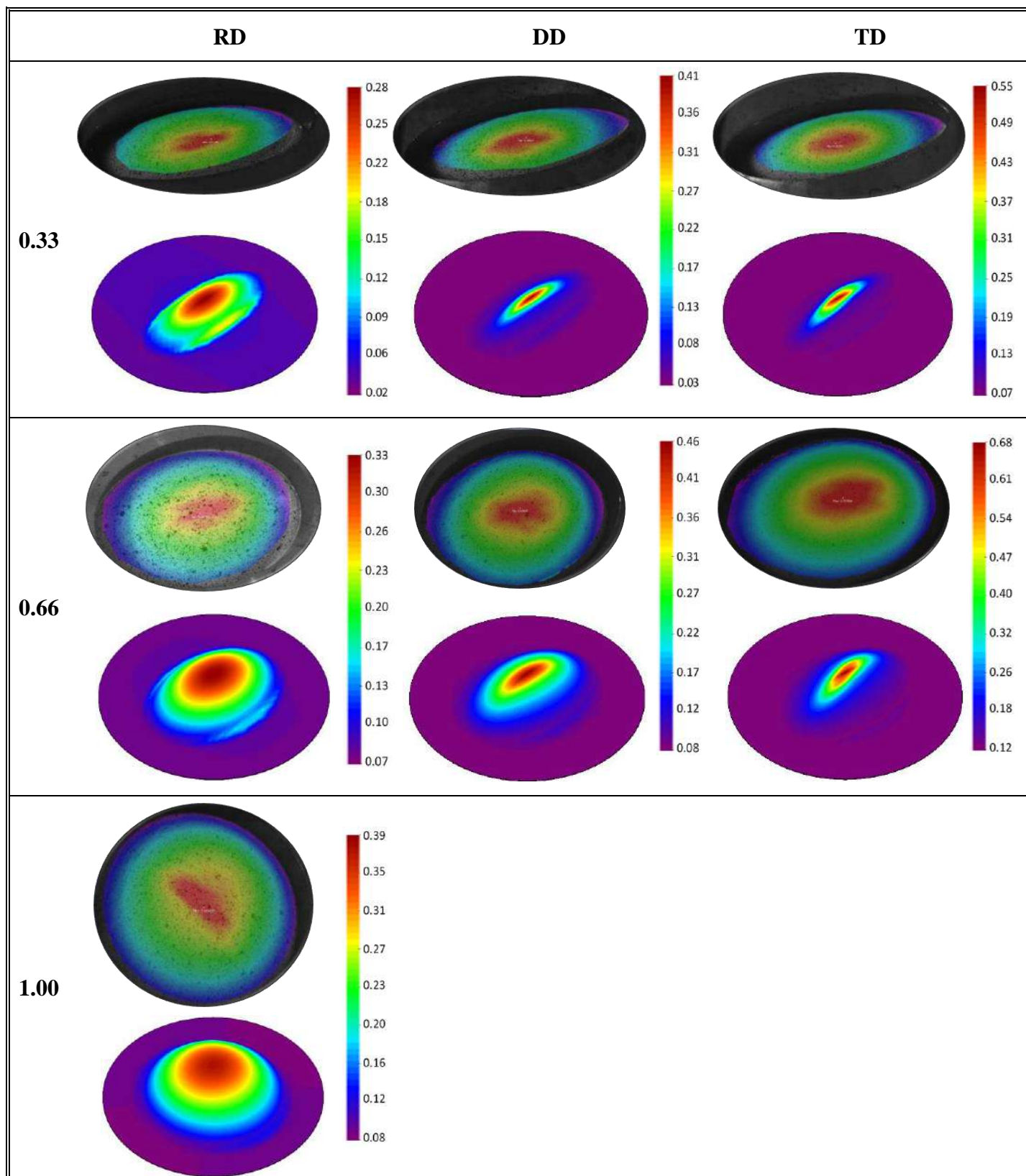


Figure 3-13: Numerical and experimental strain-strain plots for all conditions.

Here, in Figure 3-13, the numerically calculated strain paths are close to those obtained experimentally. Except for $\beta=0.66$, the experimental e_{11} strain values are always higher than the FEM model in the same e_{22} values, which reduces dome thickness earlier in the simulation. The DIC data and FEM model show the mask's dominance over the anisotropy, which means the strain path is equivalent for different directions with the same mask.

Figure 3-14 shows the major strain field (e_1) for the last step of the experiments and simulations. The images were taken from the frame before the mask's fracture in the experiments and at the end of the simulation in the FEM model. In addition, Figure 3-14 shows a qualitative and quantitative description of the strain fields.

Figure 3-14: DIC and FEM major strain field (ϵ_1) for all masks and directions.

The experimental dome thickness evolution is calculated based on the nominal sheet thickness at the dome and the ϵ_{zz} strain component assuming plastic incompressibility. In the FEM simulation, the dome thickness was determined with the nodal coordinates of the top and bottom elements. To compare the thickness reduction in the simulations and experiment, this measure is compared over the dome height evolution. Except for $\beta=0.33$ RD, the thickness reduction is faster in the simulation for all masks and directions. Figure 3-15 shows the experimental and numerically estimated thickness reduction against the dome height.

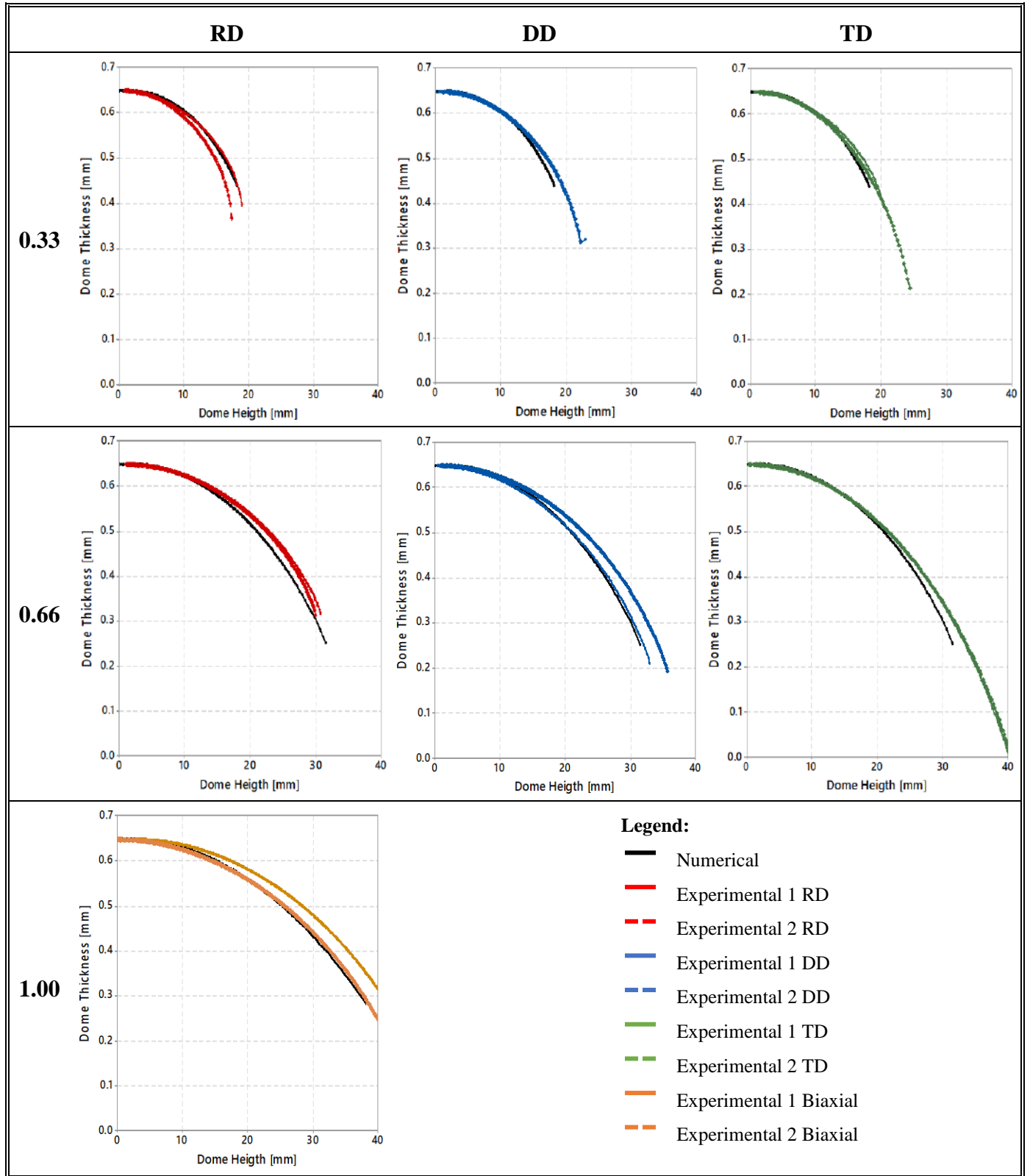


Figure 3-15: Dome thickness evolution during bulge test for all conditions.

3.4 Discussion

The elastoplastic behavior of Zn20 alloy has been successfully conducted through a CPB-06 advance yield function and the Swift hardening law in its associated form. The findings and issues of the applied methodology are discussed below.

For the Zn20 alloy, the engineering UTS is reached, as reported in Table III-1, around 10% of strain for all samples, drastically reducing the number of points for the fitting process. A significant change in the standard methodology is made to avoid this issue, moving the UTS from the engineering curves to the true stress and strain. While for other materials, the homogenous state is only valid until the engineering UTS, in Zn20, the localization process extends over a wide area in the gauge length, generating minor variations in the strain field.

The assumption of a homogenous strain state up to the onset of necking in a wide area of the sample can be seen in Figure 3-5, where for all main directions, the variation of strain is not greater than 0.05 along the longitudinal axis. The strain range from UTS to OSN allows the calibration range to be extended from a 10% strain to 35% in RD (reference direction), thus improving the fitting process. Except for the work by Leonard et al. (Leonard et al., 2017), the strain homogeneity in zinc alloy as presented in Figure 3-7 has not been covered in the referenced research. The late presence of a broader strain homogeneous area represents a global reduction of the cross-section instead of a localized necking process.

Figures 3-9 and 3-10 show the curves from the calibration process, while Tables III-4, III-5, and III-6 give the RMSE for the hardening and Lankford computation. All these results are obtained analytically with the process described in Section 3.2.4.

From RD to DD, the experimental hardening curve is well approached by the analytical expressions with an RMSE ranging from 1.08 to 4.95 MPa. For 67.5° and TD, the approach is less precise but still has a good representation of the observed behavior, with an RMSE for TD of 7.61 MPa. For the Lankford coefficients, the analytically obtained values are very close to the experimental average. Here, the RMSE in all five directions never arises over 0.013, which numerically reflects the constitutive model's ability to capture the alloy's plastic behavior. The good performance in describing the hardening curves and R values reinforces an associated model's choice to characterize the Zn20 elastoplastic behavior numerically. However, the faster thickness reduction shown in bulge test simulations is still a branch of this research under study.

Unlike previous studies on zinc alloys (Jansen et al., 2011, 2012, 2013, 2016; Milesi et al., 2014), the constitutive model based on the CPB-06 criterion and Swift hardening law used here shows a good agreement between the analytically and experimental hardening curves and Lankford coefficients for all five examined directions. Contrary to those referenced works, it is important to highlight that the hardening law is adjusted only in RD. Thus, the Swift hardening coefficients are not angle-dependent. This independence simplifies not only the characterization process but also the constitutive model implementation. An interesting feature of the used methodology is that the mechanical response of all other directions different from RD is obtained exclusively by the yield function (CPB-06) based on RD's hardening fitting. The results of the CPB-06 criterion, compared to those obtained in previous studies based on the Hill-48 criterion, reinforce the use of non-quadratic yield

functions for materials with Lankford values less than 1 (Cheng et al., 2017; Nurcheshmeh & Green, 2016). Besides, the use of non-associated models will be explored as an alternative to face the anisotropic behavior of this alloy.

No significant differences between the three tested directions (RD, DD, and TD) are noted in the experimental force-displacement curves and the fracture strain in the shear test. It is seen that the numerical simulations shown in Figure 12 adequately describe this feature of the experimental curves. Borodachenkova et al. (Borodachenkova et al., 2015) have reported experimental curves simulated with a similar load level for Zn alloys. It is interesting to highlight that the strong anisotropy shown in the tensile experiments does not play a role in this test concerning the force-displacement response and, by extension, the shear stress-strain curves (Mansouri, 2020; Thuillier & Manach, 2009). The numerical force-displacement curves agree with the experimental ones, with a major deviation for DD, on which an increase in the force value, compared to RD and TD, is seen from 0 to 0.8 mm. However, this difference is as much as 10% from the lesser value. A revision of the experimental rig and setup needs to be done together with more shear samples to determine the experimental variability of the force-displacement curves in the presented device and minimize the uncertainty of this test. From the initial behavior to the end of the experiment, the shape and force values are comparable between experimental and numerical results for RD, DD, and TD. In the RD and DD cases, the curves are below the experimental, while in TD, the numerical values tend to rise in the last part of the simulation (from 0.7 mm). In the case of the strain fields, the distribution and magnitude are comparable for the three analyzed directions.

The results of the bulge test strain-strain diagrams shown in Figure 13 and Figure 14 show a good agreement for all directions and masks. In general, the experimental and numerical results show that the mask shape governs the strain path evolution, while the anisotropy determines the extension of the strain path; meaning that, regardless of the alignment of the anisotropy axis to the major axis of the mask, the strain path evolves similarly (equivalent slope) but varies in the final strain point (e_1 , e_2).

A limitation of the numerical model is an early necking appearance compared to that registered in the experiment. The consequent short deformation range exhibited in most numerical strain-strain curves can be reinforced by the dome thickness vs. dome height curves shown in Figure 15. Here, the numerical curve is placed below the experimental ones for most of the masks and directions, meaning a faster thickness reduction of the dome in the simulation. However, the bulge test results validate the proposed model based on its ability to estimate the strain evolution and thickness reduction. Further analysis needs to be done to extend the range of these simulations to match the final experimental strain and the strain evolution of points outer from the dome. Moreover, the effect of the more complicated boundary conditions (i.e., friction between the draw bed, sheet, and clamping ring) and pressure evolution during the test, like those reported by Chen et al. (Chen, 2020; Chen et al., 2016), could be explored.

3.5 Conclusions

It has been demonstrated that the use of CPB-06 gives enough flexibility to capture the anisotropy and strain evolution in different load scenarios compared to those studies based on Hill-48. The simulations show, in general, a good agreement in the

strain path and strain evolution, independent of the test's condition. The calibration of the constitutive model parameters was obtained exclusively from the tensile test in RD, 22.5, DD, 67.5, and TD, and compression test in TD ($k=0$), while the hardening parameters were adjusted exclusively from RD data. The CPB-06 yield function replicates the hardening behavior and Lankford values based on a unique set of anisotropy coefficients and a very well-known hardening law. Based on the DIC results, the definition of UTS in the true stress-strain curve validates the consideration of a homogenous state for this alloy that extends the fitting range and improves the analytical and numerical results of the constitutive model.

The CPB-06-Swift numerical model, in its associated form, attains a reasonable estimation of the thickness reduction of the dome and completely describes the elastoplastic behavior of Zn20 alloy for different forming conditions. However, further improvements need to be done to simulate the complete strain path for bulge tests and match the experimental necking with the numerical rise in strain.

4 VISCOPLASTIC AND TEMPERATURE BEHAVIOR OF ZN-CU-TI ALLOY SHEETS: EXPERIMENTS, CHARACTERIZATION, AND MODELING

Published in *Journal of Materials Research and Technology*, 2021.

4.1 Introduction

The use of Zn-Ti-Cu alloys has been especially pulled by construction and architecture applications. These areas take advantage of the excellent corrosion resistance and long-lasting surface finish from zinc, while titanium increases its mechanical resistance and copper improves its malleability. These features allow skin-type creations in vanguard projects. Besides, its cost is considerably lower than other materials such as titanium. Despite its wide range of applications and advantages, there is a reduced number of research works on these types of alloys. These studies on Hexagonal Close-Packed focus on metals like titanium, magnesium, or zirconium (Barros et al., 2016; Chandola et al., 2015; Gilles et al., 2011; Kabirian & Khan, 2015; Kakogiannis et al., 2018; Revil-Baudard et al., 2014; Williams & Boyle, 2016).

The rolling process in zinc alloy production generates significant texture changes inducing a high dependency with the material orientation, increasing the difficulty of describing the plastic behavior of this material. In particular, rolled zinc alloys exhibit Lankford coefficients below 1 and significantly different between directions. Furthermore, the hardening has a significant and consistent rise for the rolling to the transverse direction. Studies on zinc alloys have focused mainly on determining its formability under different loading paths and the evolution of its texture. A detailed

description of zinc alloys anisotropy and the influence of the rolling process can be found in the works of Phillippe et al., Faur and Cosmeleață, Pantazopoulos et al., Milesi et al., Schlosser et al., and Alister et al. (Alister et al., 2021; Diot et al., 1998; Faur & Cosmeleață, 2006; Fundenberger et al., 1997; Milesi et al., 2017; Pantazopoulos et al., 2017; Philippe et al., 1991, 1994; Schlosser et al., 2019). From a different point of view, all these works present experimental results that evidence the marked anisotropy of rolled zinc alloys in terms of hardening and plastic strain related to the direction of the samples, performing a material characterization under quasi-static and isothermal conditions.

The anisotropy behavior of zinc alloys has been studied using crystal models and phenomenological frameworks. For example, Cauvin, Schwindt, and Borodachenkova (Borodachenkova et al., 2015; Cauvin et al., 2018; Schwindt, 2015) use the viscoplastic self-consistent (VPSC) approach to describe the plastic behavior of zinc alloys based on the texture evolution under quasi-static and isothermal conditions. From a phenomenological view, the research of Jansen and Milesi (Jansen et al., 2011, 2012, 2013, 2016; Milesi et al., 2010, 2014, 2017) focuses on modeling the behavior of zinc alloys in different forming processes. In their works, Jansen and Milesi developed the “Fiber Vector” concept to determine zinc formability via the Forming Limit Diagram (FLD). The “Fiber Vector” defines the Eigen stress and strains through angle-dependent parameters related to Hill 48 anisotropy coefficients to describe the anisotropic behavior of metal sheets, mainly applied on Zn-Cu-Ti alloys. The work of Milesi et al. is extended in Alister et al. (Alister et al., 2021), using the CPB-06 yield function to face the numerical

estimation of zinc alloy behavior. However, all these works are established under a strain-rate independent and isothermal framework.

The material response under different forming conditions has been reported in Leonard (Schlosser et al., 2019) and Milesi (Milesi, Lecoq, et al., 2020), showing that similar zinc alloys present high strain rate sensitivity. Furthermore, (Diot et al., 1998; Milesi, Pino, et al., 2020; Philippe et al., 1991) studied Zn-Cu and Zn-Cu-Ti alloy's response under different temperature conditions and its effect on material formability showing this condition's influence. It is worth mentioning that the high sensitivity to temperature and strain rate makes self-heating effects significant in the material behavior. Milesi *et al.* studied the effect of self-heating phenomena in (Milesi, Pino, et al., 2020), where the plastic work was analyzed using numerical and experimental tests. Although these researches show the strong influence of strain rate and temperature in the material behavior, no one of them analyzes both factors in the numerical modeling of Zinc alloys.

In this work, using the CPB-06 yield function (Cazacu et al., 2006; Plunkett et al., 2008) and the Johnson-Cook hardening law (Johnson & Cook, 1983), the anisotropy of a Zn-Ti-Cu alloy is experimentally characterized and modeled to establish a material description involving strain-rate and temperature-dependent effects as a framework for further numerical simulations in different forming scenarios.

4.2 Materials and Methods

4.2.1 Material

The material used in this work is a sheet of Zn-Cu-Ti alloy named Zn-20, with a nominal thickness of 0.65 mm. All test samples were cut along the rolling direction RD (0°), diagonal direction DD (45°), and transversal direction TD (90°). RD and TD are aligned with the x - and y -axis of the reference system. As a result, the z -axis is the out-of-plane component.

The uniaxial tensile stress-strain curves show no significant difference for all samples' elasticity moduli (E). The E value was established to 99.0 GPa (Ledbetter, 1977). No variation of E related to temperature or strain rate was considered in this study. The Poisson ratio is 0.24 (Tromans, 2011). The yield stress σ_{yp} was obtained with the 0.002 strain offset.

The Lankford coefficients were computed from the DIC images over the gauge area from the yield point to the maximum stress in the true-stress strain curve. Leonard et al. (Leonard et al., 2019) and Alister et al. (Alister et al., 2021) showed that a homogeneous state could be considered until such point for the Zn20 (Onset of Necking). Mean values for R of 0.24, 0.33, and 0.73 for RD, DD, and TD, respectively, were found. There is no significant difference for R values in the same direction at different testing conditions.

4.2.2 Experimental Procedure

Uniaxial tensile tests were carried out with an Instron 5967 Universal Testing machine, equipped with a 30 kN load cell and an isolated heating chamber for

temperature dependence experiments. Two repetitions per direction (RD, DD, and TD) and condition (strain rate and temperature) were performed for a total of 30 experiments. The sample shape was defined according to ASTM E8-8M. All specimens were cut along the three main directions described above (RD, DD, and TD). All experiments performed are detailed in Table IV-1. Figure 4-1 shows the experimental setups for the strain-rate and temperature experiments together with the speckled tensile samples used.

Table IV-1: Experiments performed.

Condition	Direction	Qty.	Strain Rate s⁻¹	Temperature °C
Low strain-rate low temperature (Control)	RD	2	0.002	20
	DD	2	0.002	20
	TD	2	0.002	20
Medium strain-rate low temperature (0.02 s ⁻¹)	RD	2	0.02	20
	DD	2	0.02	20
	TD	2	0.02	20
High strain-rate low temperature (0.2 s ⁻¹)	RD	2	0.2	20
	DD	2	0.2	20
	TD	2	0.2	20
Low strain-rate medium temperature (60 °C)	RD	2	0.002	60
	DD	2	0.002	60
	TD	2	0.002	60
Low strain-rate high temperature (80 °C)	RD	2	0.002	80
	DD	2	0.002	80
	TD	2	0.002	80

The displacement and later strain field computation were obtained with a 3D Digital Image Correlation (3D DIC) system VIC 3D 8 by Correlated Solutions. Two pairs of high-resolution cameras with 4.0 Megapixels resolution at 10 frame per seconds (fps) were used (Point Grey Grasshopper for strain rate and Allied Technologies Pike for temperature dependency). The post-process parameter to obtain the strain fields was set to 19 and 3 pixels for the grid and step size. The load data was recorded for each time step and frame using an analog-digital converter provided by National Instruments (Alister et al., 2021).

An isolated chamber with controlled temperature was used for the variable temperature tests, containing the grips and samples. At the same time, the samples were stored inside the chamber to standardize their temperature to the test conditions. Three minutes of holding time were used for each test to stabilize the chamber temperature after mounting the new sample.

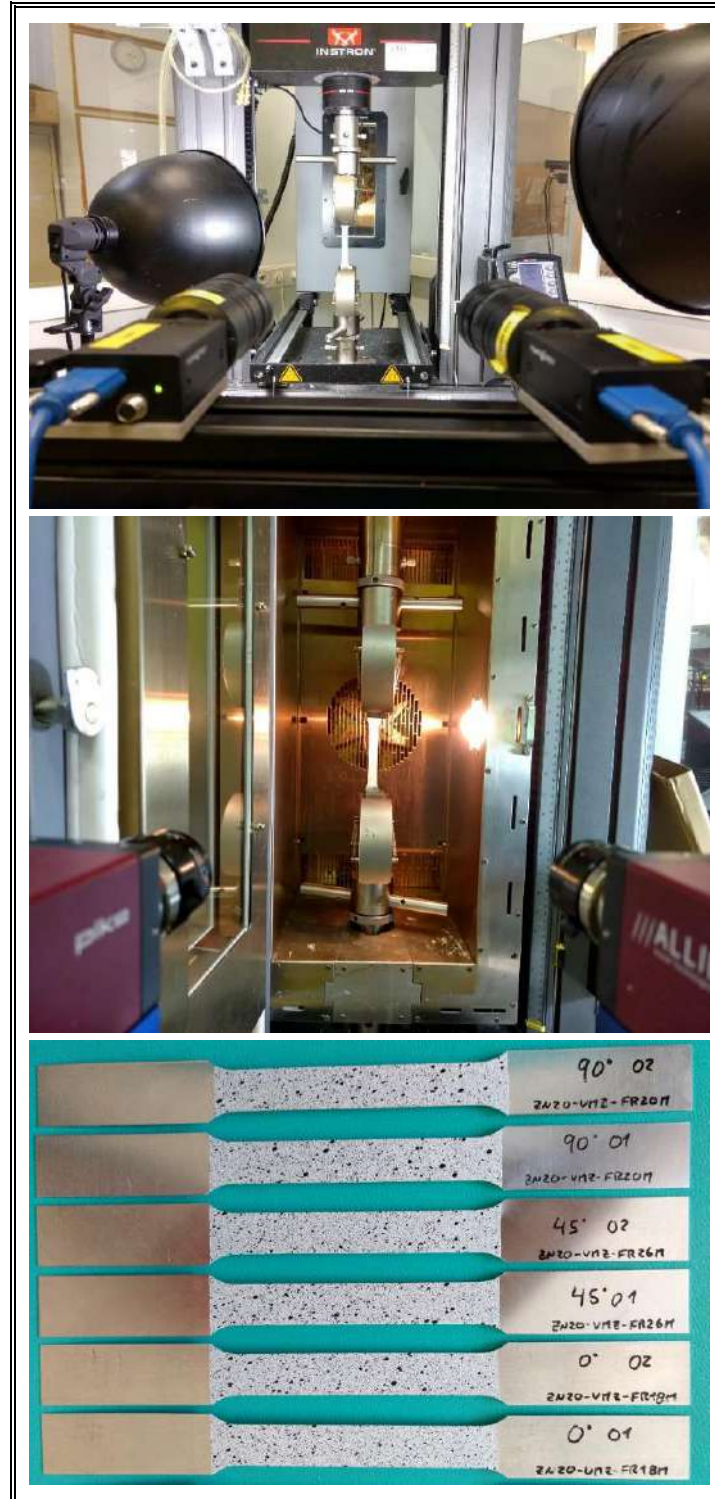


Figure 4-1: Top: Strain-rate setup. Middle: The heating chamber for variable temperature experiments. Bottom: ASTM E8 test samples with speckle pattern.

4.2.3 Constitutive Model

The constitutive model adopted in this work modified that already reported in (Alister et al., 2019, 2021; Cazacu et al., 2006; Plunkett et al., 2006, 2008). The model considers an elastic and viscoplastic material model under an associated flow rule. Besides, the strain rate and temperature dependencies are driven through the use of a Johnson-Cook hardening model.

The constitutive model is implemented in an in-house finite element code with a radial-return scheme based on the Newton-Raphson iterative method (Celentano et al., 2012).

a) Yield Function

The CPB-06 yield criterion chosen to describe the material behavior is written as (Cazacu et al., 2006; Johnson & Cook, 1983; Plunkett et al., 2006, 2008):

$$F_{(\boldsymbol{\sigma}, \bar{\varepsilon}_p, \dot{\bar{\varepsilon}}_p, T^\circ)} = \bar{\sigma}(\boldsymbol{\sigma}) - Y_{(\bar{\varepsilon}_p, \dot{\bar{\varepsilon}}_p, T^\circ)} = 0 \quad (4.1)$$

where $\bar{\sigma}$ is the equivalent stress, $\boldsymbol{\sigma}$ is the Cauchy stress tensor (in a general Cartesian reference system), and Y is the isotropic strain rate and temperature-dependent hardening stress for which $\bar{\varepsilon}_p$ is the equivalent plastic strain, $\dot{\bar{\varepsilon}}_p$ is its strain rate, and T° is the material temperature. The equivalent stress is given by:

$$\bar{\sigma}(\boldsymbol{\sigma}) = \left(\frac{f}{B_{0^\circ}} \right)^{\frac{1}{a}} \quad (4.2)$$

where f and B_{0° are defined as:

$$f = (|\Sigma_1| - k\Sigma_1)^a + (|\Sigma_2| - k\Sigma_2)^a + (|\Sigma_3| - k\Sigma_3)^a \quad (4.3)$$

$$B_{0^{\circ}} = (|\gamma_1| - k\gamma_1)^a + (|\gamma_2| - k\gamma_2)^a + (|\gamma_3| - k\gamma_3)^a \quad (4.4)$$

and γ_i are:

$$\gamma_1 = \left(\frac{2}{3}L_{11} - \frac{1}{3}L_{12} - \frac{1}{3}L_{14} \right) \quad (4.5)$$

$$\gamma_2 = \left(\frac{2}{3}L_{12} - \frac{1}{3}L_{22} - \frac{1}{3}L_{24} \right) \quad (4.6)$$

$$\gamma_3 = \left(\frac{2}{3}L_{14} - \frac{1}{3}L_{24} - \frac{1}{3}L_{44} \right) \quad (4.7)$$

For a plane stress case, the principal components of equation (4.3) can be described as follows:

$$\Sigma_1 = \frac{1}{2} \left(\Sigma_{xx} + \Sigma_{yy} + \sqrt{(\Sigma_{xx} - \Sigma_{yy})^2 + 4\Sigma_{xy}^2} \right) \quad (4.8)$$

$$\Sigma_2 = \frac{1}{2} \left(\Sigma_{xx} + \Sigma_{yy} - \sqrt{(\Sigma_{xx} - \Sigma_{yy})^2 + 4\Sigma_{xy}^2} \right) \quad (4.9)$$

$$\Sigma_3 = \Sigma_{zz} \quad (4.10)$$

where Σ_{xx} , Σ_{yy} , Σ_{xy} and Σ_{zz} are the general components of the modified Cauchy stress tensor explicitly described as:

$$\Sigma_{xx} = \left(\frac{2}{3}L_{11} - \frac{1}{3}L_{12} - \frac{1}{3}L_{14} \right) \sigma_{xx[m]} + \left(-\frac{1}{3}L_{11} + \frac{2}{3}L_{12} - \frac{1}{3}L_{14} \right) \sigma_{yy[m]} \quad (4.11)$$

$$\Sigma_{yy} = \left(\frac{2}{3}L_{12} - \frac{1}{3}L_{22} - \frac{1}{3}L_{24} \right) \sigma_{xx[m]} + \left(-\frac{1}{3}L_{12} + \frac{2}{3}L_{22} - \frac{1}{3}L_{24} \right) \sigma_{yy[m]} \quad (4.12)$$

$$\Sigma_{zz} = \left(\frac{2}{3}L_{14} - \frac{1}{3}L_{24} - \frac{1}{3}L_{44} \right) \sigma_{xx[m]} + \left(-\frac{1}{3}L_{14} + \frac{2}{3}L_{24} - \frac{1}{3}L_{44} \right) \sigma_{yy[m]} \quad (4.13)$$

$$\Sigma_{xy} = L_{33} \sigma_{xy[m]} \quad (4.14)$$

where $\sigma_{ij[m]}$ are the Cauchy stress tensor components based on the material reference system $[m]$. Besides, L_{ij} are the anisotropic coefficients related to the texture evolution of the material. The $\sigma_{ij[m]}$ components described in the tensile test reference system $\sigma_{ij[r]}$ are:

$$\sigma_{xx[m]} = \sigma_{xx[r]} \cos^2 \theta + \sigma_{yy[r]} \sin^2 \theta + 2 \sin \theta \cos \theta \sigma_{xy[r]} \quad (4.15)$$

$$\sigma_{yy[m]} = \sigma_{xx[r]} \sin^2 \theta + \sigma_{yy[r]} \cos^2 \theta - 2 \sin \theta \cos \theta \sigma_{xy[r]} \quad (4.16)$$

$$\sigma_{xy[m]} = (\sigma_{yy[r]} - \sigma_{xx[r]}) \sin \theta \cos \theta + \sigma_{xy[r]} (\cos^2 \theta - \sin^2 \theta) \quad (4.17)$$

It can be demonstrated that for any uniaxial stress state, the yield function (4.3) can be expressed in terms of:

$$f = \sigma_{\theta^{\circ}}^a [(|\Sigma_1| - k\Sigma_1)^a + (|\Sigma_2| - k\Sigma_2)^a + (|\Sigma_3| - k\Sigma_3)^a] = \sigma_{\theta^{\circ}}^a B_{\theta^{\circ}} \quad (4.18)$$

$$\bar{\sigma}_{\theta} = \left(\frac{B_{0^{\circ}}}{B_{\theta^{\circ}}} \right)^{\frac{1}{a}} Y_{(\bar{\varepsilon}_p, \dot{\bar{\varepsilon}}_p, T^{\circ})} \quad (4.19)$$

where σ_θ^a is the stress applied in the defined direction, and γ are deduced from the previous equations (4.5 to 4.7). The sub-index θ° denotes the angle referenced to the RD, and a is the degree of homogeneity. Finally, the asymmetry coefficient k is obtained from:

$$k = 1 - \frac{\left\{ \frac{2^a - 2 \left(\frac{\sigma_t}{\sigma_c} \right)^a}{\left(2 \left(\frac{\sigma_t}{\sigma_c} \right)^a - 2 \right)} \right\}^{\frac{1}{a}}}{1 + \left\{ \frac{2^a - 2 \left(\frac{\sigma_t}{\sigma_c} \right)^a}{\left(2 \left(\frac{\sigma_t}{\sigma_c} \right)^a - 2 \right)} \right\}^{\frac{1}{a}}} \quad (4.20)$$

where $\frac{\sigma_t}{\sigma_c}$ is the ratio between the yield values at tension and compression over the same direction. Both σ_t and σ_c are obtained from the uniaxial tensile and compression tests. If the material shows no asymmetry, k is equal to 0. Specifically, for the Zn-20 sheet alloy in this work, symmetric behavior is considered (Alister et al., 2021).

Based on the equivalent stress definition (4.2), the Lankford coefficients, considering plastic incompressibility, are defined in the reference frame as:

$$R_{\theta^\circ}^{num} = - \frac{\frac{\partial \bar{\sigma}}{\partial \sigma_{yy[r]}}}{\frac{\partial \bar{\sigma}}{\partial \sigma_{xx[r]}} + \frac{\partial \bar{\sigma}}{\partial \sigma_{yy[r]}}} \quad (4.21)$$

b) Hardening Function

The hardening behavior is represented by the Johnson-Cook law (Johnson & Cook, 1983) written for RD as:

$$Y_{(\bar{\varepsilon}_p, \dot{\bar{\varepsilon}}_p, T^\circ)} = K(\bar{\varepsilon}_0 + \bar{\varepsilon}_p)^n \left[1 + C_1 \ln \left(\frac{\dot{\bar{\varepsilon}}_p}{\dot{\bar{\varepsilon}}_{ref}} \right) \right] \left[1 - \left(\frac{T - T_{ref}}{T_{fusion} - T_{ref}} \right)^{C_2} \right] \quad (4.22)$$

Quasi-Static Strain Rate Temperature-dependent

The function can be divided into quasi-static strain, strain rate, and temperature components. For the quasi-static part, K is the strength coefficient, n is the hardening exponent, and $\bar{\epsilon}_0 = \left(\frac{\sigma_{yp}^{RD}}{K}\right)^{\frac{1}{n}}$, σ_{yp}^{RD} being the yield strength for RD. The rate of the equivalent plastic strain is $\dot{\bar{\epsilon}}_p = \frac{\sigma_{[m]}:\dot{\epsilon}_p}{\bar{\sigma}}$, such that ϵ_p is the plastic strain tensor with the associated flow rule $\dot{\epsilon}_p = \dot{\lambda} \frac{\partial \bar{\sigma}}{\partial \sigma_{[m]}}$, where $\dot{\lambda}$ is the plastic consistency parameter. Moreover, in the strain rate component $\dot{\epsilon}_{ref}$ is the reference and lower strain rate (0.002 s⁻¹), $\dot{\epsilon}$ is the actual strain rate and C_1 is the strain rate coefficient to be fitted. Lastly, in the temperature component, T_{ref} is the reference temperature, defined to be equal to the lower temperature in tests (20 °C), T_{fusion} is the fusion temperature of the alloy considered as pure Zinc (419.5 °C), and T is the actual temperature of the test. Finally, C_2 is the temperature coefficient to be fitted.

4.2.4 Model Calibration

The calibration is performed in the plastic range, from the yield point until the Onset of Necking (OS-necking). The yield point is determined based on the Elasticity Modulus defined in 4.1. As was mentioned, no variation related to the strain rate or temperature is considered in the elastic range. The fitting procedure is an extension of Alister et al. 2019 and 2021 (Alister et al., 2019, 2021).

a) Hardening Coefficients

i) Quasi-static Component

The quasi-static component of equation (4.22) is the Swift hardening law, resulting from applying the reference strain rate (0.002 s^{-1}) and temperature ($20 \text{ }^\circ\text{C}$). The Swift coefficients (K, n) were obtained from the minimization of expression (4.24) based on its explicit form (4.23) for the two RD experiments at the control condition, i.e., the reference strain rate and temperature; see Table 1.

$$Y_{(\bar{\varepsilon}_p, \dot{\varepsilon})} = K \left[\left(\frac{\sigma_{yp}^{RD}}{K} \right)^{\frac{1}{n}} + \bar{\varepsilon}_p \right]^n \quad (4.23)$$

$$Error_{\bar{\varepsilon}} = \sum_{i=1}^m \left(\frac{Y_{(\bar{\varepsilon}_p)}}{\sigma_{RD}^{exp}} - 1 \right)_i^2 \quad (4.24)$$

where $Y_{(\bar{\varepsilon}_p)}$ is the expression (4.23) and σ_{RD}^{exp} is the experimentally measured stress values for RD, both experimental and numerical, at the reference strain rate and temperature.

ii) Strain Rate Component

The strain rate component is derived from expression (4.22) at the reference temperature of $20 \text{ }^\circ\text{C}$. The coefficient C_I results from the minimization of expression (4.26) based on the expression (4.25) for all the RD experiments at strain rates different from the reference one, i.e., they correspond to values of 0.02 and 0.2 s^{-1} (see Table IV-1).

$$Y_{(\bar{\varepsilon}_p, \dot{\varepsilon})} = K(\bar{\varepsilon}_0 + \bar{\varepsilon}_p)^n \left[1 + C_1 \ln \left(\frac{\dot{\varepsilon}}{\dot{\varepsilon}_{ref}} \right) \right] \quad (4.25)$$

$$Error_{\dot{\varepsilon}} = \sum_{i=1}^m \left(\frac{Y_{(\bar{\varepsilon}_p, 0.02)}}{\sigma_{0.02}^{exp}} - 1 \right)_i^2 + \sum_{i=1}^n \left(\frac{Y_{(\bar{\varepsilon}_p, 0.2)}}{\sigma_{0.2}^{exp}} - 1 \right)_i^2 \quad (4.26)$$

where $Y_{(\bar{\varepsilon}_p, 0.02)}$ and $Y_{(\bar{\varepsilon}_p, 0.2)}$ are expression (4.25) for strain rates of 0.02 and 0.2, respectively, and $\sigma_{0.02}^{exp}$ and $\sigma_{0.2}^{exp}$ are the experimentally measured stress values for each strain rate at the reference temperature.

iii) Temperature Component

The temperature-dependent component is derived from expression (4.22) at the reference strain rate of 0.002 s^{-1} . Coefficient C_2 results from the minimization of expression (4.28) using equation (4.27) for all RD experiments at temperatures different from the reference, i.e., they correspond to values of 60 and 80 °C (see Table 1).

$$Y_{((\bar{\varepsilon}_p, T^{\circ}))} = K(\bar{\varepsilon}_0 + \bar{\varepsilon}_p)^n \left[1 - \left(\frac{T - T_{ref}}{T_{fusion} - T_{ref}} \right)^{C_2} \right] \quad (4.27)$$

$$Error_{\dot{\varepsilon}} = \sum_{i=1}^m \left(\frac{Y_{(\bar{\varepsilon}_p, 60)}}{\sigma_{60}^{exp}} - 1 \right)_i^2 + \sum_{i=1}^n \left(\frac{Y_{(\bar{\varepsilon}_p, 80)}}{\sigma_{80}^{exp}} - 1 \right)_i^2 \quad (4.28)$$

were $Y_{(\bar{\varepsilon}_p, 60)}$ and $Y_{(\bar{\varepsilon}_p, 80)}$ are expression (4.27) for temperatures of 60 and 80 °C, respectively, and σ_{60}^{exp} and σ_{80}^{exp} are the experimentally measured stress values for each temperature at the reference strain rate.

b) CPB-06 Anisotropic Coefficients L_{ij}

The material parameters of the constitutive model presented are derived through a fitting procedure that only considers the tensile test results. CPB-06 coefficients are obtained using the methodology described in (Alister et al., 2019, 2021). This methodology minimizes the error between the experimental and corresponding analytical values of the tensile true stress-strain curves and Lankford coefficients for three main directions under the different strain and temperature conditions.

$$\begin{aligned}
 Error_L = & W_{45^\circ}^T \sum_{i=1}^m \left(\frac{\sigma_{45^\circ}^{num}}{\sigma_{45^\circ}^{exp}} - 1 \right)_i^2 + W_{90^\circ}^T \sum_{i=1}^m \left(\frac{\sigma_{90^\circ}^{num}}{\sigma_{90^\circ}^{exp}} - 1 \right)_i^2 + \\
 & W_{0^\circ}^R \sum_{i=1}^m \left(\frac{R_{0^\circ}^{num}}{R_{0^\circ}^{exp}} - 1 \right)_i^2 + W_{45^\circ}^R \sum_{i=1}^m \left(\frac{R_{45^\circ}^{num}}{R_{45^\circ}^{exp}} - 1 \right)_i^2 + W_{90^\circ}^R \sum_{i=1}^m \left(\frac{R_{90^\circ}^{num}}{R_{90^\circ}^{exp}} - 1 \right)_i^2
 \end{aligned}
 \tag{4.29}$$

In the present study, L_{11} , L_{55} , and L_{66} were set to 1 (Cazacu et al., 2006, 2010; Chandola et al., 2015; Muhammad et al., 2015; Revil-Baudard et al., 2014; Tuninetti et al., 2012, 2015; Yoon et al., 2013). Besides, the homogeneity degree a is set to 4, based on the work of Liu et al. (Liu et al., 1997). The weights $W_{\theta^\circ}^{T-R}$ were set to 1. In summary, the CPB-06 parameters to be obtained are the remaining six coefficients of tensor L (L_{22} , L_{33} , L_{44} , L_{12} , L_{14} , and L_{24}).

The model parameters were fitted in the plastic strain interval ranging from the yield point (σ_{yp}) up to the Onset of Necking over which homogeneous stress and plastic strain field are observed (Alister et al., 2021; Leonard et al., 2019).

Finally, the accuracy of the fitting procedure is assessed by the Root Mean Square Error (RMSE) between the experimental and corresponding analytical values for both the stress-strain curves and Lankford coefficients through the following expressions:

$$E_{\sigma} = \sqrt{\frac{1}{m} \sum_{i=1}^m (\sigma_{\theta^{\circ}}^{num} - \sigma_{\theta^{\circ}}^{exp})^2} \quad (4.30)$$

$$E_R = \sqrt{\frac{1}{m} \sum_{i=1}^m (R_{\theta^{\circ}}^{num} - R_{\theta^{\circ}}^{exp})^2} \quad (4.31)$$

4.3 Results and Discussions

The elastoviscoplastic and the temperature-dependent behavior of Zn20 alloy has been numerically described by the associated form of the CPB-06 yield function and the Johnson-Cook hardening law. The findings and issues of the applied methodology are presented and discussed below.

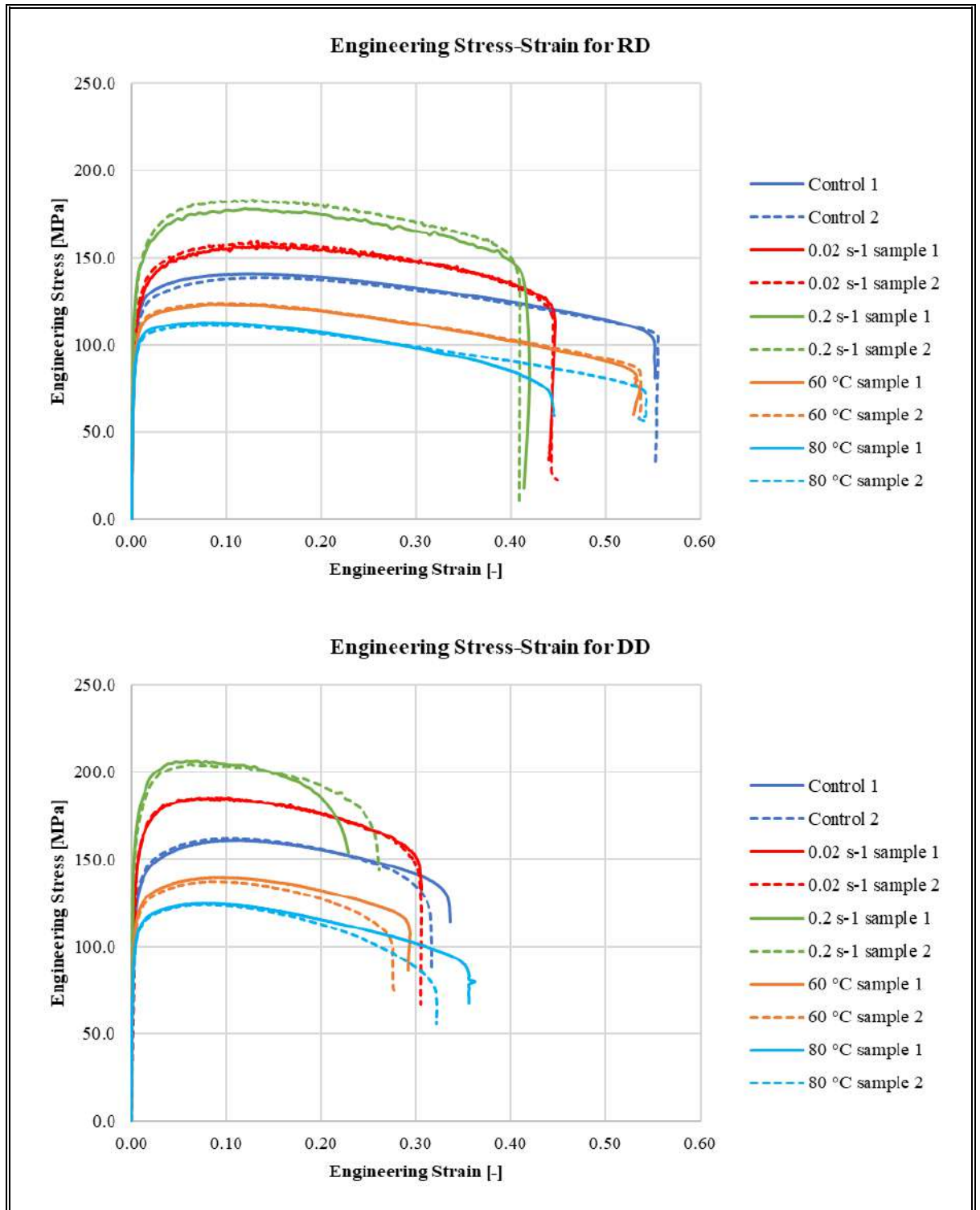
4.3.1 Experimental Results

a) Stress-Strain Curves

The studied alloy presents a high anisotropy both in terms of stress-strain curves and Lankford values. The stress-strain curves show that increments in one order of magnitude in strain rate increase the UTS by a mean of 12% without significant changes in the strain value at this point. For example, the UTS strain in RD for the control and medium strain-rate samples is around 0.13 with a stress of 138 MPa and 159.3 MPa, respectively. Although the UTS strain barely changes, the increase in strain rate induces a significant reduction in the final strain in the order of 0.15, 0.10, and 0.18 for RD, DD, and TD, from the control condition to the high strain-rate condition (Figure 4-2).

Regarding the temperature dependency, the alloy behavior is opposite to that seen in strain rate, i.e., it means that an increase of temperature induces a softening and an

increase of the ultimate strain. Contrary to strain rate, a reduction in the UTS strain value is also seen in all directions (Figure 4-2).



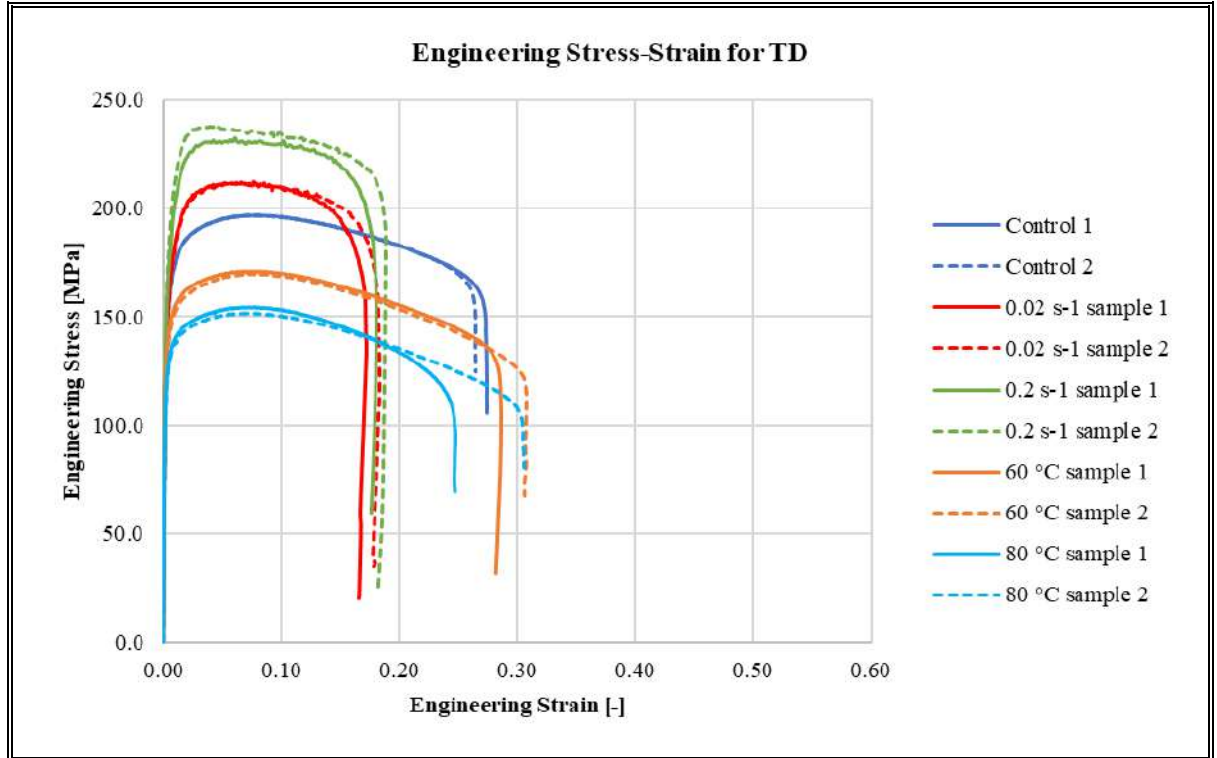
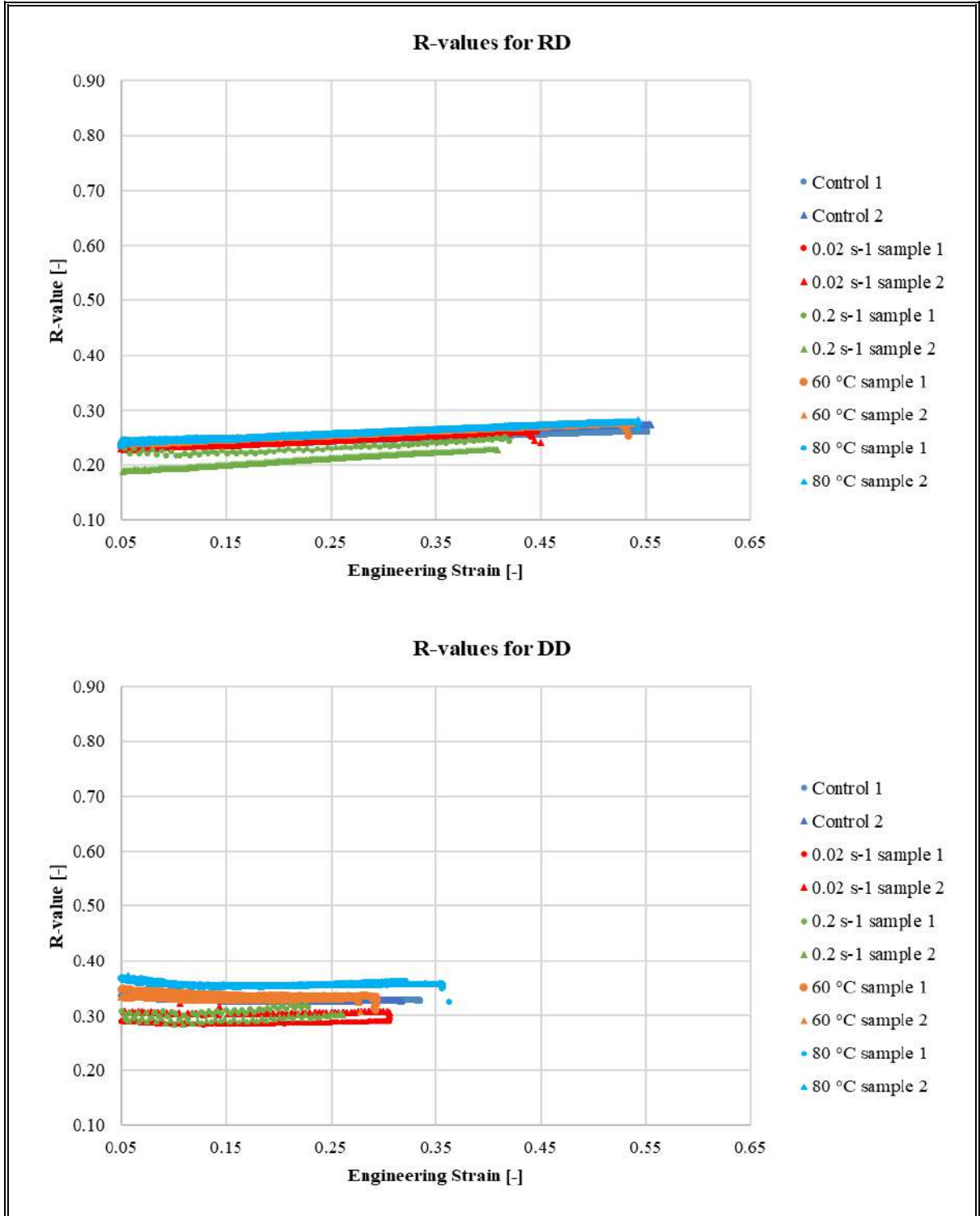


Figure 4-2: Experimental engineering stress-strain curves for all experiments and conditions.

b) Lankford Coefficients

Although there is a noticeable change in the stress-strain response under different strain rates or temperatures, the Lankford coefficients (R values) show no significant difference in their evolution. As can be seen in Figure 4-3, R value did not change their trends during the test. Consequently, RD presents a slight increase while DD has an enduring value. Finally, TD shows a steady reduction in the R value from the beginning until the end of the tests. No matter what the conditions were, the trend is the same for the same direction.



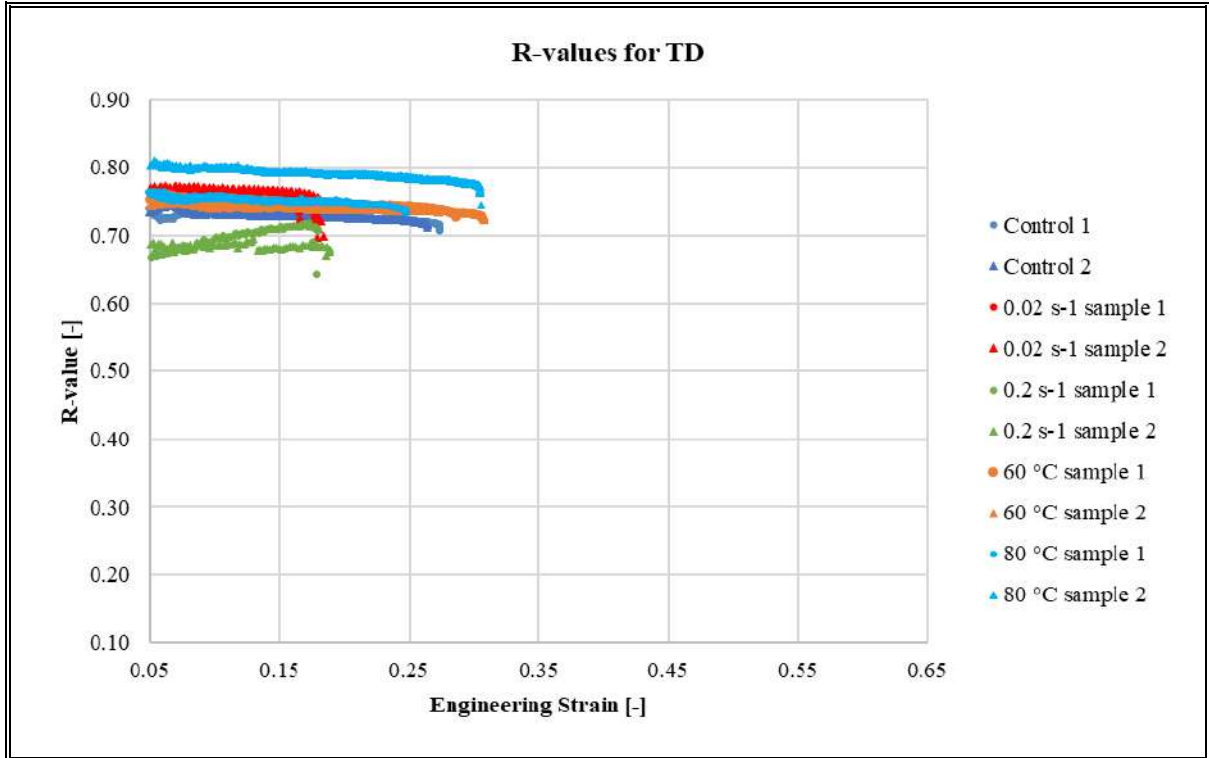


Figure 4-3: Experimental Lankford coefficient vs. engineering strain curves for all experiments and conditions.

Figure 4-4 presents the registered R values, from yield to OS Necking, averaged for two repetitions in the same condition and direction. Besides, the dispersion bars are also represented. The plot shows no significant difference between the control case (0.002 s^{-1} at $20 \text{ }^{\circ}\text{C}$) and the temperature and strain rate cases for all conditions and directions.

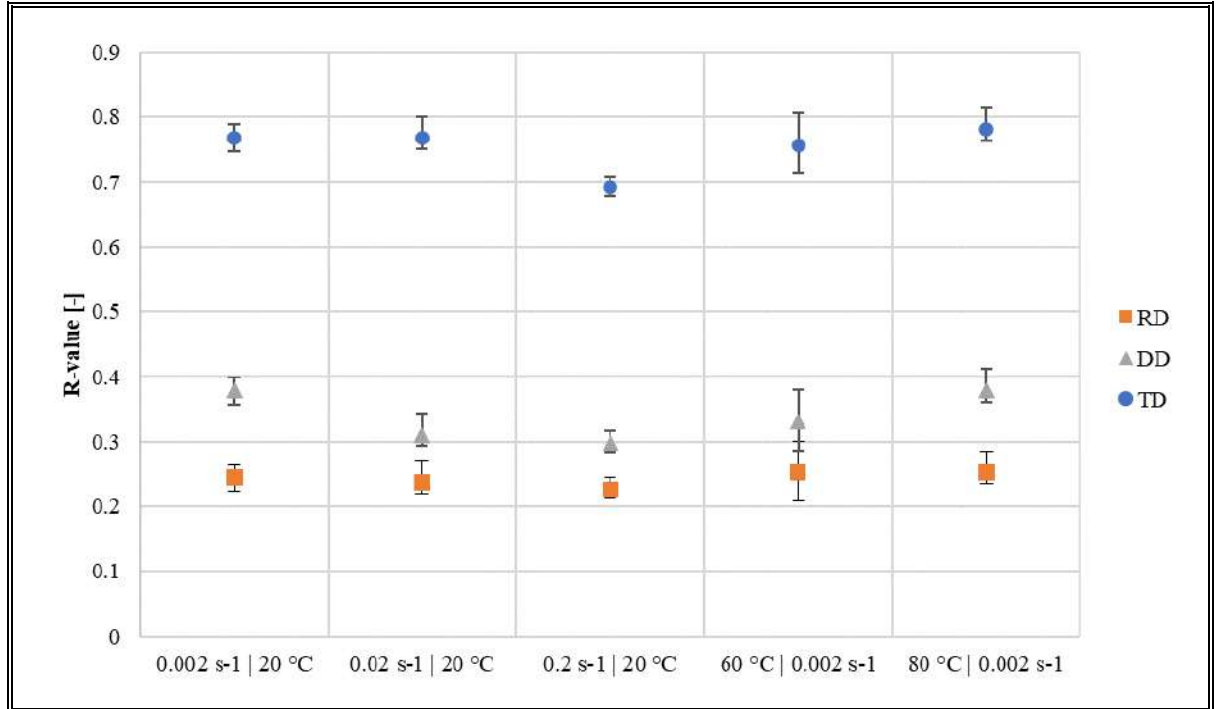


Figure 4-4: Dispersion around the mean R value for all experiments and conditions.

In general, there is a slight increment of the R value at high temperatures (80 °C) for all directions, especially for DD. On the other hand, the high strain rate condition (0.2 s⁻¹) decreases the mean R value for all directions. The maximum and minimum R values for RD are 0.23 and 0.25, respectively. For DD, 0.38 and 0.30 while for TD are 0.78 and 0.80. The maximum and minimum mean R values correspond to the high-temperature case (80 °C) and high strain rate (0.2 s⁻¹), respectively. However, based on the data scattering, it is not possible to establish a correlation in the alloy's response to the strain rate or temperature.

Even when the stress-strain curves presented in Figure 4-2 show a clear difference for a specific direction in the different conditions, the R value is almost constant. Figure

4-4 shows that there is no trend between the experimental condition and Lankford coefficients for all directions. Thus, R values can be considered independent of strain rate (0.002, 0.02, and 0.2 s⁻¹), temperature (20, 60, and 89 C°), and constants for the plastic range from yield to the OS-necking.

4.3.2 Numerical Results

a) Fitted Material Model Parameters

Based on the previous statement, it is possible to use a unique set of anisotropy L_{ij} coefficients to describe the stress and plastic behavior of the alloy. Therefore, the hardening law's definition is driven only by RD in all strain-rate and temperature conditions, while the CPB-06 yield function adapts the hardening curves to the other directions. On the other hand, the Lankford coefficients are fitted for all directions and conditions.

As was set before, no asymmetry is considered; thus, k is equal to 0. The degree of homogeneity (parameter a) was fixed to 4, based on a previous trial test (Alister et al., 2019, 2021). In addition, the experimental findings of Liu (Liu et al., 1997) and Nurcheshmeh (Nurcheshmeh & Green, 2016) show a better approximation with fourth-order yield models for some HCP materials.

The obtained Johnson-Cook and CPB-06 fitted coefficients are respectively presented in Tables IV-2 and IV-3.

Table IV-2: Johnson-Cook fitted coefficients.

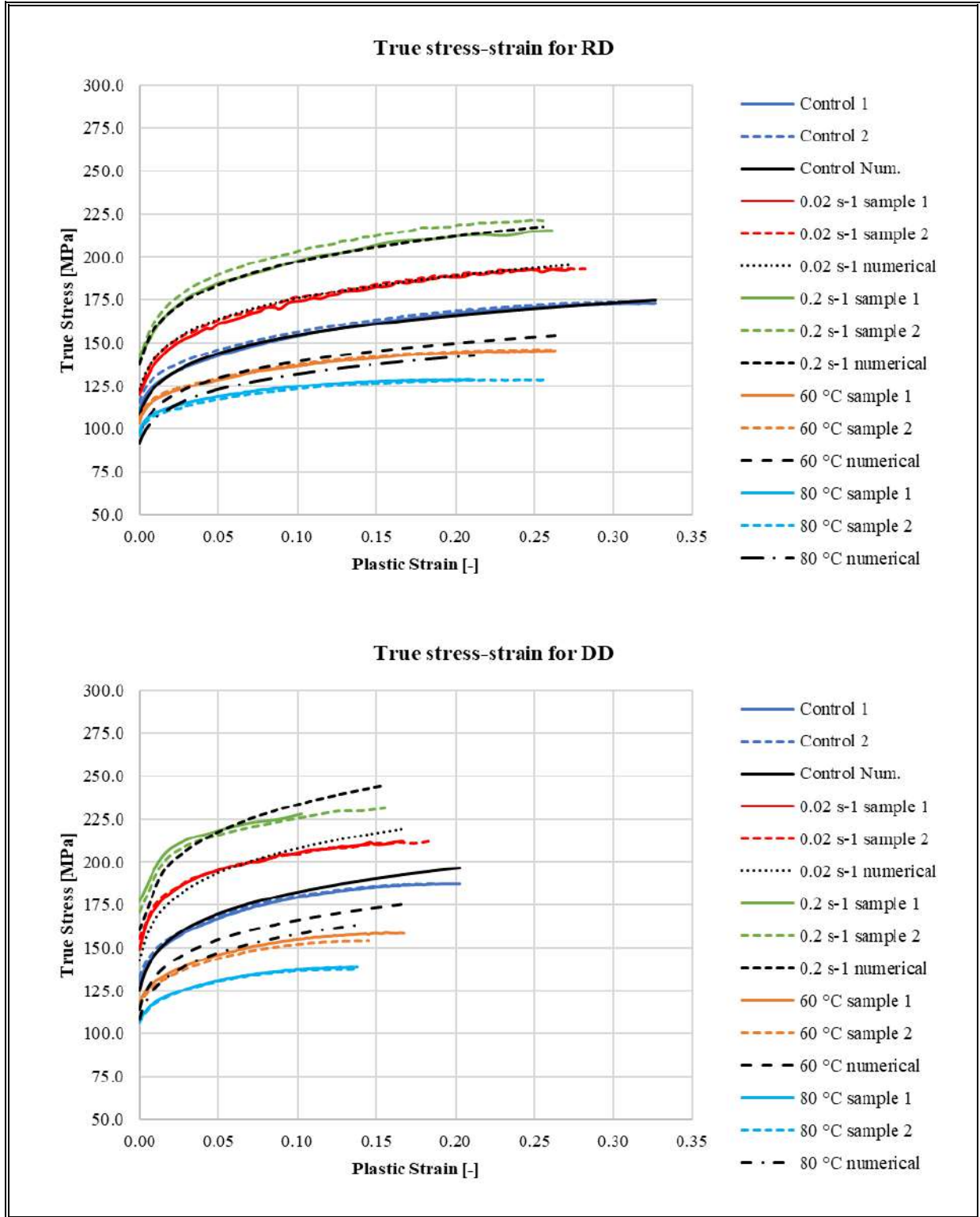
K (MPa)	ϵ_0	n	C_1	C_2
197.2	0.004	0.105	0.0615	0.9680

Table IV-3: CPB-06 fitted coefficients.

L_{12}	L_{14}	L_{22}	L_{24}	L_{33}	L_{44}	k	a
0.055	-0.191	0.853	0.025	0.856	1.056	0.0	4.0

b) Stress-Strain Curves

The result of the fitting process is applied and shown in Figure 4-5 for stress-strain curves. For all conditions, RD is the best reproduced for all combinations. However, in all directions, the alloy's softening by increasing temperature is not well represented. The adjusted true stress-strain curves for the RD, DD, and TD directions in all conditions are presented in Figure 4-5. Here, the range of interest is bounded from the yield until the OS-Necking strain.



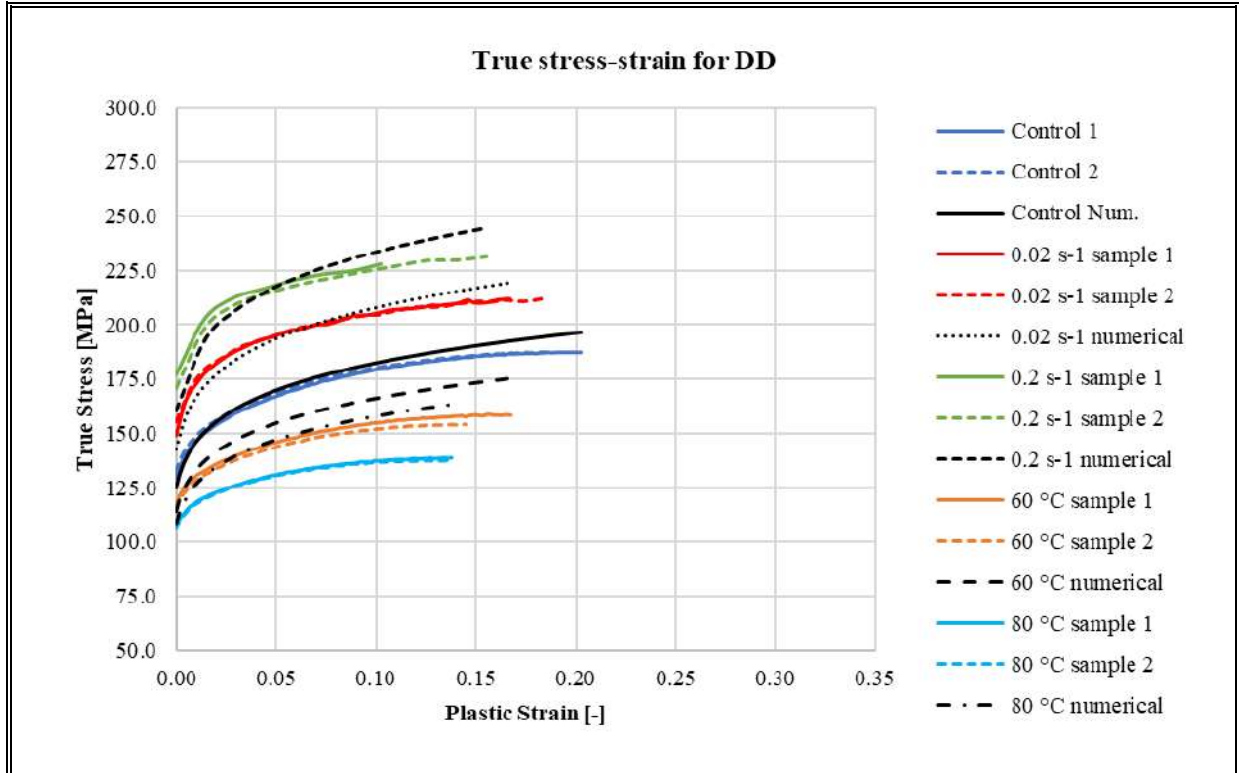


Figure 4-5: Experimental and numerical true stress-strain plots all directions and conditions. From top to bottom: RD, DD, and TD, respectively.

The plot of the yield loci at 0.1 of plastic strain for all conditions in Figure 4-6 shows the constitutive model's ability to describe the alloy's anisotropy based on a unique set of anisotropy coefficients (L_{ij}). Simultaneously, the underestimation of the yield value for TD is seen for each condition. However, the approach by CPB-06 is always better than Hill-48. The evolution of the alloy asymmetry related to the strain rate and temperature should be studied. The shape of the yield loci suggests that modifying the asymmetry coefficient “k” could improve the yield point determination for TD. The use of the non-quadratic yield function, as suggested by Liu (Liu et al., 1997) and Nurcheshmeh (Nurcheshmeh & Green, 2016), gives good results for this material.

The yield loci for a plastic strain of 0.10 and the different experiments are plotted in Figure 6 for $\sigma_{xy} = 0$. The different approximation of CPB-06 based on the same set of anisotropy coefficients compared to Hill-48 based on R values (Hill, 1948) can be seen. The colored circles denote the experimental yield values for RD and TD.

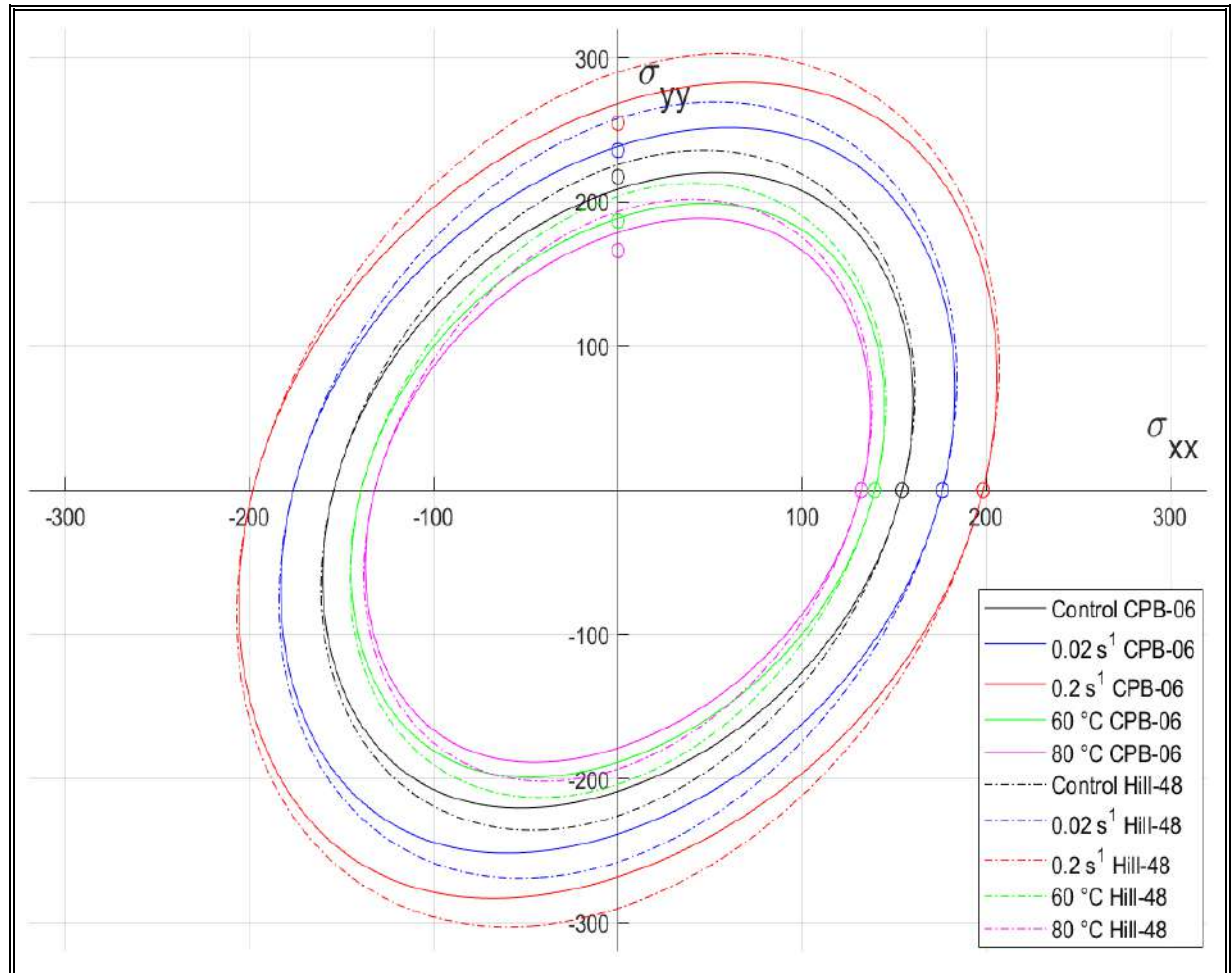


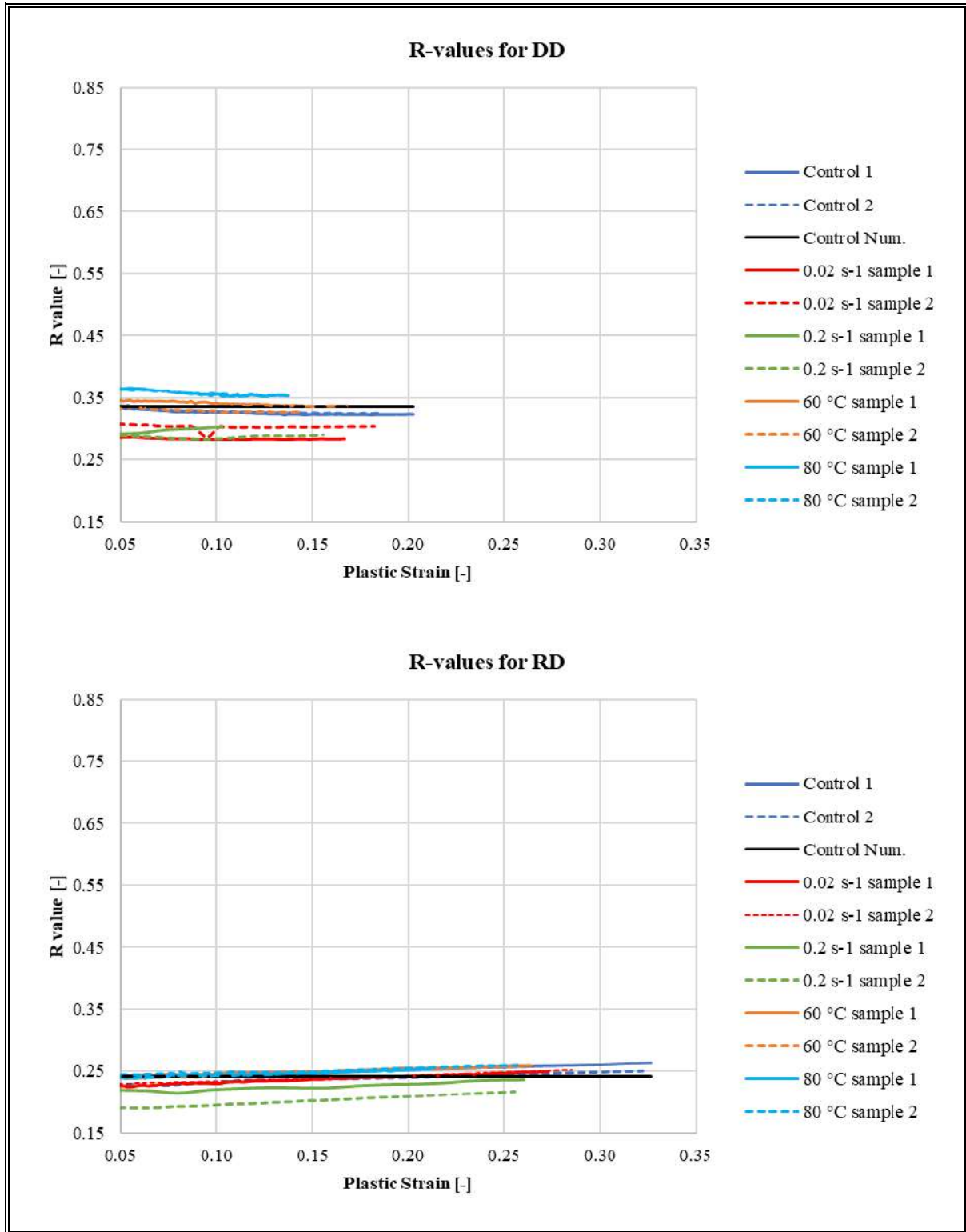
Figure 4-6: Yield loci for all conditions at 0.10 of plastic strain for $\sigma_{xy} = 0$.

Circles indicate the experimental yield value for both RD and TD in the respective condition (black: control, blue: medium strain, red: high strain, green: medium-temperature, and magenta: high temperature).

c) Lankford Coefficients

The result of the fitting process is applied and shown in Figure 4-7 for R values. In general, the analytically reproduced values show a good approximation for all directions, and it can be considered a means of all conditions. A limitation of the proposed methodology is the constant value of the anisotropy coefficients. In this sense, Plunkett and Wu (Plunkett et al., 2007; S.-H. Wu et al., 2015) proposed an evolution scheme of the anisotropy coefficients as a function of the cumulative plastic strain. Besides, the same structure could be considered for asymmetry evolution. This change in the methodology could improve the match of the analytical curves, especially for TD in the high strain rate condition and all directions in the high-temperature scenario.

The adjusted true Lankford curves for RD, DD, and TD directions in all conditions are presented in Figure 4-7, where the R value is plotted against the axial plastic strain. Here, the range of interest is bounded from 0.1 of plastic strain until the OS-Necking, avoiding R values' initial noise. Because there is no dependency of the R values to the test conditions, only the numerical control is plotted to avoid redundancy.



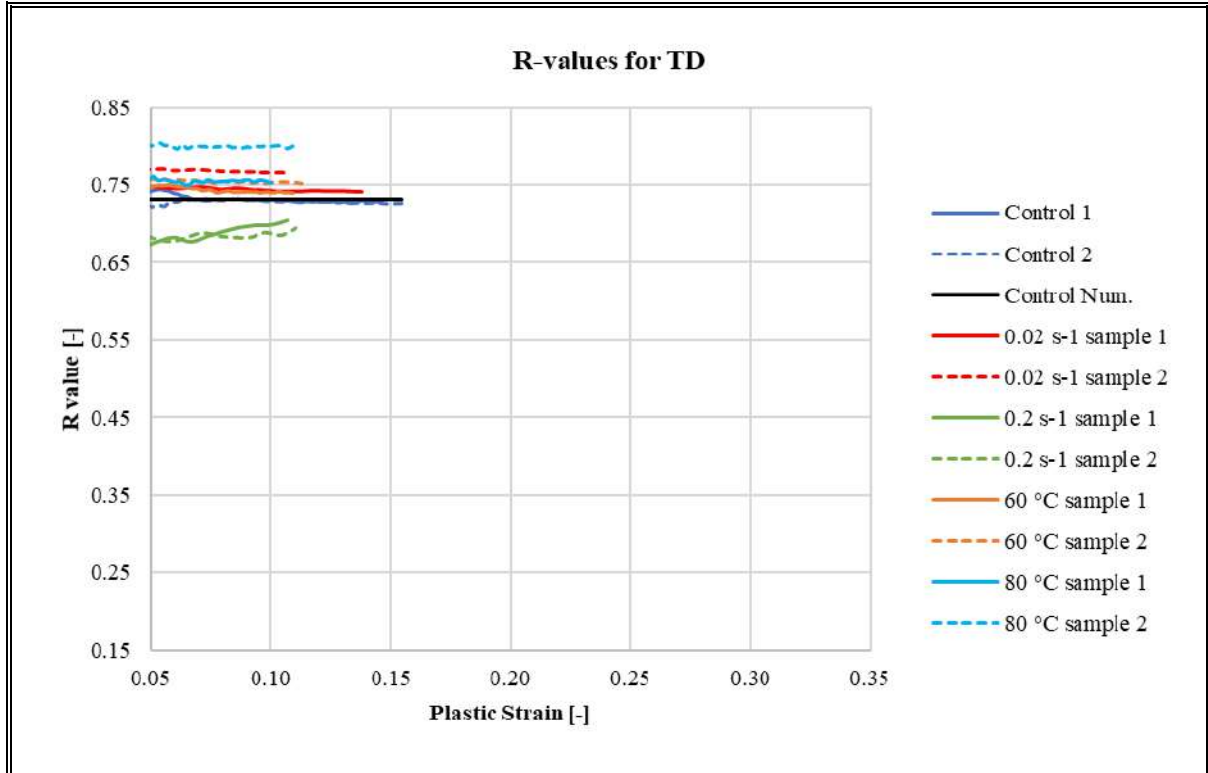


Figure 4-7: Experimental and numerical Lankford coefficient vs. plastic strain curves for all directions and conditions. From top to bottom: RD, DD, and TD, respectively.

d) Root Mean Square Error Results

The RMSE is graphically presented in Figures 4-8 and 4-9 for each direction and condition. The results are based on the functions presented in equations (4.30) and (4.31) for Stress and R values. Figure 4-8 shows the numerical RMSE for the stress-strain curves.

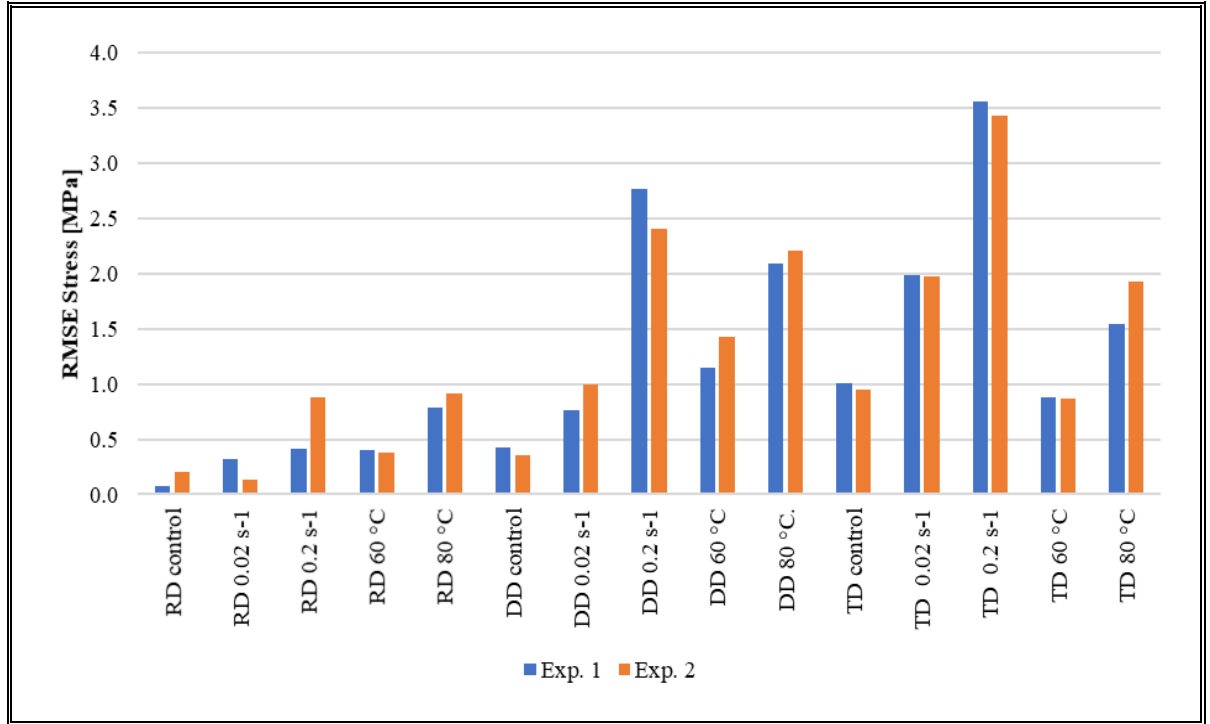


Figure 4-8: True stress RMSE for each direction, condition, and repetition based on the numerical model.

The worst approaches are the high strain rate condition followed by the high temperature for all directions and repetitions. In DD and TD, which have the highest RMSE value, the strain rate is by far the less precise modeled condition. The best approaches are obtained for all directions in the control case (0.002 s^{-1} at $^{\circ}\text{C}$).

In comparison, for the TD case, the strain rate condition almost doubles the high-temperature RMSE. So then, it would be interesting to study the evolution of anisotropy coefficients as a function of strain rate or accumulated plastic strain.

In general, for stress-strain curves, the RMSE tends to be constant for all directions and cases, with an RMSE close to 1.0 MPa, except for DD, TD, high strain rates and high-temperature conditions on which the value surpasses 2.0 MPa.

Figure 4-9 shows the numerical RMSE for the Lankford curves for each experiment and condition.

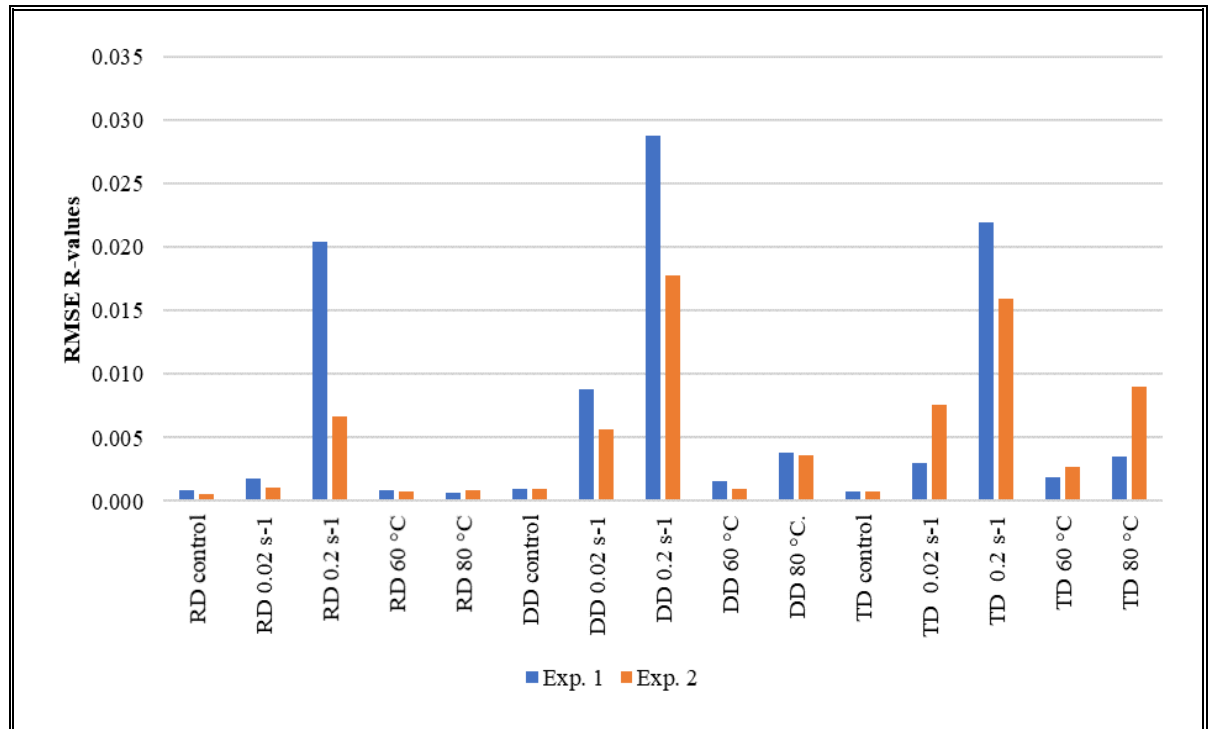


Figure 4-9: Lankford coefficient RMSE for each direction, condition, and repetition based on the numerical model.

For R values, the less precise approaches are for the high strain and high-temperature conditions for all directions, while the best results are obtained for the control condition. In contrast with the stress RMSE, the high strain rate values are more significant than the other conditions. In this sense, for all other conditions, the RMSE is around 0.05.

4.4 Conclusions

The Zn20 alloy exhibits a complex behavior for hardening and R values. Moreover, the response of the material is highly influenced by the strain rate and temperature. A

constitutive model based on CPB-06/Johnson-Cook is implemented to replicate the experimental uniaxial test results through an associated elastoviscoplastic model.

The experimental results show that R value is not significantly affected while the strain rate and temperature highly influence hardening. Therefore, the fitting process was performed for base or control conditions while the hardening law, together with anisotropy coefficients, broadly describes the material behavior for other scenarios.

The use of CPB-06/Johnson-Cook in its associated form, and the proposed fitting procedure, are fast and straightforward, demonstrating that it can deal with the complex behavior of Zn20 without compromising the accuracy of the results. This work is presented as a base framework to drive numerical simulation dedicated to industrial forming process.

Improvements need to be performed to achieve better agreements for directions different from RD, especially TD. In this sense, evolving anisotropy coefficients or exploring the alloy's asymmetry behavior are presented as a new challenge in this research.

5 CONCLUSIONS, PRESENT AND FUTURE WORKS

5.1 Conclusions

The CPB-06 in its associated form is presented and used as the base of a constitutive model to describe the complex behavior of the Zn20 alloy under different loading paths and test conditions with a unique and constant set of anisotropic coefficients L . In this sense, the material is experimentally characterized using tensile, shear, compression, and bulge test. Besides, the material behavior under different strain rates and temperatures is also explored in the tensile test. Based on the presented results, using the CPB-06 in its associated form, together with phenomenological quasi-static and dynamic hardening laws, proves to be a good and robust way to describe the elastoplastic anisotropic behavior of Zn20 alloy. It is intended that this research will be a helpful framework to face complex forming processes for zinc alloys.

In Chapter 2, related to the specific objective i , the CPB-06/Swift associate constitutive model, together with the proposed fitting procedure, are presented and prove to be a useful and robust way to describe the elastoplastic anisotropic behavior of a zinc alloy. In this context, a unique set of anisotropic coefficients could reproduce the experimental tensile stress-strain curves and Lankford coefficients. Besides, the strain paths in the bulge test using different dies were properly validated for the equibiaxial $\beta=1.00$, $\beta=0.50$ in RD, and $\beta=0.33$ in TD cases, while only approximate results have been obtained for the $\beta=0.50$ in TD and $\beta=0.33$ in RD cases. Together with the good approach of the stress-strain curves, these results

reinforce using an associated flow rule to reproduce the anisotropy behavior of Zn20 sheets.

In the context of the specific objectives *i* and *ii*, Chapter 3 validate the use of CPB-06 to capture the anisotropy and strain evolution in different loading paths compared to those studies based on Hill-48. The simulations show a good agreement in the strain path and evolution, independent of the test's condition. The calibration of the constitutive model parameters was obtained exclusively from the tensile tests, while the hardening parameters were adjusted only from RD data. The CPB-06 yield function replicates the hardening behavior and Lankford values based on a unique set of anisotropy coefficients and a very well-known hardening law.

Chapter 4 is devoted to accomplishing the specific objective *iii*; here, the experimental results show that while the strain rate and temperature highly influence hardening, R values are not significantly affected. Therefore, the fitting process was performed for control conditions while the hardening law, together with anisotropic coefficients, broadly describes the material behavior for other conditions.

Finally, the use of CPB-06/Johnson-Cook in its associated form, and the proposed fitting procedure, are fast and straightforward compared to the non-associated form of CPB-06, demonstrating that it can deal with the complex behavior of Zn20 without compromising the accuracy of the results.

5.2 Present Work

The work is at this time focused on applying the framework developed in this research in complex forming. These are deep drawings processes with semispherical and prismatic dies. All the experimental data and fitted coefficients will be used in

Finite element simulations of the forming experiences. The experimental results are already obtained and analyzed. In this line, the comparison bases are strain field, thickness reduction, and shape compliance between simulations and samples.

Furthermore, special attention is put on the evolution of earring defects during the prismatic die process. The final objective is to broaden the current research results, apply them to a real forming condition to study the influence of the anisotropy in the evolution of the thickness, shape, and earring. Figure 5-1 shows the result of the experimental campaign for the prismatic die drawing.



Figure 5-1: Prismatic die drawing samples for earring defect analysis.

The semispherical die samples after the test are shown in Figure 5-2. This assay is intended to compare the thickness reduction and compliance of the shape after forming between the experimental samples and FEM simulations.



Figure 5-2: Semispherical die drawing samples for shape and thickness reduction analysis.

5.3 Future Work

The present research is intended as a methodological base to define the formability of zinc alloys, with the construction of numerically generated Forming Limit Diagrams (FLD) and the prediction of failure areas in forming process. With this aim, future work is focused on the following areas:

- Develop an evolutionary scheme of the anisotropic coefficients L and k parameters as a function of the accumulated strain and temperature. This modification of the actual model gives a dynamic and evolving yield surface that

could broaden the flexibility of CPB-06 and improve the material behavior prediction in high strain levels.

- Include the Marciniack-Kuczynski necking criteria combined with CPB-06 to numerically define the formability of zinc alloys in the FLD with the construction of the Forming Limit Curves (FLC).
- The fitting of the phenomenological damage criteria Modified Mohr-Coulomb or MMC enriches the alloys' formability description and predicts failure areas in forming simulations.
- Explore the impact of experimental uncertainties and material variations in the numerical prediction of the implemented models.

REFERENCES

- Alistar, F., Celentano, D., Nicoletti, E., Signorelli, J., Bouchard, P.-O., Pino, D., Pradille, C., & Cruchaga, M. (2021). Elastoplastic Characterization of Zn-Cu-Ti Alloy Sheets: Experiments, Modeling and Simulation. *Journal of Materials Engineering and Performance*.
- Alistar, F., Celentano, D., Signorelli, J., Bouchard, P.-O., Pino, D., & Cruchaga, M. (2019). Characterization of the elastoplastic response of low zn-cu-ti alloy sheets using the cpb-06 criterion. *Materials*, *12*(19), 1–14.
- An, Y. G., Vegter, H., & Heijne, J. (2009). Development of simple shear test for the measurement of work hardening. *Journal of Materials Processing Technology*, *209*(9), 4248–4254.
- Banabic, D. (2000). Formability of Metallic Materials. In *Springer*.
- Banabic, D., Barlat, F., Cazacu, O., & Kuwabara, T. (2010). Advances in anisotropy and formability. *International Journal of Material Forming*, *3*(3), 165–189.
- Barlat, F., Aretz, H., Yoon, J. W., Karabin, M. E., Brem, J. C., & Dick, R. E. (2005). Linear transformation-based anisotropic yield functions. *International Journal of Plasticity*, *21*(5), 1009–1039.
- Barlat, F., Becker, R. C., Hayashida, Y., Maeda, Y., Yanagawa, M., Chung, K., Brem, J. C., Lege, D. J., Matsui, K., Murtha, S. J., & Hattori, S. (1997). Yielding description for solution strengthened aluminum alloys. *International Journal of Plasticity*, *13*(4), 385–401.
- Barlat, F., Lege, D. J., & Brem, J. C. (1991). A six-component yield function for anisotropic materials. *International Journal of Plasticity*, *7*(7), 693–712.
- Barlat, F., Maeda, Y., Chung, K., Yanagawa, M., Brem, J. C., Hayashida, Y., Lege, D. J., Matsui, K., Murtha, S. J., Hattori, S., Becker, R. C., & Makosey, S. (1997). Yield function

- development for aluminum alloy sheets. *Journal of the Mechanics and Physics of Solids*, 45(11–12), 1727–1763.
- Barros, P. D., Alves, J. L., Oliveira, M. C., & Menezes, L. F. (2016). Modeling of tension-compression asymmetry and orthotropy on metallic materials: Numerical implementation and validation. *International Journal of Mechanical Sciences*, 114, 217–232.
- Blaber, J., Adair, B., & Antoniou, A. (2015). Ncorr: Open-Source 2D Digital Image Correlation Matlab Software. *Experimental Mechanics*, 55(6), 1105–1122.
- Borodachenkova, M., Wen, W., Barlat, F., Pereira, A., & Grácio, J. (2015). Modeling of the mechanical behavior and texture evolution in Zn alloys during reverse shear loading. *Journal of Materials Processing Technology*, 224, 143–148.
- Bouchard, P.-O., Bourgeon, L., Fayolle, S., & Mocellin, K. (2011). An enhanced Lemaitre model formulation for materials processing damage computation. *International Journal of Material Forming*, 4(3), 299–315.
- Brunton, J. H., & Wilson, M. (1969). The Kinetics of Twinning in Zinc and Tin Crystals. *Proceedings of the Royal Society A: Mathematical, Physical and Engineering Sciences*, 309(1498), 345–361.
- Cao, T. S., Gachet, J. M., Montmitonnet, P., & Bouchard, P.-O. (2014). A Lode-dependent enhanced Lemaitre model for ductile fracture prediction at low stress triaxiality. *Engineering Fracture Mechanics*, 124–125, 80–96.
- Cauvin, L., Raghavan, B., Bouvier, S., Wang, X., & Meraghni, F. (2018). Multi-scale investigation of highly anisotropic zinc alloys using crystal plasticity and inverse analysis. *Materials Science and Engineering A*, 729, 106–118.
- Cazacu, O., & Barlat, F. (2004). A criterion for description of anisotropy and yield differential effects in pressure-insensitive metals. *International Journal of Plasticity*, 20(11 SPEC. ISS.), 2027–2045.

- Cazacu, O., Ionescu, I. R., & Yoon, J. W. (2010). Orthotropic strain rate potential for the description of anisotropy in tension and compression of metals. *International Journal of Plasticity*, 26(6), 887–904.
- Cazacu, O., Plunkett, B., & Barlat, F. (2006). Orthotropic yield criterion for hexagonal closed packed metals. *International Journal of Plasticity*, 22(7), 1171–1194.
- Celentano, D., Guelorget, B., Francois, M., Cruchaga, M., & Slimane, A. (2012). Numerical simulation and experimental validation of the microindentation test applied to bulk elastoplastic materials. *Modelling and Simulation in Materials Science and Engineering*, 20, 196–198.
- Chandola, N., Lebensohn, R. A., Cazacu, O., Revil-Baudard, B., Mishra, R. K., & Barlat, F. (2015). Combined effects of anisotropy and tension-compression asymmetry on the torsional response of AZ31 Mg. *International Journal of Solids and Structures*, 58, 190–200.
- Chen, K. (2020). A general and unified theory of the kinematic relationships in bulge tests. *Journal of the Mechanics and Physics of Solids*, 143, 104086.
- Chen, K., Scales, M., Kyriakides, S., & Corona, E. (2016). Effects of anisotropy on material hardening and burst in the bulge test. *International Journal of Solids and Structures*, 82, 70–84.
- Cheng, C., Wan, M., Wu, X. D., Cai, Z. Y., Zhao, R., & Meng, B. (2017). Effect of yield criteria on the formability prediction of dual-phase steel sheets. *International Journal of Mechanical Sciences*, 133, 28–41.
- Dasappa, P., Inal, K., & Mishra, R. K. (2012). The effects of anisotropic yield functions and their material parameters on prediction of forming limit diagrams. *International Journal of Solids and Structures*, 49(25), 3528–3550.
- Delannay, L., Logé, R., Signorelli, J., & Chastel, Y. (2004). Prediction of the planar anisotropy of springback after bending of a textured zinc sheet. *AIP Conference*

Proceedings, 712, 1058–1063.

Diot, M., Fundenberger, J. J., Philippe, M. J., Wegria, J., & Esling, C. (1998). Texture gradient in rolled zinc sheets. *Scripta Materialia*, 39(11), 1623–1630.

Faur, M., & Cosmeleață, G. (2006). Effects of hot and cold rolling on the microstructure of low alloy Zn-Cu and Zn-Cu-Ti zinc alloy with improved corrosion resistance. *UPB Scientific Bulletin, Series B: Chemistry and Materials Science*, 68(1), 67–74.

Florando, J. N., Rhee, M., Arsenlis, A., Leblanc, M. M., & Lassila, D. H. (2006). Calculation of the slip system activity in deformed zinc single crystals using digital 3-D image correlation data. *Philosophical Magazine Letters*, 86(12), 795–805.

Fundenberger, J. J., Philippe, M. J., Wagner, F., & Esling, C. (1997). Modelling and prediction of mechanical properties for materials with hexagonal symmetry (zinc, titanium and zirconium alloys). *Acta Materialia*, 45(10), 4041–4055.

Gilles, G. (2015). Experimental study and modeling of the quasi-static mechanical behavior of Ti6Al4V at room temperature. *Universite de Liege, March*.

Gilles, G., Cazacu, O., Hammami, W., Habraken, A. M., & Duchêne, L. (2012). Experimental and numerical study of TA-6V mechanical behavior in different monotonic loading conditions at room temperature. *Procedia IUTAM*, 3(September 2015), 100–114.

Gilles, G., Hammami, W., Libertiaux, V., Cazacu, O., Yoon, J. H., Kuwabara, T., Habraken, A. M., & Duchêne, L. (2011). Experimental characterization and elasto-plastic modeling of the quasi-static mechanical response of TA-6 v at room temperature. *International Journal of Solids and Structures*, 48(9), 1277–1289.

Hill, R. (1948). A theory of the yielding and plastic flow of anisotropic metals. *Proceedings of the Royal Society A: Mathematical, Physical and Engineering Sciences*, 260, 459–474.

Hill, R. (1979). Theoretical plasticity of textured aggregates. *Mathematical Proceedings of*

the Cambridge Philosophical Society, 85(October 2008), 179.

Hill, R. (1990). Constitutive modelling of orthotropic plasticity in sheet metals. *Journal of the Mechanics and Physics of Solids*, 38(3), 405–417.

Hockett, J. E., & Sherby, O. D. (1975). Large strain deformation of polycrystalline metals at low homologous temperatures. *Journal of the Mechanics and Physics of Solids*, 23(2), 87–98.

Hosford, W., & Allen, T. J. (1973). Twinning and directional slip as a cause for a strength differential effect. *Metallurgical Transactions*, 4(5), 1424–1425.

Jansen, Y., Logé, R., Manach, P.-Y., Carbuccia, G., & Milesi, M. (2016). On the benefits of a stress criterion for the simulation of cup drawing process. *International Journal of Material Forming*.

Jansen, Y., Logé, R., Milesi, M., Manov, S., & Massoni, E. (2011). Theoretical and Experimental Evaluation of the Formability of Anisotropic Zinc Sheets. *Key Engineering Materials*, 473(November 2016), 390–395.

Jansen, Y., Logé, R., Milesi, M., Manov, S., & Massoni, E. (2012). Using Cross Stamping to Test Zinc Sheets Formability. *Key Engineering Materials*, 504–506(November 2016), 65–70.

Jansen, Y., Logé, R., Milesi, M., & Massoni, E. (2013). An anisotropic stress based criterion to predict the formability and the fracture mechanism of textured zinc sheets. *Journal of Materials Processing Technology*, 213(6), 851–855.

Johnson, G. R., & Cook, W. H. (1983). A constitutive model and data for metals subjected to large strains, high strain rates and high temperatures. In *7th International Symposium on Ballistics* (pp. 541–547).

Kabirian, F., & Khan, A. S. (2015). Anisotropic yield criteria in T-S Stress space for materials with yield asymmetry. *International Journal of Solids and Structures*, 67–68,

116–126.

Kakogiannis, D., Verleysen, P., Belkassem, B., Coghe, F., & Rabet, L. (2018). Multiscale modelling of the response of Ti-6Al-4V sheets under explosive loading. *International Journal of Impact Engineering*, *119*(March), 1–13.

Kang, W. J., Cho, S. S., Huh, H., & Chung, D. T. (1999). Modified Johnson-Cook model for vehicle body crashworthiness simulation. *International Journal of Vehicle Design*, *21*(4-5 SPEC. ISS.), 424–435.

Kuwabara, T., Kumano, Y., Ziegelheim, J., & Kurosaki, I. (2009). Tension-compression asymmetry of phosphor bronze for electronic parts and its effect on bending behavior. *International Journal of Plasticity*, *25*(9), 1759–1776.

Lankford, W. I., Snyder, S. C., & Bauscher, J. A. (1950). New criteria for predicting the press performance of deep-drawing sheets. *Transaction ASM*, *42*, 1196–1232.

Larour, P. (2010). Strain rate sensitivity of automotive sheet steels: influence of plastic strain, strain rate, temperature, microstructure, bake hardening and pre-strain. *https://D-Nb.Info/1007085649/34*, April, 270.

Ledbetter, H. M. (1977). Elastic properties of Zinc: a Compilation and a Review. In *Journal of Physical and Chemical Reference Data* (Vol. 6, Issue 4, pp. 1181–1203).

Leonard, M., Moussa, C., Roatta, A., Seret, A., & Signorelli, J. (2020). Continuous dynamic recrystallization in a Zn–Cu–Ti sheet subjected to bilinear tensile strain. *Materials Science and Engineering A*, *789*(May), 139689.

Leonard, M., Nicoletti, E., Roatta, A., Stout, M., Bolmaro, R., & Signorelli, J. (2019). Study of Zinc-Sheet Mechanical Anisotropy and its Relationship to Crystallographic Texture. *Revista Latinoamericana de Metalurgia y Materiales*, *8*(1), 43–47.

Leonard, M., Nicoletti, E., Roatta, A., Stout, M., & Signorelli, J. (2017). Anisotropía mecánica en chapas de zinc por efecto de la evolución de la textura cristalográfica y la

microestructura. *Conamet-SAM 2017*.

Li, H., Hu, X., Yang, H., & Li, L. (2015). Anisotropic and asymmetrical yielding and its distorted evolution: Modeling and applications. *International Journal of Plasticity*, 82.

Liu, C., Huang, Y., & Stout, M. G. (1997). On the asymmetric yield surface of plastically orthotropic materials: A phenomenological study. *Acta Materialia*, 45(6), 2397–2406.

Maeda, T., Noma, N., Kuwabara, T., Barlat, F., & Korkolis, Y. P. (2017). Experimental Verification of the Tension-Compression Asymmetry of the Flow Stresses of a High Strength Steel Sheet. *Procedia Engineering*, 207, 1976–1981.

Mansouri, L. Z. (2020). Investigation of Portevin-Le Chatelier effect during Erichsen test. *International Journal of Material Forming*, 13, 687–697.

Milesi, M., Chastel, Y., Hachem, E., Bernacki, M., Logé, R., & Bouchard, P.-O. (2010). A multi-scale approach for high cycle anisotropic fatigue resistance: Application to forged components. *Materials Science and Engineering A*, 527(18–19), 4654–4663.

Milesi, M., Lecoq, J., Pradille, C., Vitu, L., Boudeau, N., & Bouchard, P.-O. (2020). Impact of strain rate sensitivity on the identification of the material parameters scattering and on the formability of zinc sheet. *International Journal of Material Forming*, 13(2), 203–218.

Milesi, M., Logé, R., & Jansen, Y. (2014). Anisotropic mechanical behavior and formability criterion for zinc sheets. *Journal of Materials Processing Technology*, 214(12), 2869–2876.

Milesi, M., Logé, R., Pino, D., Jansen, Y., & Bouchard, P.-O. (2017). Accounting for material parameters scattering in rolled zinc formability. *Journal of Materials Processing Technology*, 245, 134–148.

Milesi, M., Pino, D., Lagroum, A., Pradille, C., & Bouchard, P.-O. (2020). Self-heating of rolled ZnCuTi sheets. *Sadhana - Academy Proceedings in Engineering Sciences*, 45(1), 1–

11.

Miyauchi, K. (1984). A proposal of a planar simple shear test in sheet metals. *Scientific Papers of the Institute of Physical and Chemical Research*, 78(3)(1984), 27–40.

Muhammad, W., Mohammadi, M., Kang, J., Mishra, R. K., & Inal, K. (2015). An elasto-plastic constitutive model for evolving asymmetric/anisotropic hardening behavior of AZ31B and ZEK100 magnesium alloy sheets considering monotonic and reverse loading paths. *International Journal of Plasticity*, 70, 30–59.

Niu, J., Tang, Z., Huang, H., Pei, J., Zhang, H., Yuan, G., & Ding, W. (2016). Research on a Zn-Cu alloy as a biodegradable material for potential vascular stents application. *Materials Science and Engineering C*, 69, 407–413.

Nurcheshmeh, M., & Green, D. E. (2016). Prediction of forming limit curves for nonlinear loading paths using quadratic and non-quadratic yield criteria and variable imperfection factor. *Materials and Design*, 91, 248–255.

Oya, T., Yanagimoto, J., Ito, K., Uemura, G., & Mori, N. (2014). Material model based on non-associated flow rule with higherorder yield function for anisotropic metals. *Procedia Engineering*, 81(October), 1210–1215.

Pantazopoulos, G., Toulfatzis, A., Vazdirvanidis, A., & Rikos, A. (2017). Fundamental aspects of rolled Zn alloy sheet formability: Structure-property and failure mode relationships. *Materials Science Forum*, 879, 1443–1448.

Pantazopoulos, G., Vazdirvanidis, A., Rikos, A., & Toulfatzis, A. (2013). Failure investigation of cold-rolled ZnTiCu alloy fracture during bending under ambient temperature conditions. *Journal of Failure Analysis and Prevention*, 13(6), 757–764.

Paredes, M., & Wierzbicki, T. (2020). On mechanical response of Zircaloy-4 under a wider range of stress states: From uniaxial tension to uniaxial compression. *International Journal of Solids and Structures*, 206, 198–223.

- Peerlings, R. H. J., Borst, R., Brekelmans, W. A. M., Vree, J. H. P., & Spee, I. (1996). Some observations on localization in non-local and gradient damage models. In *European Journal of Mechanics, A/Solids* (Vol. 15, Issue 6, pp. 937–953).
- Philippe, M. J., Fundenberger, J. J., Galledou, Y., Humbert, M., Wegria, J., & Esling, C. (1991). Influence of Texture on Low Temperature Bendability of Zn Alloys. *Textures and Microstructures*, 14(C), 471–476.
- Philippe, M. J., Wagner, F., Mellab, C., Esling, C., & Wegria, J. (1994). Modelling of Texture Evolution for Materials of Hexagonal Symmetry - I . Application to Zinc Alloys. *Acta Metallurgica et Materialia*, 42(1), 239–250.
- Plunkett, B., Cazacu, O., & Barlat, F. (2008). Orthotropic yield criteria for description of the anisotropy in tension and compression of sheet metals. *International Journal of Plasticity*, 24(5), 847–866.
- Plunkett, B., Cazacu, O., Lebensohn, R. A., & Barlat, F. (2007). Elastic-viscoplastic anisotropic modeling of textured metals and validation using the Taylor cylinder impact test. *International Journal of Plasticity*, 23(6), 1001–1021.
- Plunkett, B., Lebensohn, R. A., Cazacu, O., & Barlat, F. (2006). Anisotropic yield function of hexagonal materials taking into account texture development and anisotropic hardening. *Acta Materialia*, 54(16), 4159–4169.
- Revil-Baudard, B., Chandola, N., Cazacu, O., & Barlat, F. (2014). Correlation between swift effects and tension-compression asymmetry in various polycrystalline materials. *Journal of the Mechanics and Physics of Solids*, 70(1), 104–115.
- Roatta, A., Stout, M., & Signorelli, J. (2020). Determination of the Forming-Limit Diagram from Deformations within Necking Instability: A Digital Image Correlation-Based Approach. *Journal of Materials Engineering and Performance*, 29(6), 4018–4031.
- Safaei, M., Lee, M. G., Zang, S. L., & De Waele, W. (2014). An evolutionary anisotropic model for sheet metals based on non-associated flow rule approach. *Computational*

Materials Science, 81, 15–29.

Schlosser, F., Schwindt, C., Fuster, V., Tommasi, A., & Signorelli, J. (2017). Crystallographic Texture Evolution of a Zinc Sheet Subjected to Different Strain Paths. *Metallurgical and Materials Transactions A: Physical Metallurgy and Materials Science*, 48(6), 2858–2867.

Schlosser, F., Signorelli, J., Leonard, M., Roatta, A., Milesi, M., & Bozzolo, N. (2019). Influence of the strain path changes on the formability of a zinc sheet. *Journal of Materials Processing Technology*, 271(December 2018), 101–110.

Schwindt, C. (2015). Desarrollo experimental y modelado computacional multiescala de la curva limite de formabilidad. Aplicacion a un acero Dual-Phase de alta resistencia. *Universidad de Rosario*.

Schwindt, C., Schlosser, F., Bertinetti, M. A., Stout, M., & Signorelli, J. (2015). Experimental and Visco-Plastic Self-Consistent evaluation of forming limit diagrams for anisotropic sheet metals: An efficient and robust implementation of the M-K model. *International Journal of Plasticity*, 73, 62–99.

Signorelli, J. W., Bertinetti, M. A., & Roatta, A. (2019). A review of recent investigations using the Marciniak-Kuczynski technique in conjunction with crystal plasticity models. *Journal of Materials Processing Technology*.

Singh, A., Basak, S., Lin, P., Roy, G., Jha, M., Mascarenhas, M., & Panda, S. (2018). Prediction of earing defect and deep drawing behavior of commercially pure titanium sheets using CPB06 anisotropy yield theory. *Journal of Manufacturing Processes*, 33(May), 256–267.

Stoughton, T. B., & Yoon, J. W. (2009). Anisotropic hardening and non-associated flow in proportional loading of sheet metals. *International Journal of Plasticity*, 25(9), 1777–1817.

Swift, H. W. (1952). Plastic instability under plane stress. *Journal of the Mechanics and Physics of Solids*, 1(1), 1–18.

- Thuillier, S., & Manach, P. Y. (2009). Comparison of the work-hardening of metallic sheets using tensile and shear strain paths. *International Journal of Plasticity*, 25(5), 733–751.
- Tromans, D. (2011). Elastic Anisotropy of HCP Metal Crystals and Polycrystals. *International Journal of Research and Reviews in Applied Sciences*, 6, 462–483.
- Tuninetti, V., Gilles, G., Milis, O., Pardoën, T., & Habraken, A. M. (2015). Anisotropy and tension-compression asymmetry modeling of the room temperature plastic response of Ti-6Al-4V. *International Journal of Plasticity*, 67, 53–68.
- Tuninetti, V., Gilles, G., Péron-lühns, V., & Habraken, A. M. (2012). Compression test for metal characterization using digital image correlation and inverse modeling. *Procedia IUTAM*, 4, 206–214.
- Tuninetti, V., & Habraken, A. M. (2014). Impact of anisotropy and viscosity to model the mechanical behavior of Ti-6Al-4V alloy. *Materials Science and Engineering A*, 605, 39–50.
- Vassilev, G. P., Liu, X. J., & Ishida, K. (2004). Reaction kinetics and phase diagram studies in the Ti-Zn system. *Journal of Alloys and Compounds*, 375(1–2), 162–170.
- Vitu, L., Laforge, N., Malécot, P., Boudeau, N., Milesi, M., & Manov, S. (2018). Flange bulging test of zinc alloy: comparison of analyses with analytical models and with stereo-correlation technique. *Procedia Manufacturing*, 15, 884–891.
- Voce, E. (1948). The relationship between stress and strain for homogeneous deformation. *Journal of the Institute of Metals*, 74, 537–562.
- Von Mises, R. (1913). Mechanics of solids in plastic state. *Göttinger Nachrichten Mathematical Physics*, 4, 582–592.
- Williams, B. W., & Boyle, K. (2016). Characterization of anisotropic yield surfaces for titanium sheet using hydrostatic bulging with elliptical dies. *International Journal of*

Mechanical Sciences, 114, 315–329.

Wu, S.-H., Song, N.-N., Pires, F., & Santos, A. (2015). Prediction of Forming Limit Diagrams for Materials with HCP Structure. *Acta Metallurgica Sinica (English Letters)*, 28(12), 1–10.

Wu, Z., Sandlöbes, S., Wang, Y., Gibson, J., & Korte-Kerzel, S. (2018). Creep behaviour of eutectic Zn-Al-Cu-Mg alloys. *Materials Science and Engineering A*, 724(November 2017), 80–94.

Yin, Q., Zillmann, B., Suttner, S., Gerstein, G., Biasutti, M., Tekkaya, A. E., Wagner, M. F., Merklein, M., Schaper, M., Halle, T., & Brosius, A. (2014). An experimental and numerical investigation of different shear test configurations for sheet metal characterization. *International Journal of Solids and Structures*, 51(5), 1066–1074.

Yoon, J. H., Cazacu, O., & Mishra, R. K. (2013). Constitutive modeling of AZ31 sheet alloy with application to axial crushing. *Materials Science and Engineering A*, 565, 203–212.

Zhang, F., Vincent, G., Sha, Y. H., Zuo, L., Fundenberger, J. J., & Esling, C. (2004). Experimental and simulation textures in an asymmetrically rolled zinc alloy sheet. *Scripta Materialia*, 50(7), 1011–1015.

Zillmann, B., Clausmeyer, T., Bargmann, S., Lampke, T., Wagner, M. F., & Halle, T. (2012). Validation of Simple Shear Tests for Parameter Identification Considering the Evolution of Plastic Anisotropy. *Technische Mechanik*, 622–630.